Investigating the Stability of Meridionally and Vertically Varying Ocean Currents Near the Equator



Jamie Rees
St Hilda's College
University of Oxford

A thesis submitted for the degree of
MSc by Research

Abstract

To understand the instability mechanisms resulting in the generation of tropical instability waves (TIWs) and to explore the transport properties of finite amplitude waves, we investigate the stability of equatorial zonal flow profiles that are motivated by those obtained in both medium and high resolution eddy-resolving coupled atmosphere-ocean general circulation model integrations. We solve the linearised equations of motion for mean profiles characteristic of active time periods with regards to TIW growth. The fastest growing instability has wavelength of ~ 1000 km and a period of ~ 30 days. TIW growth is dominated by baroclinic production associated with the meridional temperature gradient north of the equator between the cold upwelled equatorial water and the warm off-equatorial water of the northern equatorial countercurrent (NECC). Utilising a fully nonlinear idealised three-dimensional zonally periodic channel in the NEMO ocean model initialised with identical mean fields as the linear model, we are able to explore the properties of TIWs throughout their life-cycle from early (linear) growth to decay. In this model, TIWs develop with wavelengths and periods of 930km and 37.5 days, respectively. In agreement with the linear model, the early stage of TIW development is dominated by baroclinic production. However, as the TIWs equilibrate, they are dominated by a barotropic source and sink located on the northern and southern flanks of the equatorial undercurrent (EUC), respectively. The nonlinear model indicates that the net effect of TIWs on the mean fields is to decelerate the northern branch of the southern equatorial current (SECN), warm the surface equatorial waters associated with the equatorial cold tongue (ECT), and cool the subsurface northern waters associated with the NECC. Investigation of the terms in the eddy stress tensor elucidates the impact of TIWs on the mean flow. Eddies associated with TIWs act to flux eastward momentum into the SECN which decelerates the current, weakens its meridional and vertical shear, and therefore weakens the sources of barotropic and baroclinic instability from which TIWs derive their eddy energy. Employing a geometric decomposition of the eddy stress tensor allows

us to interpret eddy feedbacks onto the mean flow via the spatial distribution of eddy ellipses. Horizontal eddy tilts, moving from the EUC to the SECN, exhibit a "banana-shape" which is indicative of an eastward momentum flux convergence into the southern flank of the SECN. Eddy tilts are also consistent with linear stability theory - tilting into the shear of the mean flow to extract energy from the mean state. Understanding the origin of the instability, and the transports associated with the eddies, could allow one to adjust parametrisations based on GEOMETRIC for better representation of TIWs in coarse resolution eddy-permitting coupled atmosphere-ocean general circulation models.

Contents

1 Introduction **1**

2 Literature Review **5**

3 Coupled Model Integrations **13**

3.1 Model Description 13

3.2 Model Outputs - The Equatorial Pacific Ocean 13

3.2.1 Integration M - Medium Resolution 14

3.2.2 Integration H - High Resolution 15

3.3 Discussion 16

4 Linear Stability Analysis - Model Formulation **18**

4.1 Equations of Motion 18

4.2 Eddy Energy Budget 20

4.3 Numerics 21

4.3.1 Reliability of Numerics 22

5 Linear Stability Analysis - Results **29**

5.1 Results 29

5.2 Shortcomings and Limitations 36

5.3 Discussion 37

6 Idealised Nonlinear Model **38**

6.1 Model Description 38

6.2 Nonlinear Eddy Energy Budget 39

6.3 Model Output - Stages of the TIW Life-Cycle 42

6.3.1 Linear Stage 46

6.3.2 Equilibrated Stage 49

6.3.3 Decaying Stage 50

7 Eddy Transports **53**
7.1 Residual-Mean Equations 53
7.2 Eddy forcing on the mean flow 54
7.3 GEOMETRIC framework 56
7.3.1 Eddy Reynolds stress decomposition 57
7.3.2 Eddy form stress decomposition 60
7.4 Results 62
7.4.1 Eddy Reynolds Stresses 62
7.4.2 Eddy Buoyancy Fluxes 67

8 Conclusions **70**
8.1 Thesis Summary 70
8.2 Future Work 72

A Appendix **76**
A.1 Eigenvalues of the Eddy Reynolds Stress Tensor 76
A.2 Eigenvalues of the Eddy Form Stress Tensor 77

List of Figures

1.1 Latitude-longitude plot of sea surface temperature (SST) [°C] in late September obtained from a 1/12° horizontal resolution NEMO integration. Tropical instability waves (TIWs) are evident as anti-cyclonic vortices on both sides of the equatorial cold tongue in the eastern equatorial Pacific ocean. Figure is from Webb [2018, Figure 13]. 1

1.2 Contours of zonal geostrophic velocity [cm s^{-1}] derived from conductivity-temperature-depth data collected during the Hawaii-Tahiti Shuttle Experiment. Currents shown are zonally averaged across 150°W-158°W for February 1979 - June 1980 based on 15 quasi-monthly cruises. Solid (dashed) contours indicate eastward (westward) flow. The original figure is from Wyrtki and Kilonsky [1984, Figure 2] without labels, and the labelled version is from McPhaden and Ripa [1990, Figure 2]. Currents include the Southern Equatorial Current (SEC), Equatorial Undercurrent (EUC), Northern Equatorial Countercurrent (NECC), Northern Equatorial Current (NEC) and Equatorial Intermediate Current (EIC). The SEC is separated into two branches, namely the northern branch (SECN) and the southern branch (SECS). . . . 3

2.1 Dispersion relations for equatorial waves (up to $n = 2$), perturbed about a resting basic state, as a function of nondimensional frequency, ω^*, and nondimensional zonal wavenumber, k^*, where $\omega^* = \omega/\sqrt{\beta c}$ and $k^* = k\sqrt{c/\beta}$, where $c = \sqrt{gH}$ is the phase speed of a gravity wave at an equivalent depth H, and β is the meridional gradient of the Coriolis parameter. The equatorial waves, which are solutions of the linearised shallow water equations on an equatorial beta-plane, are given as follows: Inertia-Gravity waves ($\omega^{*2} = k^{*2} + (2n+1)$) [green solid lines], Rossby waves ($\omega^* = -k^*/(k^{*2} + (2n+1))$) [orange solid lines] and a Yanai wave ($k^* = \omega^* - 1/\omega^*$) [red solid line]. The Kelvin wave ($\omega^* = k^*$) [blue solid line] solution is obtained by assuming a zero meridional velocity perturbation in the linearised shallow water equations, and is labelled as the $n = -1$ mode. Westward propagating waves appear on the left with negative k^* and eastward propagating waves appear on the right with positive k^*. This figure is adapted from a replotting of Cane and Sarachik [1976, Figure 1]. 6

3.1 Depth-longitude cross sections of zonal velocity [ms^{-1}] (white contours) and temperature [°C] (filled colour and black solid contours) at the equator from integration M. (Left): Time-averaged over the TIW-inactive period (30 years of March and April). (Right): Time-averaged over the TIW-active period (30 years of July and August). The equatorial depth-longitude slice intercepts the Galápagos Islands at 91°W. Solid (dashed) white contours are used to denote eastward (westward) zonal velocities with contours every 0.1ms^{-1}. Bold contours denote zonal velocities every 0.5ms^{-1}. 14

3.2 Depth-latitude cross sections of zonal velocity [ms^{-1}] (white contours) and temperature [°C] (filled colour and black solid contours) at the equator from integration M, time-averaged over the TIW-inactive period (left) and the TIW-active period (right). Solid (dashed) white contours are used to denote eastward (westward) zonal velocities with contours every 0.1ms^{-1}. Bold contours denote zonal velocities every 0.5ms^{-1}. 15

3.3 Depth-longitude cross sections of zonal velocity [ms^{-1}] (white contours) and temperature [°C] (filled colour and black solid contours) at the equator from integration H. (Left): Time-averaged over the TIW-inactive period (10 years of March and April). (Right): Time-averaged over the TIW-active period (10 years of July and August). The equatorial depth-longitude slice intercepts the Galápagos Islands at 91°W. Solid (dashed) white contours are used to denote eastward (westward) zonal velocities with contours every 0.1ms^{-1}. Bold contours denote zonal velocities every 0.5ms^{-1}. 16

3.4 Depth-latitude cross sections of zonal velocity [ms^{-1}] (white contours) and temperature [°] (filled colour and black solid contours) at the equator from integration H, time-averaged over the TIW-inactive period (left) and the TIW-active period (right). Solid (dashed) white contours are used to denote eastward (westward) zonal velocities with contours every 0.1ms^{-1}. Bold contours denote zonal velocities every 0.5ms^{-1}. 16

4.1 (Left): Contours of constant non-dimensional growth rate, kc_i, as a function of $a = k/\pi$ and $b = \beta/\pi^2$ for the sinusoidal jet. The red dot denotes the largest growth rate. (Right): Stability picture for the sinusoidal jet as in Lin et al. [2020, Figure 4]. Only regions I and II are unstable, with region II exaggerated to aid visualisation. 24

4.2 (Left): Growth rates as a function of the zonal wavenumber k for the Stone's formulation of the Eady problem calculated with Richardson number $Ri = 1$ and selected values of the meridional wavenumber μ. (Right): As in the left panel, but originally from Stone [1970, Figure 2] with the meridional wavenumber denoted by λ. 25

4.3 (Left): Mean zonal velocity $U(y, z)$ [ms^{-1}] from case C of Proehl [1998]. Contours are every 0.1ms^{-1} with solid/dashed contours denoting eastward/westward flow. (Right): Mean potential density $\overline{\rho}(y, z)$ [kgm^{-3}] from case C of Proehl [1998]. 26

4.4 (Left): Growth rates for case C of Proehl [1998] obtained by solving the generalised eigenvalue problem over a range of zonal wavenumbers k. (Right): As in the left panel but from Proehl [1998, Figure 12]. 26

4.5 (Upper Left): Amplitude of the zonal velocity perturbation for the fastest growing instability from figure 4.4. For comparison with Proehl, we have normalised the amplitude to 1 with the stability characteristics of the most unstable mode stated in the bottom left of the panel. Contours are evenly spaced at every 0.1. The solid black line denotes locations where the meridional PV gradient is zero. The thick dashed line denotes the critical level locations where $U = c_r$. (Upper Right): Phase of the zonal velocity perturbation of the most unstable mode. (Bottom): As in the upper panels, but originally from Proehl [1998, Figure 13]. Proehl uses hatching to denote the locations where $U - c_r < 0$ hence our thick dashed lines correspond to the edges of this hatched region. 27

4.6 Spatial structure of barotropic (left) and baroclinic (right) conversions for the most unstable mode obtained from our findings (top) and Proehls original findings (bottom). All contoured figures are independently normalised to 1 with the maximum and minimum stated in the bottom left and with contour intervals every 0.1. For comparison with Proehl, we normalised the barotropic conversion such that the maximum value agreed with that of Proehl. Superposed are vectors for the normalised eddy pressure fluxes $(\overline{v'p'}, \overline{w'p'})$. 28

5.1 Depth-latitude plots of mean zonal velocity $U(y, z)[\mathrm{ms}^{-1}]$ ((a)-(b)), mean density $\rho_0 + \overline{\rho}(y, z)[\mathrm{kgm}^{-3}]$ ((c)-(d)), and meridional gradients of PV $[\mathrm{m}^{-2}\mathrm{s}^{-1}]$ ((e)-(f)) for model M-LIN (left column) and model H-LIN (right column). For (a) and (b), thin contours are every $0.1\mathrm{ms}^{-1}$ with solid/dashed contours denoting eastward/westward velocities, respectively. For (c)-(d), thin contours are every $0.5\mathrm{kgm}^{-3}$. For (e)-(f), thin contours are every $5 \times 10^{-16}\mathrm{m}^{-2}\mathrm{s}^{-1}$ with solid/dashed contours denoting positive/negative values, respectively. In all figures, we superpose thick solid contours denoting the regions where $Q_y = 0$. 30

5.2 Growth rates kc_i [s^{-1}] ((a)-(b)) and phase speeds c_r [ms^{-1}] ((c)-(d)) for unstable modes as a function of zonal wavenumber k for model M-LIN ((a) and (c)) and model H-LIN ((b) and (d)). At each wavenumber and eigenvalue guess, which we use to initialise the numerical solver for the generalised eigenvalue problem, we solve the linear stability problem for the 3 most unstable modes (largest imaginary parts) and colour each marker corresponding to the real part of our initial eigenvalue guess. These initialisations range from $c_r = -0.05$ to $c_r = -0.45$ in steps of 0.05. The wavenumber range highlighted in grey denotes the range of wavelengths between $\lambda = 500$km and $\lambda = 2000$km in between which TIWs have been observed. 31

5.3 Three-dimensional structure of the eigenvectors for the fastest growing instabilities at wavenumber $k = 6.18 \times 10^{-6}\text{m}^{-1}$ for model M-LIN (upper figure) and $k = 6.45 \times 10^{-6}\text{m}^{-1}$ for model H-LIN (lower figure). The figures for each model are structured as follows. In the upper left, we plot a latitude-longitude slice of the perturbations of density ρ' (colour), pressure p' (solid/dashed contours) and horizontal velocity (u', v') (quivers) at a depth of 5m. Red dotted lines are used to denote the locations where we take cross sections for the depth-longitude and depth-latitude plots. In the lower left, we plot a depth-longitude slice, at 2.5°N for models M-LIN and H-LIN, of the perturbations of density (colour), meridional velocity (solid/dashed contours) and zonal and vertical velocities (u',w') (quivers) at a latitude of 2.5°N. On the right, we plot a depth-latitude slice, at 15°E for models M-LIN and H-LIN, of the perturbations of density (colour), zonal velocity (solid/dashed contours) and meridional and vertical velocities (v', w') (quivers). We have normalised the eigenvectors such that $\max(|\rho'|) = 1$. 33

5.4 Latitude-longitude slice of the meridional eddy heat flux $\overline{v'\rho'}$ (colour) ((a),(b)) and zonal eddy momentum flux $\overline{u'v'}$ (colour) ((c),(d)) at a depth of 5m for models M-LIN (left column) and H-LIN (right column). Superposed are solid (dashed) contours of meridional velocity perturbations denoting positive (negative) values. 34

5.5 Spatial structure of the energy conversion mechanisms for the fastest growing instability at wavenumber $k = 6.18 \times 10^{-6}\mathrm{m}^{-1}$ for model M-LIN (left column) and wavenumber $k = 6.45 \times 10^{-6}\mathrm{m}^{-1}$ for model H-LIN (right column). ((a)-(b)): Barotropic conversion $-\overline{u'v'}U_y$. ((c)-(d)): Baroclinic conversion $-\alpha\overline{v'\rho'}$. ((e)-(f)): Eddy potential energy to eddy kinetic energy conversion $-(g/\rho_0)\overline{w'\rho'}$. On each plot, we superpose the eddy pressure work fields ($\overline{v'p'}$, $\overline{w'p'}$) as quivers. For barotropic conversion, we superpose the mean zonal velocity as contours, whereas for the other conversion mechanisms we superpose the mean density field. On each plot we have superposed the locations where $Q_y = 0$ (thick solid contour) and $U = c_r$ (thick dashed contour). . . . 35

6.1 Time-longitude plots of perturbation fields from integrations M-NONLIN ((a)-(c)) and H-NONLIN ((d)-(f)). Plots (a) and (d) show the meridional velocity perturbation [ms^{-1}] (filled colour and solid contours) at a depth of 5m and averaged meridionally between $[-0.5°\mathrm{N}, 0, 5°\mathrm{N}]$. Plots (b) and (e) show the meridional velocity perturbation [ms^{-1}] at a depth of 5m and averaged meridionally between $[3°\mathrm{N}, 4°\mathrm{N}]$. Plots (c) and (f) show the temperature perturbation [°C] at a depth of 125m and averaged meridionally between $[3°\mathrm{N}, 6°\mathrm{N}]$. From plots (d)-(f), it is evident that integration H-NONLIN aborted the run at day 313. 43

6.2 Time series of domain averaged eddy kinetic energy (EKE) and eddy potential energy (EPE) for integrations M-NONLIN (top) and H-NONLIN (bottom). Units are $\mathrm{m}^2\mathrm{s}^{-2}$. Highlighted vertical strips of blue, orange and green are used to denote periods of TIW development corresponding to the linear, equilibrated and decaying stages of the TIW life-cycle. Due to integration H-NONLIN failing to complete its integration, we are only able to consider data for the linear stage ($250 - 260$ days). For integration M-NONLIN, the linear stage is the time range of 200 to 210 days, equilibrated stage is 278 to 288 days, and the decaying stage is 305 to 315 days. 44

6.3 Time series of the domain average eddy energy conversion mechanisms at each timestep for integrations M-NONLIN (top) and H-NONLIN (bottom). Units are $\mathrm{m}^2\mathrm{s}^{-3}$. The coloured highlighted regions are as in figure 6.2 and denote the linear (blue), equilibrated (orange) and decaying (green) stages of the TIW life-cycle. 45

6.4 Three-dimensional structure of the outputs of the perturbation fields for integration M-NONLIN (top) at day 205 and integration H-NONLIN (bottom) at day 255. The figures for each integration are structured as follows. In the upper left, we plot a latitude-longitude slice of the perturbations of density ρ' [kgm^{-3}] (colour), sea surface height [m] (solid/dashed contours), and horizontal velocity (u', v') [ms^{-1}] (quivers) at a depth of 5m. Red dotted lines are used to denote the locations where we take cross sections for the depth-longitude and depth-latitude plots. In the lower left, we plot a depth-longitude slice, at 3°N for integration M-NONLIN and 2.5°N for integration H-NONLIN, of the perturbations of density (colour), meridional velocity (solid/dashed contours) and (u', w') (quivers). On the right, we plot a depth-latitude slice, at 15°E for integration M-NONLIN and 6°E for integration H-NONLIN, of the perturbations of density (colour), zonal velocity (solid/dashed contours) and (v', w') (quivers). 47

6.5 As in figure 5.5, but time averaged over the linear stage of the TIW life-cycle for integrations M-NONLIN (left column) and H-NONLIN (right column). Thick solid contours denote the locations where $Q_y = 0$. Thick dashed contours denote the locations $U = c_r$ where $c_r = -0.287$ms^{-1} for integration M-NONLIN and $c_r = -0.275$ms^{-1} for integration H-NONLIN. 48

6.6 As in figure 6.4, but for integration M-NONLIN at day 283 which is the midpoint of the equilibration stage of the TIW life-cycle. 49

6.7 Spatial structure of eddy energy conversion mechanisms time averaged over the linear (left column), equilibrated (middle column) and decaying (right column) stages of the TIW life-cycle for integration M-NONLIN. Thick solid contours denote the locations where $Q_y = 0$. Thick dashed contours denote the locations $U = c_r$ where $c_r = -0.287$ms^{-1}. The barotropic (first row), baroclinic (second row), eddy potential to eddy kinetic (third row) and Kelvin-Helmholtz (fourth row) eddy energy conversion mechanisms are plotted as filled colour contours. Units are m^{2}s^{-3}. We have superposed the mean zonal velocity [ms^{-1}] (first and fourth rows) and mean density [kgm^{-3}] (second and third rows) onto each plot. 50

6.8 As in figure 6.4, but for integration M-NONLIN only, at day 310 which is the midpoint of the decaying stage of the TIW life-cycle. 51

6.9 (Top left): Difference in the mean temperature field at days 315 and 200 (filled colour contours). Superposed is the mean temperature field at day 250. Red/blue boxes bound the regions where the heating/cooling are strongest. (Top right): Difference in the mean zonal velocity field at days 315 and 200 (filled colour contours). Superposed is the mean zonal velocity field at day 250. Thick dashed contours bound the edges of the westward flowing SECN. (Lower left): Time series of the mean temperature (red/blue line) given by the domain average of the red/blue bounding boxes which are shown in the upper left plot. (Lower right): Time series of the mean zonal velocity within the bounding dashed lines of the SECN. In both cases, dashed lines denote the times between which TIWs are predominantly active, namely days 200 and 300. The red dashed line denotes the phase speed of the unstable wave ($c_r = -0.287\text{ms}^{-1}$). 52

7.1 Eddy momentum fluxes associated with a "banana-shaped" eddy. Momentum converges at the centre of the eddy and yields an eastward momentum flux. The zonal average of the eddy velocities is zero, but their product can be non-zero if the eddy is anisotropic. The zonal average of $u'v'$ gives $N > 0$ and $N < 0$ on the southern and northern flanks of the eddy, respectively. Figure originally from Wardle and Marshall [2000]. 55

7.2 Zonally averaged eddy momentum flux $N = \overline{u'v'}$ (colour) calculated from models M-LIN (a) and H-LIN (b). Superposed are contours of the mean zonal velocity field at intervals of 0.1ms^{-1} with positive (negative) values denoted by solid (dashed) contours. In both plots, three black circular markers are used to denote the locations at which we plot $u' - v'$ covariance ellipses in figure 7.3, namely 1°N, 1.4°N and 1.8°N at a depth of 15m. 63

7.3 Horizontal eddy velocity covariance ellipses from models M-LIN ((a)-(c)) and H-LIN ((d)-(f)). Ellipses are calculated via scatter plots of (u', v') over longitude. Corresponding eddy ellipse eccentricity (γ_m) and tilt (ϕ_m [rads]) values are stated in the lower left of each plot. Eddy ellipses are plotted corresponding to the black circles in figure 7.2, namely 1°N ((a),(d)), 1.4°N ((b),(e)), and 1.8°N ((c),(f)) at a depth of 15m. 63

7.4 Mean zonal velocity at a depth of 15m for models M-LIN (a) and H-LIN (b). At each grid point, eddy ellipses are plotted along the mean zonal velocity field to demonstrate eddies tilting into the shear of the mean flow. The size of the eddy ellipses is proportional to the eddy kinetic energy and, for visual clarity, we have fixed the eddy eccentricity to 1. 64

7.5 Depth-latitude plot of the zonally averaged eddy momentum flux $N = \overline{u'v'}$ (colour) averaged in time over the linear period of the TIW life-cycle for integrations M-NONLIN (a) and H-NONLIN (b). Contours of the mean zonal velocity averaged over the same time period are superposed with contour intervals of 0.1ms^{-1}. Three black circular markers are used to denote the locations at which we plot $u' - v'$ covariance ellipses in figure 7.6, namely at 15m depth and 1°N, 2°N and 3°N, respectively. 65

7.6 Scatter plots of (u', v'), for integrations M-NONLIN ((a)-(c)) and H-NONLIN ((d)-(f)), time averaged over the linear period of the TIW life-cycle, at a depth of 15m, and over different meridional locations, from left to right, at $y = 1°\text{N}$, $y = 2°\text{N}$ and $y = 3°\text{N}$. Superposed are red variance ellipses with eccentricity γ_m, tilt ϕ_m and are scaled with the eddy kinetic energy. Values for the eccentricity and tilts (radians) of each ellipse are stated in the lower left of each plot. 65

7.7 Mean zonal velocity (blue) time averaged over the linear period of the TIW life-cycle and at 15m depth for integrations M-NONLIN (a) and H-NONLIN (b). At each grid point, eddy ellipses are plotted along the mean zonal velocity field to demonstrate eddies tilting into the shear of the mean flow. The size of the eddy ellipses is proportional to the eddy kinetic energy and, for visual clarity, we have fixed the eddy eccentricity to 1. 66

7.8 Hovmöller plots for the eddy ellipse quantities N $[m^2 s^{-2}]$ (a), M $[m^2 s^{-2}]$ (b) and ϕ_m (c) over the two year duration of integration M-NONLIN. Blue highlighted regions in time denote the linear, equilibrated and decaying stages of the TIW life-cycle, respectively. 67

7.9 Depth-latitude plot of the zonally averaged eddy form stress $S = f_0 \overline{v'b'}/N_0^2$ (colour) calculated from models M-LIN (a) and H-LIN (b). Superposed are contours of the mean zonal velocity field at intervals of 0.1ms^{-1} with positive (negative) values denoted by solid (dashed) contours. 68

7.10 Depth-latitude plot of the zonally averaged eddy buoyancy flux $S = f_0\overline{v'b'}/N_0^2$ (colour) averaged in time over the linear period of the TIW life-cycle for integrations M-NONLIN (a) and H-NONLIN (b). Contours of the mean zonal velocity averaged over the same time period are superposed with contour intervals of 0.1ms^{-1}. 68

7.11 Hovmöller plot for the eddy form stress S (colour) and mean zonal velocity U (contours) depth averaged over the upper 50m of the domain for the two year duration of integration M-NONLIN. Blue highlighted regions in time denote the linear, equilibrated and decaying stages of the TIW life-cycle, respectively. 69

Glossary

AOGCM Atmosphere-Ocean General Circulation Model.

ENSO El-Niño Southern Oscillation.

EUC Equatorial Undercurrent.

GEOMETRIC Generation and Energetics of Mesoscale Eddies and Their Rectified Impact on Climate.

NECC Northern Equatorial Countercurrent.

NEMO Nucleus for European Modelling of the Ocean.

SECN Northern Branch of the Southern Equatorial Current.

SECS Southern Branch of the Southern Equatorial Current.

SST Sea Surface Temperature.

TIV Tropical Instability Vortex.

TIW Tropical Instability Wave.

Chapter 1

Introduction

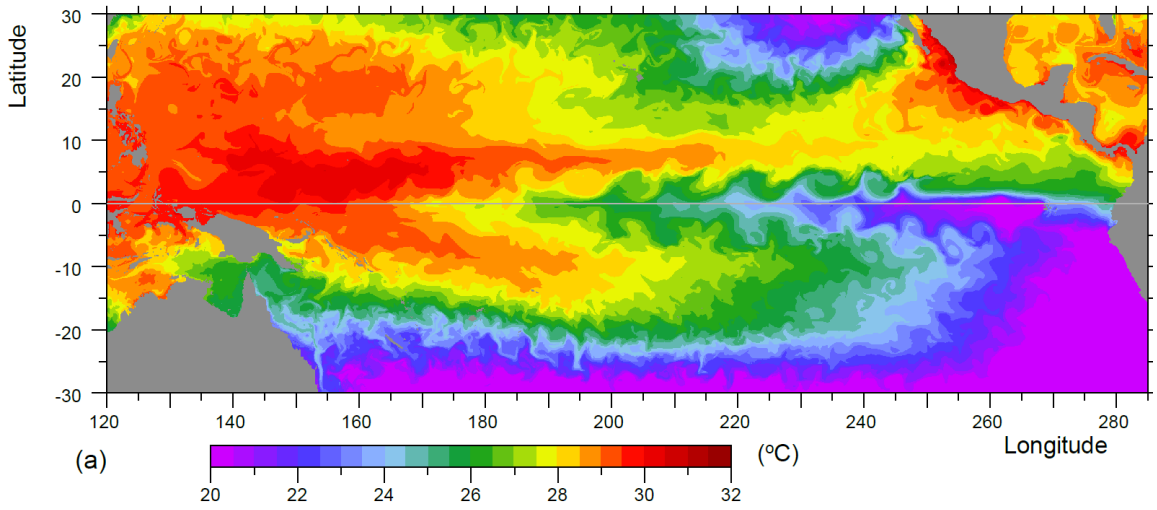


Figure 1.1: Latitude-longitude plot of sea surface temperature (SST) [°C] in late September obtained from a 1/12° horizontal resolution NEMO integration. Tropical instability waves (TIWs) are evident as anti-cyclonic vortices on both sides of the equatorial cold tongue in the eastern equatorial Pacific ocean. Figure is from Webb [2018, Figure 13].

Tropical instability waves (TIWs) are mesoscale, westward propagating, waves that grow during boreal autumn and winter. They are generally accepted to be instabilities of the mean zonal currents, generated either by the shear of the near surface currents or the strong meridional temperature gradients in the equatorial Atlantic [Duing et al., 1975] and Pacific [Legeckis, 1977] oceans. The instability is evident as a train of anticyclonic vortices in SST on both sides of the equatorial cold tongue, such as shown in Figure 1.1. Since their discovery, TIWs have been found to be important due to their role in the equatorial oceans as regulators of transports of momentum and heat and their role in exchanges between kinetic and potential energies [Baturin and Niiler, 1997]. They are also important for the spatial variability of ocean biology and chemistry [Feely et al., 1994, Strutton

et al., 2001]. We will focus on TIWs in the equatorial Pacific ocean. We will also cite papers referring to TIWs in the Atlantic ocean since their dynamics are essentially the same [Willett et al., 2006].

There are several reasons why one might study TIWs near the equator. Firstly, a persistent error in generations of coupled atmosphere-ocean general circulation models is a cold tongue bias which is characterised by an excessive westward extension of the equatorial cold tongue and results in SSTs several degrees colder than observations [Mechoso et al., 1995]. This cold bias is detrimental to the skill of GCM forecasts of global climate variability on decadal to multi-decadal timescales. TIWs are significant in the equatorial mixed layer heat budget [Jochum and Murtugudde, 2006] by acting as a negative feedback to the equatorial cold tongue [Swenson and Hansen, 1999]. TIWs offset cooling via meridional advection of equatorial cold tongue waters polewards, and warm atmospherically heated off-equatorial waters equatorwards. Coarse resolution GCMs are not able to resolve the meridional scales associated with TIWs and therefore have deficient equatorward heat transport compared to higher resolution models [Graham, 2014]. Under-representation of TIW heat transport may explain the excessively cold equatorial SSTs. A better understanding of the initial development of TIWs can enable parametrisation of TIW momentum and heat transports into coarse resolution models to reduce the cold bias.

Secondly, the origin and nature of the energy conversions resulting in TIW growth are not agreed upon in the literature. Previous energetics analyses, from observational and also numerical studies, suggest that potential sources for energy conversions are barotropic instability associated with the shear between the equatorial undercurrent (EUC) and northern branch of the southern equatorial current (SECN) [Lukas, 1987], within the SECN itself [Weisberg and Weingartner, 1988] or between the SECN and northern equatorial countercurrent (NECC) [Philander, 1978]. Baroclinic instability associated with the SST front [Yu et al., 1995] is also thought to be important.

Thirdly, TIWs could be important for the equatorial ocean circulations through their transfer of zonal momentum. The primary terms in the zonal momentum balance along the equator involve the surface wind stress, the vertical mixing of surface wind by turbulent motions and the horizontal pressure gradients associated with the slopes of the thermocline and the sea surface height. If one attempts to correct this balance in models with a cold tongue bias by making temperature increments in the biased region this can lead to overturning circulations that counteract the temperature increments [Bell et al.,

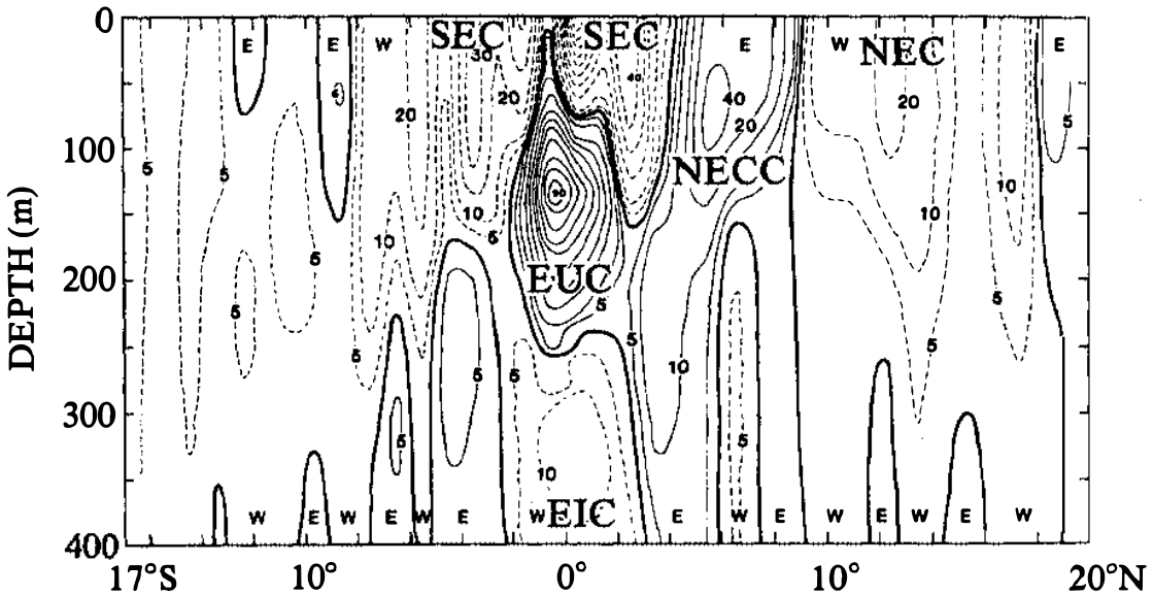


Figure 1.2: Contours of zonal geostrophic velocity [cm s^{-1}] derived from conductivity-temperature-depth data collected during the Hawaii-Tahiti Shuttle Experiment. Currents shown are zonally averaged across 150°W-158°W for February 1979 - June 1980 based on 15 quasi-monthly cruises. Solid (dashed) contours indicate eastward (westward) flow. The original figure is from Wyrtki and Kilonsky [1984, Figure 2] without labels, and the labelled version is from McPhaden and Ripa [1990, Figure 2]. Currents include the Southern Equatorial Current (SEC), Equatorial Undercurrent (EUC), Northern Equatorial Countercurrent (NECC), Northern Equatorial Current (NEC) and Equatorial Intermediate Current (EIC). The SEC is separated into two branches, namely the northern branch (SECN) and the southern branch (SECS).

2004]. One can reduce the cold tongue bias more successfully by simultaneously adjusting the model's temperature and pressure fields [Martin et al., 2002, Balmaseda et al., 2007]. This suggests that contributions to the convergence of zonal momentum on the equator by TIWs [Bryden and Brady, 1989, Baturin and Niiler, 1997] might be as important as their heat fluxes in their impact on cold biases in coupled atmosphere-ocean models.

In this thesis, we investigate the stability of equatorial zonal flow profiles motivated by those obtained in eddy-resolving coupled AOGCM integrations. We investigate the stability characteristics and eddy energetics of TIWs in both idealised linear and nonlinear models of the equatorial Pacific ocean. We then study the eddy-mean flow feedbacks associated with TIWs via investigation of the components of the eddy stress tensor and their geometric decompositions.

The thesis is structured as follows. Chapter 2 reviews the literature of TIWs. In chapter 3, we describe the details of the Met Office's coupled AOGCM, whose outputs we use as a

basis for our investigation of TIWs in the idealised linear and fully nonlinear models of the equatorial Pacific. The formulation of the linear model, and the numerical methods used to solve the linear stability problem, are discussed in chapter 4. In chapter 5, we solve the linear stability problem and investigate the stability characteristics and eddy energy diagnostics of the unstable modes. In chapter 6, we discuss the details of the fully nonlinear idealised model of the equatorial Pacific and investigate the stability characteristics and eddy energy budget of TIWs throughout their life-cycle. In chapter 7, we elucidate the role of eddy-mean flow feedbacks associated with TIWs by examining the components of the eddy stress tensor. We then review the local geometrical properties of the eddy stress tensor and derive the decomposition of key quantities in terms of bounded nondimensional parameters. We calculate and investigate these geometric quantities for both the linear and nonlinear models. The thesis concludes in chapter 8 with a summary and discussion of the findings of the thesis along with several areas of potential future work.

Chapter 2

Literature Review

Equatorial Modes

There are two distinct modes of TIWs in the equatorial Pacific, each of which is dominated by one of the set of equatorially trapped waves that occur in the absence of zonal flow [Matsuno, 1966, Musman, 1992, Lyman et al., 2007]. The equatorial region acts as a waveguide where disturbances decay rapidly away from the equator with a trapping scale given by the equatorial deformation radius which is of O(200km) for the first baroclinic mode. The dispersion relation for the infinite set of equatorially trapped waves, with meridional structure indices $n = -1, 0, 1, 2, ...$, is plotted in figure 2.1.

The first mode of TIWs is evident from alternating patterns of meridional velocity, centered on, and symmetric about, the equator with a period of ~ 17 days and resembles a surface trapped Yanai wave. A Yanai wave is the $n = 0$ mode of the equatorially trapped waves, has eastward group velocity and either eastward or westward phase velocity. For large negative wavenumbers, which correspond to westward phase propagation, a Yanai wave behaves like a Rossby wave. For large positive wavenumbers, which correspond to eastward phase propagation, a Yanai wave behaves like a gravity wave. Therefore, Yanai waves are also termed as mixed Rossby-gravity waves.

The second mode of TIWs is evident from SSTs as anticyclonic vortices on both sides of the equator, seen in Figure 1.1, and are termed as Tropical instability vortices (TIVs) [Kennan and Flament, 2000], located on both sides of the equatorial cold tongue [Legeckis, 1977, Flament et al., 1996, Yin et al., 2014]. This second mode has greater meridional extent north of the equator [Chelton et al., 2000]. Yu et al (1995) argue that this is because the SECN is stronger than the southern branch of the southern equatorial current (SECS); a meridional cross-section of the equatorial currents based on observations is shown in Figure 1.2. This mode has a period of ~ 33 days and resembles a first meridional

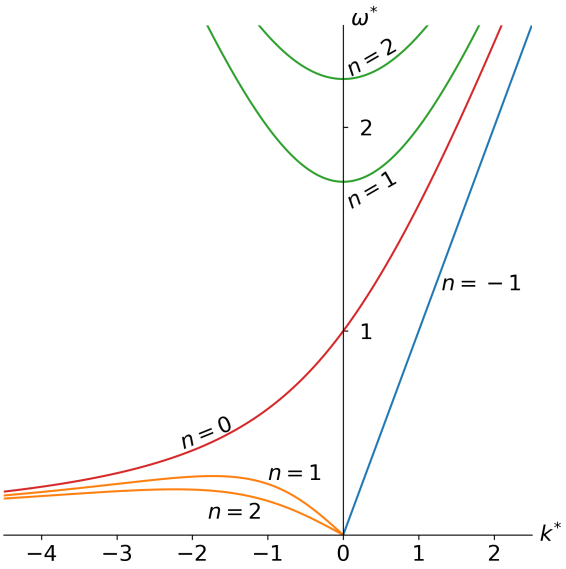


Figure 2.1: Dispersion relations for equatorial waves (up to $n = 2$), perturbed about a resting basic state, as a function of nondimensional frequency, ω^*, and nondimensional zonal wavenumber, k^*, where $\omega^* = \omega/\sqrt{\beta c}$ and $k^* = k\sqrt{c/\beta}$, where $c = \sqrt{gH}$ is the phase speed of a gravity wave at an equivalent depth H, and β is the meridional gradient of the Coriolis parameter. The equatorial waves, which are solutions of the linearised shallow water equations on an equatorial beta-plane, are given as follows: Inertia-Gravity waves ($\omega^{*2} = k^{*2} + (2n+1)$) [green solid lines], Rossby waves ($\omega^* = -k^*/(k^{*2} + (2n+1))$) [orange solid lines] and a Yanai wave ($k^* = \omega^* - 1/\omega^*$) [red solid line]. The Kelvin wave ($\omega^* = k^*$) [blue solid line] solution is obtained by assuming a zero meridional velocity perturbation in the linearised shallow water equations, and is labelled as the $n = -1$ mode. Westward propagating waves appear on the left with negative k^* and eastward propagating waves appear on the right with positive k^*. This figure is adapted from a replotting of Cane and Sarachik [1976, Figure 1].

Rossby wave. Equatorial Rossby waves are the low frequency modes, for $n = 1, 2, ...$, in the set of equatorially trapped waves (see figure 2.1). These waves have eastward or westward group velocity and only westward phase velocity. The first meridional Rossby wave is given by $n = 1$.

These TIW modes are referred to as 17 and 33 day waves [Lyman et al., 2007] and have wavelengths varying from $600 - 1800$km. A summary of observational and model findings of the periods, wavelengths and phase speeds for TIWs is given in [Qiao and Weisberg, 1995, Table 1].

Variation with season and El Nino

TIWs are seasonally and interannually variable. Initial TIW development in the Pacific begins in late northern hemisphere (NH) summer and coincides with the acceleration of the southern equatorial current (SEC) [Qiao and Weisberg, 1995] due to south-easterly trade winds. These trade winds transport warm surface waters westward, to build up the western Pacific warm pool, and upwell cold abyssal waters in the eastern Pacific which extend across the equator and form an equatorial cold tongue. During NH autumn, TIWs fully develop as westward propagating anti-cyclonic vortices along the lateral edges of the equatorial cold tongue [Philander, 1976, 1979, Baturin and Niiler, 1997, Chelton et al., 2000]. As NH winter begins, the trade winds weaken and the SECN and NECC begin to decelerate [Philander, 1976, Philander et al., 1987, Cox, 1980]. TIWs remain well defined until NH spring [Chelton et al., 2000] when the SEC and NECC are at their weakest [Philander, 1978]. Then the warm water built up in the western Pacific is able to flow eastward as an internal Kelvin wave which inhibits the development of TIWs until NH summer, when the cycle of TIW development begins again [Wyrtki, 1975, McCreary Jr and Yu, 1992, Qiao and Weisberg, 1998].

TIWs have a strong dependence on the phase of the El-Niño southern oscillation (ENSO). During the La Niña phase of ENSO, the easterly trade winds are anomalously strong. The TIWs which develop have larger amplitudes and are more energetic than TIWs in the neutral or El Niño phases of ENSO. During the El Niño phase of ENSO, the easterly trade winds are weak and can even be westerly. In this case, TIWs are either unable to develop or are very weak and confined to the far eastern Pacific [Masina, 1997].

Mechanisms for net meridional heat transport

The mechanism by which TIWs act as a net heating for the equatorial mixed layer heat budget is shown in Jochum and Murtugudde [2006, Figure 7]. As TIWs propagate westward and rotate anti-cyclonically, the cold equatorial mixed layer waters are advected polewards and are replaced by warm atmospherically heated off-equatorial water. These warm waters are then cooled by vertical entrainment through the base of the mixed layer. The meridional transport of heat may be significantly balanced by vertical entrainment [Jochum et al., 2004, Grodsky et al., 2005, Lien et al., 2008, Moum et al., 2009, 2013]. Overall, the TIWs act as a negative feedback on the equatorial cold tongue by offsetting cooling through meridional advection of heat [Swenson and Hansen, 1999]. There is no

equivalent negative feedback to the warming of the sea surface during an El Niño event. It was suggested by An [2008] that this asymmetric heating by TIWs can explain the observed ENSO asymmetry in which El Niño events have larger peak warm anomalies of SST compared to the peak cold anomalies of SST during La Niña events [An and Jin, 2004].

Equatorial Pacific SSTs are important for global climate variability due to their interaction with ENSO via Bjerknes feedback [Bjerknes, 1969]. This is a positive feedback in which equatorial zonal SST gradients drive easterly trade winds, and these easterlies strengthen the zonal SST gradient by inducing upwelling in the eastern Pacific. Accurate simulation of equatorial SSTs is important for confidence in GCM predictions of climate variability on decadal to multi-decadal timescales. However, most current numerical models exhibit a cold tongue bias which is characterised by an equatorial cold tongue which extends too far westward and is several degrees colder than observations [Mechoso et al., 1995]. Cloud and lapse rate feedbacks strongly depend on SST patterns near the equator [Andrews and Webb, 2018]. One of the consequences of a cold bias is deficient precipitation across the equatorial Pacific due to a reduction in low-level low latitude clouds [Li and Xie, 2014, Sakamoto et al., 2012].

Determining the possible origins of the cold tongue bias is an active area of research. Postulated causes include zonal wind biases, creating excessive upwelling [Vanniere et al., 2013], and atmosphere interactions with the thermocline via Bjerknes feedback [Li and Xie, 2014]. It is unclear whether the bias originates from the atmosphere [Lin, 2007], ocean [Li and Xie, 2012] or their coupling [Navarra et al., 2008].

Given that TIWs are significant for the equatorial mixed layer heat budget, we expect their role in this cold bias to be important. Roberts et al. [2004] showed that a coarse resolution model, HadCM3 whose ocean component has zonal and meridional resolutions of 1° and 1/3° respectively, weakly represent TIWs and their sharp oscillatory meridional velocities. This is demonstrated by Graham [2014] who compared the eddy meridional heat flux between 1° and 1/4° NEMO integrations. It was found that, during periods of TIW activity, the 1° model under-represented the equatorward heat flux by up to 2.5°C per month compared to the 1/4° model. Similarly, the 1/10° horizontal resolution GFDL CM2.6 model [Griffies et al., 2015] showed significantly enhanced sub-monthly advective warming of the equatorial cold tongue surface mixed layer compared to the GFDL-FLOR 1° horizontal resolution model [Ray et al., 2018]. If the meridional velocities of TIWs are not resolved, or parametrised, then TIWs cannot act as a negative feedback onto the cold

tongue. Therefore, an improved representation of TIWs would result in an improved La Niña simulation [Graham, 2014] and better simulated ENSO asymmetry [An, 2008]. A better representation of ENSO is vital since it is the largest source of global climate variability on interannual timescales. Representation of TIWs is improved by increasing model resolution, but running integrations with high resolutions for long time periods is computationally expensive. Instead, the current aim is to investigate TIWs to determine how to parametrise their dynamics into coarse resolution models [Imada and Kimoto, 2012, Tanaka and Hibiya, 2019].

One possible pathway to parametrise TIWs is to employ a GEOMETRIC framework [Marshall et al., 2012] in which eddy feedbacks onto the mean flow can be interpreted in terms of non-dimensional bounded parameters related to the geometry of eddy fluxes as principal axes of an ellipse. Implementation of the GEOMETRIC framework allows one to gain an understanding of the key quantities to be parametrised to improve coarse resolution models [Mak et al., 2017, Poulsen et al., 2019]. Previous studies have utilised this framework to elucidate the role of eddy Reynolds and eddy form stresses in the acceleration, equilibration, and deceleration of jets [Waterman and Hoskins, 2013, Stewart et al., 2015, Tamarin et al., 2016, Kontogiannis and Bakas, 2020]. The GEOMETRIC framework was successfully implemented in NEMO [Mak et al., 2018] by utilising the Gent-McWilliams parametrisation scheme for closing eddy buoyancy fluxes with a variable eddy transfer coefficient determined by the geometry of eddy fluxes.

Instability Theory

Instability theory is a tool whereby one can elucidate which mechanisms give rise to an instability of an idealised averaged initial state, and the predicted structure of the perturbations as the deviation from the mean. The potential vorticity (PV) of a fluid is an important quantity with regards to investigating stability. The Ertel PV [Ertel, 1942] of a Boussinesq fluid is given by

$$Q = \frac{\left(f\hat{\boldsymbol{k}} + \nabla \times \boldsymbol{u}\right) \cdot \nabla \rho}{\rho_0}, \tag{2.1}$$

where f is the Coriolis parameter, $\hat{\boldsymbol{k}}$ is the unit vertical vector, $\boldsymbol{u}$ is the velocity relative to the Earth's surface, ∇ is the three-dimensional gradient operator, ρ is the potential density, and ρ_0 is a constant reference density. To determine whether instability is possible for a given basic state, one can consider the necessary conditions for instability. The Charney-Stern-Pedlosky integral constraint [Charney and Stern, 1962, Pedlosky,

1964] states that, for an exponentially growing normal mode, the meridional gradient of potential vorticity must change sign within the domain or be balanced by surface temperature gradients and topographic variations. Rossby waves can be understood in terms of conservation of PV, therefore one can interpret instabilities from a counter-propagating Rossby wave perspective [Hoskins et al., 1985, Section 6]. In this framework, the positive correlation between the sign of the meridional PV gradient and the relative velocity of the zonal flow ($U - c$), where U is the mean velocity and c is the phase speed of the Rossby waves, allows two out-of-phase counter-propagating Rossby waves to induce growth in each other and this describes the situation of an exponentially growing normal mode. Both barotropic and baroclinic instability mechanisms can be interpreted in terms of horizontally or vertically counter-propagating Rossby waves, respectively. To investigate instability, the surface $Q_y = 0$ and critical surface $U = c$ where energy exchanges between the mean field and eddy field occur, are of importance.

Instability Mechanisms

There is no consensus, in the literature, on the origin and nature of the eddy energy conversions which results in TIW growth. However, there are two main instability mechanisms. Barotropic instability is associated with the meridional shears of the equatorial currents, in which eddies grow by extracting kinetic energy from the mean flow. Baroclinic instability is associated with meridional temperature gradients, in which eddies grow by extracting available potential energy from the mean flow. Postulated sources of barotropic instability for TIW growth are the meridional shears between the EUC and SECN [Lukas, 1987, Wilson and Leetmaa, 1988, Luther and Johnson, 1990, Yu et al., 1995, Qiao and Weisberg, 1998, Grodsky et al., 2005, Jochum and Murtugudde, 2006, Von Schuckmann et al., 2008, Imada et al., 2012, de Decco et al., 2018], within the SECN itself [Weisberg and Weingartner, 1988, Lyman et al., 2005] or between the SECN and NECC [Philander, 1976, 1978, Cox, 1980, Philander et al., 1986, Flament et al., 1996, Baturin and Niiler, 1997, Tanaka and Hibiya, 2019]. The SST front, due to the presence of the equatorial cold tongue, is a source of baroclinic instability [Hansen and Paul, 1984, Luther and Johnson, 1990, McCreary Jr and Yu, 1992, Yu et al., 1995, Masina et al., 1999, Grodsky et al., 2005, Von Schuckmann et al., 2008]. Drawing definitive conclusions about the responsible instability mechanisms for eddy growth is challenging due to the limitations of available observational data, primarily focused on the equator [Lukas, 1987], and since insights from numerical models, such as 1.5 layer models [Philander, 1978, Tanaka and Hibiya, 2019], are limited due to baroclinic instability not being permitted as a possible energy transfer mechanism.

Linear Stability Analyses

Linear stability analysis is a useful tool for investigating the generation of initial instabilities by superposing infinitesimal exponentially growing perturbations on the mean flow. Proehl [1996] used a linear stability analysis on equatorial zonal currents to support the idea of over-reflection theory [Lindzen, 1988] predicting instability characteristics, such as phase speed. The initial study assumed a symmetric zonal flow, but this was extended to more realistic equatorial asymmetric flows [Proehl, 1998]. It was found that asymmetry only changes the amplitude of the TIWs and not their dynamics. Lyman et al. [2005] investigated the generation mechanism for TIWs using a modal model in which the vertical structure of the variables are projected onto the set of orthogonal baroclinic modes. The unstable mode had a period of 31 days, wavelength of 1384km and was identified as a first meridional Rossby wave which grows primarily through barotropic instability, though baroclinic instability was shown to be non-negligible. Lyman et al. [2005] suggested that TIWs are generated from a resonance between westward propagating equatorial Rossby waves. Tanaka and Hibiya [2019] used a linear stability analysis in a 1.5 layer reduced gravity model to show that TIWs are generated from a resonance between intrinsically counter-propagating Rossby waves, which are Doppler shifted by the equatorial currents to be westward propagating and phase locked with each other. An unstable mode of period ~ 45 days and wavelength ~ 1700km was identified and develops from barotropic instability associated with the shear between the SECN and NECC. Each of the resonant equatorial Rossby waves are separated by an inflection point in the meridional potential vorticity gradient. Tanaka and Hibiya [2019] demonstrated that the strength of the negative potential vorticity (PV) gradient north of the equator is a significant quantity in controlling TIW dynamics. However, this result is determined by a linear stability analysis of TIWs during different seasons. This includes perturbing about a mean state which includes equilibrated large amplitude TIWs. It is not clear how useful a linear stability analysis is to a mean zonal flow when the instability of interest is already fully developed.

Ongoing Research

Ongoing research into TIWs includes the investigation into parametrisations of TIW momentum and heat transports in coarse resolution models. Boucharel and Jin [2020] derived an analytical formulation of the eddy meridional heat flux convergence associated with stochastically forced TIWs, and show that TIW feedbacks onto ENSO are highly nonlinear. This formulation could be implemented to parametrise TIWs in coarse

resolution models. However, Boucharel and Jin [2020] chose to neglect the 17 day TIW. Further investigation of the interactions between ENSO and TIWs, including these shorter period waves, would be illuminating. Other investigations into parametrisations of TIWs include Tanaka and Hibiya [2019] who suggest that the strength of the PV gradient north of the equator controls TIW dynamics and development. Extending this study to a more realistic model of the equatorial Pacific could elucidate whether the PV gradient is indeed significant for controlling TIW dynamics.

Chapter 3

Coupled Model Integrations

3.1 Model Description

We investigate outputs from two coupled atmosphere-ocean model integrations that were run by the Met Office and made available by Malcolm Roberts [Roberts et al., 2015]. Both integrations use version GO4 of the Met Office's global atmosphere model [Williams et al., 2015]. Integration M (medium resolution) has run ID u-bx950, and uses the Met Office's GO8p3 version of the NEMO ocean model with a 1/4° ORCA grid for the ocean and a N216 (60km) atmosphere. Integration H (high resolution) has run ID u-by430, and uses the Met Office's GO8p4.1 version of the NEMO ocean model with a 1/12° ORCA grid for the ocean and a N512 (25km) atmosphere. The main difference between these versions of the NEMO ocean model is the equation of state, a diagnostic equation for density in terms of temperature, salinity and pressure, namely EOS80 [UNESCO, 1983] and TEOS10 [IOC and IAPSO, 2010] for integrations M and H, respectively. Both integrations have 75 non-uniformly spaced vertical levels in the ocean ranging from a thickness of 1m at the sea surface to 200m in the abyssal ocean. Both integrations are initialised on the 1st January 1976. Integration M is initialised with temperature and salinity climatology based on EN4 [Good et al., 2013] and runs with a time step of 20 minutes for 30 years. Integration H is initialised with temperature and salinity climatology obtained from WOA13 [Locarnini et al., 2013] and runs with a time step of 10 minutes for 10 years. Both integrations output data as monthly averages. Further details on the global coupled model configuration and the NEMO ocean model are available in Williams et al. [2015] and Madec [2016].

3.2 Model Outputs - The Equatorial Pacific Ocean

For integrations M and H, we provide an overview of the zonal velocity and temperature profiles typical of the equatorial Pacific ocean during periods prior to TIW activity and also when TIW activity has ceased. To obtain zonal velocity and temperature profiles

typical of periods prior to TIW activity, we temporally average over July and August for the duration of the available data and term this as the TIW-active period. Similarly, we temporally average over March and April to obtain profiles typical of periods after TIW activity has ceased, which we term as the TIW-inactive period.

3.2.1 Integration M - Medium Resolution

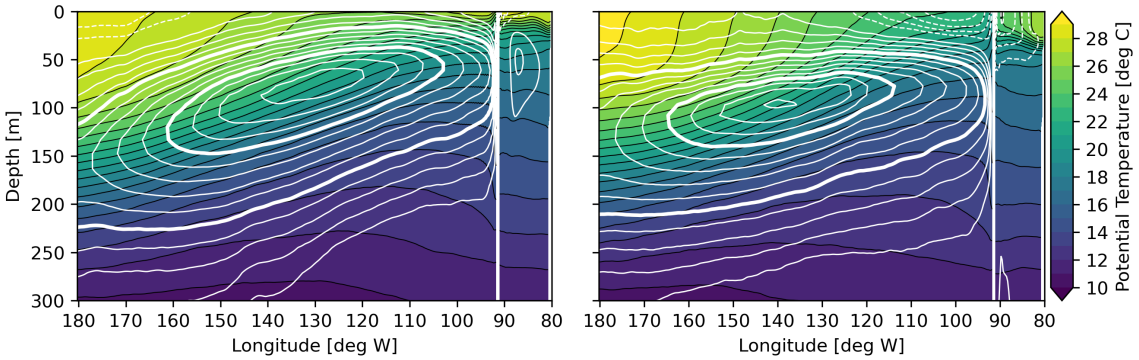


Figure 3.1: Depth-longitude cross sections of zonal velocity [ms^{-1}] (white contours) and temperature [°C] (filled colour and black solid contours) at the equator from integration M. (Left): Time-averaged over the TIW-inactive period (30 years of March and April). (Right): Time-averaged over the TIW-active period (30 years of July and August). The equatorial depth-longitude slice intercepts the Galápagos Islands at 91°W. Solid (dashed) white contours are used to denote eastward (westward) zonal velocities with contours every 0.1ms^{-1}. Bold contours denote zonal velocities every 0.5ms^{-1}.

Figure 3.1 shows that the EUC is the dominant zonal current at the equator for both the TIW-inactive and TIW-active periods and has an maximum amplitude exceeding 1ms^{-1}. For the TIW-inactive period, the EUC is shallowest near the Galápagos Islands extending from the surface down to 200m depth. The EUC deepens with the isotherms as one moves westwards and, in the central equatorial Pacific, reaches a depth of over 300m. For the TIW-active period, the EUC has weaker zonal variation with a maximum depth of 250m at the Galápagos Islands and 300m in the central equatorial Pacific. The EUC deepens across the equatorial Pacific but intersects isotherms unlike the TIW-inactive case. Above 100m, the isotherms have significantly stronger tilts and, towards the east, the westward flowing SEC appears. These features are associated with the equatorial cold tongue that occurs due to the south-easterly trade winds across the equator upwelling cold waters transported by the EUC.

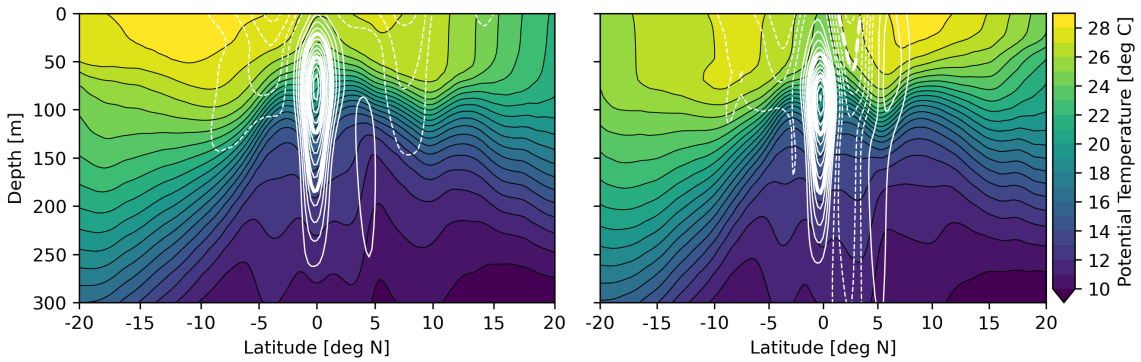


Figure 3.2: Depth-latitude cross sections of zonal velocity [ms^{-1}] (white contours) and temperature [°C] (filled colour and black solid contours) at the equator from integration M, time-averaged over the TIW-inactive period (left) and the TIW-active period (right). Solid (dashed) white contours are used to denote eastward (westward) zonal velocities with contours every $0.1ms^{-1}$. Bold contours denote zonal velocities every $0.5ms^{-1}$.

Figure 3.2 shows that the presence of a strong EUC persists during both TIW-inactive and TIW-active periods. In both cases, the EUC is narrow with a latitudinal extent of approximately 4° about the equator. The SECS is also a persistent feature of the equatorial current system. The SECS is a westward flowing current on the southern flank of the EUC with an amplitude of $0.3ms^{-1}$, depth of 100m, and lies between 1°S-10°S. North of the equator, the TIW-inactive and TIW-active profiles differ significantly. For the TIW-inactive period, there is a westward flowing current that lies away from the EUC at approximately 7°N. This is the SECN which has moved polewards due to the absence of the NECC. The NECC is present in the TIW-active period and lies at 6°N. The NECC acts to transport warm water from the western Pacific towards the eastern Pacific which is evident from the positive isotherm tilt at 6°N. The NECC also traps the westward flowing SECN between both the eastward flowing EUC and NECC.

3.2.2 Integration H - High Resolution

The zonal velocity and temperature profiles for integration H during TIW-inactive and TIW-active periods are plotted below. Since their features are similar to those of integration M, we do not repeat the same discussion as for integration M.

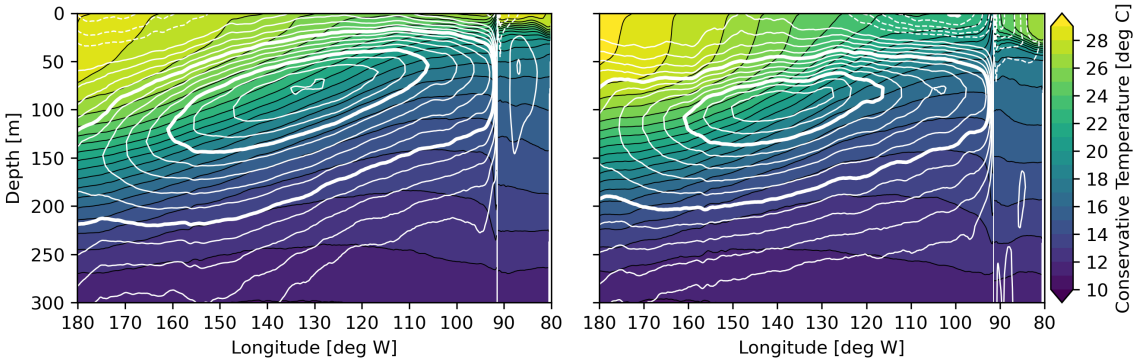


Figure 3.3: Depth-longitude cross sections of zonal velocity [ms^{-1}] (white contours) and temperature [°C] (filled colour and black solid contours) at the equator from integration H. (Left): Time-averaged over the TIW-inactive period (10 years of March and April). (Right): Time-averaged over the TIW-active period (10 years of July and August). The equatorial depth-longitude slice intercepts the Galápagos Islands at 91°W. Solid (dashed) white contours are used to denote eastward (westward) zonal velocities with contours every $0.1ms^{-1}$. Bold contours denote zonal velocities every $0.5ms^{-1}$.

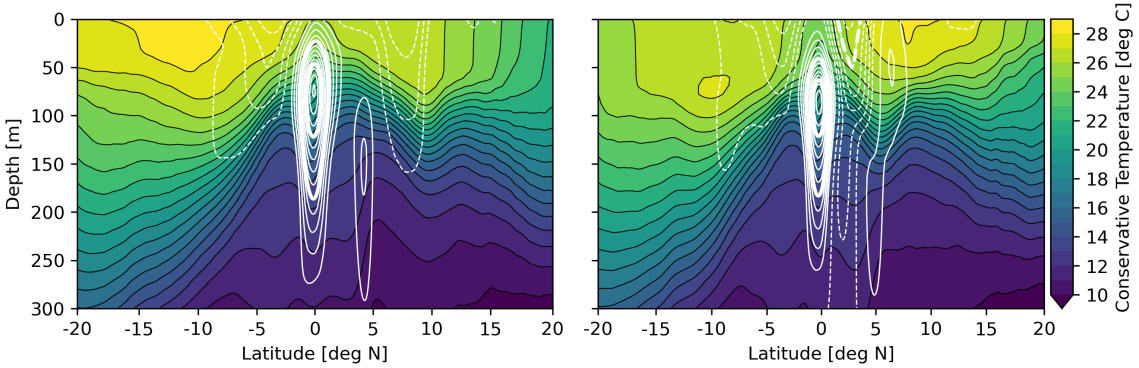


Figure 3.4: Depth-latitude cross sections of zonal velocity [ms^{-1}] (white contours) and temperature [°] (filled colour and black solid contours) at the equator from integration H, time-averaged over the TIW-inactive period (left) and the TIW-active period (right). Solid (dashed) white contours are used to denote eastward (westward) zonal velocities with contours every $0.1ms^{-1}$. Bold contours denote zonal velocities every $0.5ms^{-1}$.

3.3 Discussion

In figures 3.1-3.4, we have presented profiles of the zonal velocity and temperature which are typical of periods either prior to TIW activity or after TIW activity has ceased. By comparison to the TIW-inactive period profiles, one can hypothesise about which features of the TIW-active period are important for TIW growth. Figures 3.2 and 3.4 indicate that the strong meridional shears at each flank of the SECN, which are not evident for the TIW-inactive period, could be an important source of barotropic conversion for TIW

growth. Similarly, the positive isotherm tilt north of the equator associated with meridional temperature gradient between the cold upwelled equatorial water and the warm off-equatorial NECC water could be a significant source of baroclinic conversion for TIW growth.

As a first step towards investigating the stability of the zonal velocity and temperature fields obtained from integrations M and H, we perform a linear stability analysis. This is the simplest framework to allow us to determine the stability characteristics and properties of the most unstable waves that grow from infinitesimal perturbations of the zonal velocity and temperature fields.

Chapter 4

Linear Stability Analysis - Model Formulation

4.1 Equations of Motion

We consider the motions of a continuous, three-dimensional, inviscid, incompressible, Boussinesq fluid in a zonally unbounded channel, centered on the equator, in the absence of external forcing. For fluid motions confined near the equator, it is appropriate to take an equatorial beta plane approximation in which we treat the equatorial region as a flat surface, except for the latitudinal variation of the Coriolis parameter $f = 2\Omega \sin\theta$, where $\Omega = 7.29 \times 10^{-5}$rad s^{-1} is the rotation rate of the Earth. Taylor expanding about $\theta = 0$, and retaining only leading order terms, yields $f \approx (2\Omega/a)y = \beta y$ where $a = 6371$km is the radius of the Earth and $\beta = 2.29 \times 10^{-11}\text{m}^{-1}\text{s}^{-1}$ is the meridional gradient of the Coriolis parameter. The diameter of our channel is much less than the radius of the Earth, therefore we are able to employ a local Cartesian coordinate system centered on the equator where x, y and z are eastward, northward and upward directions, respectively, with corresponding zonal, meridional and vertical velocities u, v and w. The channel is bounded meridionally and vertically by rigid walls at $y = \pm 15^\circ$ and $z = -1000, 0$, respectively. The meridional walls are placed far enough away so as not to disturb the instabilities.

The governing equations for the continuous, three-dimensional, inviscid, hydrostatic, unforced motions of an incompressible, rotating, stratified fluid subject to Boussinesq and

equatorial beta plane approximations are

$$\frac{\partial u}{\partial t} + u\frac{\partial u}{\partial x} + v\frac{\partial u}{\partial y} + w\frac{\partial u}{\partial z} - \beta y v = -\frac{1}{\rho_0}\frac{\partial p}{\partial x}, \tag{4.1}$$

$$\frac{\partial v}{\partial t} + u\frac{\partial v}{\partial x} + v\frac{\partial v}{\partial y} + w\frac{\partial v}{\partial z} + \beta y u = -\frac{1}{\rho_0}\frac{\partial p}{\partial y}, \tag{4.2}$$

$$\frac{\partial p}{\partial z} = -\rho g, \tag{4.3}$$

$$\frac{\partial \rho}{\partial t} + u\frac{\partial \rho}{\partial x} + v\frac{\partial \rho}{\partial y} + w\frac{\partial \rho}{\partial z} = 0, \tag{4.4}$$

$$\frac{\partial u}{\partial x} + \frac{\partial v}{\partial y} + \frac{\partial w}{\partial z} = 0. \tag{4.5}$$

The boundary conditions of no-normal flow are imposed as

$$v = 0, \qquad y = \pm 15^\circ, \tag{4.6}$$

$$w = 0, \qquad z = -1000, 0. \tag{4.7}$$

We linearise the system of equations (4.1)-(4.5) by expanding about a zonally and temporally invariant background state as follows:

$$u(x, y, z, t) = U(y, z) + u'(x, y, z, t), \tag{4.8}$$

$$v(x, y, z, t) = v'(x, y, z, t), \tag{4.9}$$

$$w(x, y, z, t) = w'(x, y, z, t), \tag{4.10}$$

$$p(x, y, z, t) = \overline{p}(y, z) + p'(x, y, z, t), \tag{4.11}$$

$$\rho(x, y, z, t) = \rho_0 + \overline{\rho}(y, z) + \rho'(x, y, z, t), \tag{4.12}$$

where primes are used to denote perturbations from the mean. We have also separated the mean density into components as the constant reference background density ρ_0 and the mean background density structure $\overline{\rho}(y, z)$. The mean fields are in geostrophic and hydrostatic balance since substitution of (4.8)-(4.12) into (4.1)-(4.5) yields at leading order

$$\beta y U = -\frac{1}{\rho_0}\frac{\partial \overline{p}}{\partial y}, \tag{4.13}$$

$$\frac{\partial \overline{p}}{\partial z} = -(\rho_0 + \overline{\rho})g. \tag{4.14}$$

Taking the meridional derivative of (4.14) and substituting into (4.13), one can show that the mean zonal velocity is in thermal wind balance with the mean density via

$$\beta y \frac{\partial U}{\partial z} = \frac{g}{\rho_0}\frac{\partial \overline{\rho}}{\partial y}. \tag{4.15}$$

At next-to-leading order, the perturbation equations of motion are given by

$$\left(\frac{\partial}{\partial t}+U\frac{\partial}{\partial x}\right)u'+v'\frac{\partial U}{\partial y}+w'\frac{\partial U}{\partial z}-\beta y v'=-\frac{1}{\rho_0}\frac{\partial p'}{\partial x}, \tag{4.16}$$

$$\left(\frac{\partial}{\partial t}+U\frac{\partial}{\partial x}\right)v'+\beta y u'=-\frac{1}{\rho_0}\frac{\partial p'}{\partial y}, \tag{4.17}$$

$$\frac{\partial p'}{\partial z}=-\rho' g, \tag{4.18}$$

$$\left(\frac{\partial}{\partial t}+U\frac{\partial}{\partial x}\right)\rho'+v'\frac{\partial \overline{\rho}}{\partial y}+w'\frac{\partial \overline{\rho}}{\partial z}=0, \tag{4.19}$$

$$\frac{\partial u'}{\partial x}+\frac{\partial v'}{\partial y}+\frac{\partial w'}{\partial z}=0. \tag{4.20}$$

Seeking zonally propagating solutions of the form $\exp(ik(x-ct))$ and eliminating ρ' and w' in favour of u', v' and p' yields the system of equations

$$kUu'+i\left(\beta y-\frac{\partial U}{\partial y}\right)v'-iw'\frac{\partial U}{\partial z}+\frac{k}{\rho_0}p'=kcu', \tag{4.21}$$

$$kUv'-i\beta y u'-\frac{i}{\rho_0}\frac{\partial p'}{\partial y}=kcv', \tag{4.22}$$

$$ku'-i\frac{\partial v'}{\partial y}-i\frac{\partial w'}{\partial z}=0, \tag{4.23}$$

with w' given, using (4.18) and (4.19), by

$$w'=\frac{ik(U-c)}{g\partial\overline{\rho}/\partial z}\frac{\partial p'}{\partial z}-\frac{\partial\overline{\rho}/\partial y}{\partial\overline{\rho}/\partial z}v'. \tag{4.24}$$

The zonal and temporal structure of the perturbations can be written as $\exp(ik(x-c_r t))\exp(kc_i t)$ where we have separated the phase speed into real and imaginary parts denoted by subscripts. An unstable solution has $c_i>0$ and grows exponentially with growth rate kc_i.

4.2 Eddy Energy Budget

The eddy kinetic energy (EKE) budget is obtained from

$$u'\times(4.16)+v'\times(4.17). \tag{4.25}$$

Using (4.20) in (4.25) and then zonal averaging, which we denote by an overbar, we obtain

$$\frac{\partial}{\partial t}\left(\frac{1}{2}\left(\overline{u'^2}+\overline{v'^2}\right)\right)=-\overline{u'v'}\frac{\partial U}{\partial y}-\overline{u'w'}\frac{\partial U}{\partial z}-\frac{1}{\rho_0}\left[\frac{\partial}{\partial y}(\overline{v'p'})+\frac{\partial}{\partial z}(\overline{w'p'})\right]-\frac{g}{\rho_0}\overline{w'\rho'}. \tag{4.26}$$

The term on the left hand side of (4.26) denotes the rate of change of EKE with respect to time. The first and second terms on the right hand side of (4.26) correspond to barotropic and Kelvin-Helmholtz energy conversions, respectively. Positive values of these conversion

terms implies conversion of kinetic energy from the mean kinetic energy field to the eddy kinetic energy field, and vice versa for negative values. The third and fourth terms are the meridional and vertical eddy pressure flux divergences which act to redistribute EKE and are zero in the domain average. The fifth term denotes the energy conversion between EKE and eddy potential energy with positive (negative) values acting to increase (decrease) eddy kinetic energy. The eddy potential energy (EPE) budget is obtained from

$$-\left(\frac{g}{\rho_0 \partial\overline{\rho}/\partial z}\right)\rho' \times (4.19), \tag{4.27}$$

and, upon zonal averaging, yields

$$\frac{\partial}{\partial t}\left(\frac{\overline{b'^2}}{2N_0^2}\right) = -\alpha\overline{v'\rho'} + \frac{g}{\rho_0}\overline{w'\rho'}, \tag{4.28}$$

where

$$N_0^2 = -\frac{g}{\rho_0}\frac{\partial\overline{\rho}}{\partial z}, \tag{4.29}$$

is the Brunt-Väisälä frequency and we denote

$$\alpha = -\frac{g}{\rho_0}\frac{\partial\overline{\rho}/\partial y}{\partial\overline{\rho}/\partial z}, \qquad b' = \frac{g}{\rho_0}\rho'. \tag{4.30}$$

The term on the left hand side of (4.28) denotes the rate of change of EPE with respect to time. The first term on the right hand side of (4.28) corresponds to baroclinic conversion. Positive values imply transfer of energy from the mean potential energy field to the eddy potential energy field, and vice versa for negative values. The second term denotes the energy conversion between EKE and EPE.

Summing (4.26) and (4.28), the zonally averaged total eddy energy (TEE) budget is given by

$$\frac{\partial}{\partial t}\left(\frac{1}{2}\left(\overline{u'^2}+\overline{v'^2}\right)+\frac{\overline{b'^2}}{2N_0^2}\right) = -\overline{u'v'}U_y - \overline{u'w'}U_z - \frac{1}{\rho_0}\left[\left(\overline{v'p'}\right)_y + \left(\overline{w'p'}\right)_z\right] - \alpha\overline{v'\rho'}. \tag{4.31}$$

4.3 Numerics

The system of equations (4.21)-(4.23), together with (4.24), form a set of linear differential equations in y and z which we can solve numerically for a given wavenumber k. In both the meridional and vertical directions, the equations are cast into finite difference form on a uniform staggered grid spanning from 15°S to 15°N and from $z = -1000$m to $z = 0$m with meridional and vertical grid spacings of Δy and Δz, respectively. All three variables

u', v' and p' are defined at half points in z which are shifted $\Delta z/2$ upward from the bottom of the domain. The v' variable is defined at full points in y, which allows for easy application of the meridional boundary conditions, and both u' and p' variables are defined at the interleaved half points in y. We do not solve for w' in the system of equations (4.21)-(4.23). We implicitly satisfy the vertical no-normal flow boundary conditions (4.7) by setting w' to be zero at the vertical edges of the domain. After solving the equations of motion, one can use (4.24) to obtain w' and then either (4.18) or (4.19) to obtain ρ'. Both w' and ρ' are evaluated at full points in y and z. This staggering of variables corresponds to a C-grid [Arakawa, 1966] in the (y, z)-plane.

Upon discretisation, the system of equations (4.21)-(4.23) is written as the generalised eigenvalue problem

$$\boldsymbol{A}\underline{q} = c\boldsymbol{B}\underline{q}, \tag{4.32}$$

where $\boldsymbol{A}$ and $\boldsymbol{B}$ are complex non-hermitian square coefficient matrices of order $(3ny - 2)(nz - 1)$, where ny and nz denote the number of grid points in the meridional and vertical directions respectively, and c are the eigenvalues with corresponding eigenvectors $\underline{q}$. Although the sizes of the matrices $\boldsymbol{A}$ and $\boldsymbol{B}$ are large, we can exploit their sparseness and solve (4.32) using `scipy.sparse.linalg.eigs`. This is a Python wrapper for ARPACK [Lehoucq et al., 1998] that uses an implicitly restarted Arnoldi method to calculate the eigenvalues and corresponding eigenvectors. Where not otherwise explicitly stated, eigenvectors are normalised such that the maximum absolute value of the density perturbation is unity. The eigenvalues that we are searching for are those with the largest imaginary parts. Therefore, we employ a shift-invert method that searches for eigenvalues near a user-specified region and we sweep through the real part of the initial eigenvalue guess. To reduce computational cost, we specify the sparse solver to obtain only the three eigenvalues with the largest imaginary parts near each initial guess. We found that increasing the number of obtained eigenvalues beyond three was significantly more computationally expensive. Due to extracting only three eigenvalues per initial guess, it is possible that we could miss unstable modes if our sweep over c_r is not sufficiently dense.

4.3.1 Reliability of Numerics

In order to ensure that our numerical solver is reliable, we have solved several well-documented problems in the existing literature. We started by solving one-dimensional problems that varied either meridionally or vertically only. We achieved this by solving both the Rayleigh-Kuo [Kuo, 1949, 1973] and Eady/Stone problems [Eady,

1949, Stone, 1966, 1970]. Then we verified our numerical solver against results from a linear stability analysis of idealised two-dimensional equatorial zonal flows [Proehl, 1996, 1998].

The Rayleigh-Kuo Problem

Consider the limiting case of the equations of motion (4.1)-(4.5) for a fluid in two-dimensional (x, y)-space that is centered on the equator and bounded meridionally by rigid walls at $y = \pm L$. We perturb about a steady barotropic basic flow $U = U(y)$ and non-dimensionalise by setting

$$[x, y] = L[x^*, y^*], \;\; t = \frac{L}{V}t^*, \;\; [u, v] = V[u^*, v^*], \;\; k = \frac{1}{L}k^*, \;\; \beta = \frac{V}{L^2}\beta^*, \;\; p = \rho_0 V^2 p^*, \;\; (4.33)$$

where starred quantities are non-dimensional and V is the maximum velocity of the basic flow $U(y)$. Dropping starred notation for non-dimensional quantities, the non-dimensional linearised equations of motion are

$$\left(\frac{\partial}{\partial t} + U\frac{\partial}{\partial x}\right)u' + \left(\beta y - \frac{dU}{dy}\right)v' = -\frac{\partial p'}{\partial x}, \tag{4.34}$$

$$\left(\frac{\partial}{\partial t} + U\frac{\partial}{\partial x}\right)v' - \beta y u' = -\frac{\partial p'}{\partial y}, \tag{4.35}$$

$$\frac{\partial u'}{\partial x} + \frac{\partial v'}{\partial y} = 0, \tag{4.36}$$

subject to no normal flow on the meridional boundaries

$$v'(\pm 1) = 0. \tag{4.37}$$

Let

$$U(y) = \frac{1}{2}(1 + \cos(\pi y)), \tag{4.38}$$

be the non-dimensional basic flow. We seek zonally propagating solutions of the form $\exp(ik(x - ct))$, discretise the equations of motion, and solve the generalised eigenvalue problem with a parameter sweep over the domain

$$(\beta, k) \in (-\pi^2/2, \pi^2/2) \times (0, \sqrt{3}\pi/2), \tag{4.39}$$

since this is the region for which $\beta - U_{yy}$ changes sign and instability is possible. We obtain the contour plot for the growth rates shown in figure 4.1 which shows agreement between our figure and that of Lin et al. [2020]. If one forms a barotropic vorticity equation as the cross product between (4.35) and (4.34), and uses a perturbation stream function, then one recovers the Rayleigh-Kuo ODE studied by Kuo [1949, Equation 2].

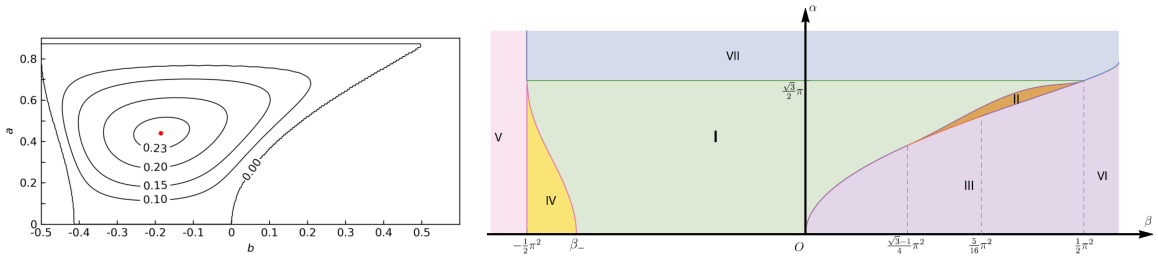


Figure 4.1: (Left): Contours of constant non-dimensional growth rate, kc_i, as a function of $a = k/\pi$ and $b = \beta/\pi^2$ for the sinusoidal jet. The red dot denotes the largest growth rate. (Right): Stability picture for the sinusoidal jet as in Lin et al. [2020, Figure 4]. Only regions I and II are unstable, with region II exaggerated to aid visualisation.

The Eady and Stone Problems

Consider the equations of motion (4.1)-(4.5) for a fluid in a zonally unbounded channel with bounding rigid walls located meridionally and vertically at $y = 0, L$ and $z = 0, H$, respectively. We employ an f-plane approximation where we set the Coriolis parameter to be the constant $f = f_0$ thereby replacing the βy terms in (4.1)-(4.5) by f_0. We perturb about a steady baroclinic basic flow $U = U(z)$ which is in thermal wind balance with the basic density field. Non-dimensionalise by setting

$$[x, y] = L[x^*, y^*], \quad z = Hz^*, \quad t = \frac{L}{V}t^*, \quad [u, v] = V[u^*, v^*], \quad w = \frac{H}{L}Vw^*,$$
$$p = \rho_0 V f_0 L p^*, \quad \rho = \rho_0 V \frac{f_0 L}{gH}\rho^*, \tag{4.40}$$

where starred quantities are non-dimensional and V is the maximum velocity of the basic flow $U(z)$. Dropping starred notation for non-dimensional quantities, the non-dimensional linearised equations of motion are

$$\epsilon\left(\frac{\partial}{\partial t} + U\frac{\partial}{\partial x}\right)u' - v' + w'\frac{\partial U}{\partial z} = -\frac{\partial p'}{\partial x}, \tag{4.41}$$
$$\epsilon\left(\frac{\partial}{\partial t} + U\frac{\partial}{\partial x}\right)v' + u' = -\frac{\partial p'}{\partial y}, \tag{4.42}$$
$$\frac{\partial u'}{\partial x} + \frac{\partial v'}{\partial y} + \frac{\partial w'}{\partial z} = 0, \tag{4.43}$$

where $\epsilon = U/f_0 L$ is the Rossby number. The linearised equations of motion are subject to periodic boundary conditions at the meridional edges of the domain and no normal flow boundary conditions at the vertical edges of the domain

$$v'(0) = v'(1), \qquad w'(0) = w'(1) = 0. \tag{4.44}$$

The vertical advective term in the zonal momentum equation, which is highlighted in red, is neglected by Eady under the assumptions of quasigeostrophic theory. The extension of

Eady's solutions to include non-geostrophic perturbations was studied by Stone. Let

$$U = z, \tag{4.45}$$

be the non-dimensional basic flow. Perturbations with sinusoidal meridional structure satisfy the meridional boundary conditions, therefore we seek solutions of the form $\exp(ik(x - ct) + i\mu y)$ which are zonally propagating with zonal wavenumber k and sinusoidal with meridional wavenumber μ. Discretising the equations of motion, we solve the generalised eigenvalue problem and calculate growth rates over a range of zonal and meridional wavenumbers k and μ. The plot for the growth rates is shown in figure 4.2.

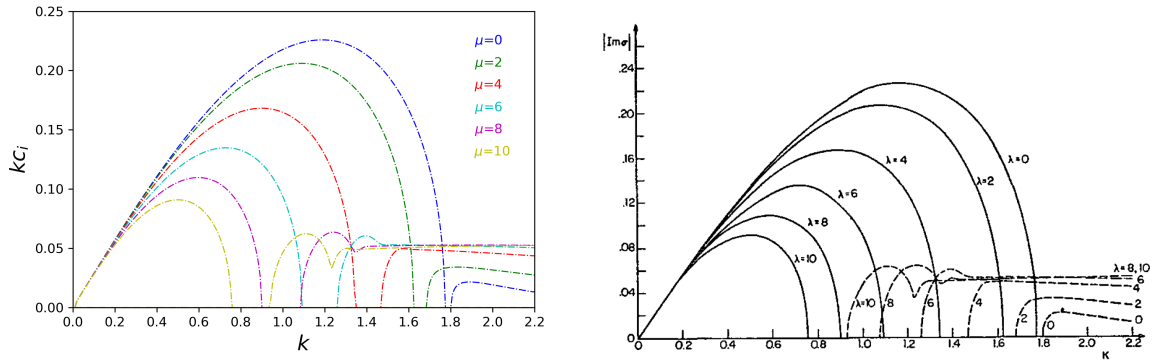


Figure 4.2: (Left): Growth rates as a function of the zonal wavenumber k for the Stone's formulation of the Eady problem calculated with Richardson number $Ri = 1$ and selected values of the meridional wavenumber μ. (Right): As in the left panel, but originally from Stone [1970, Figure 2] with the meridional wavenumber denoted by λ.

3. Two-dimensional Equatorial Jets

Following the linear stability analysis of Proehl [1996, 1998], we have solved the equations of motion (4.21)-(4.23) in the two-dimensional domain bounded latitudinally by rigid walls at $y = \pm L$, and bounded vertically by a rigid wall at $z = -D$ and a rigid lid at $z = 0$. The mean zonal flows consist of a variety of increasingly realistic, idealised, equatorial zonal jets constructed from a linear combination of Gaussian jets, with corresponding mean density fields in thermal wind balance and assuming a constant buoyancy frequency. A total of nine equatorial zonal flows are considered, ranging from single isolated Gaussian jets to combinations of these jets representing a realistic equatorial Pacific current structure. Proehl [1996] considered basic states which were meridionally symmetric about the equator and solved the problem only in the southern half of the domain to exploit the symmetry of the problem and reduce computational cost. We solved the linear stability problem on an equivalent domain as Proehl, with a meridional half-width $L = 10^\circ$ and depth $D = 1000$m, and with $(ny, nz) = (111, 50)$ meridional and vertical grid points,

respectively. Proehl [1998] added meridional asymmetry to the basic state. For these cases, we solved the linear stability over the same domain as Proehl, with meridional half-width $L = 8°$ and depth $D = -250$m, and with $(ny, nz) = (60, 50)$ meridional and vertical grid points, respectively. In all cases, we solved the equations of motion subject to no normal flow boundary conditions at the meridional and vertical edges of the domain.

We compare our findings to Proehls original results for the sixth case which is representative of the equatorial currents with a meridionally asymmetric SEC as shown in figure 4.3.

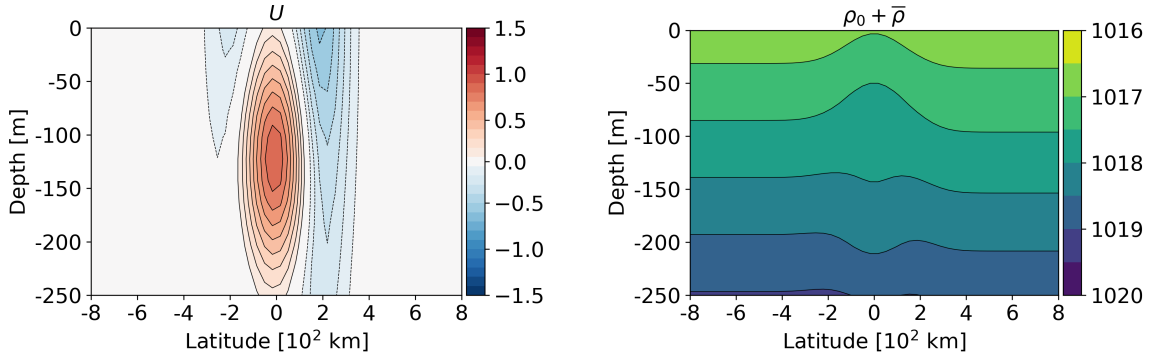


Figure 4.3: (Left): Mean zonal velocity $U(y, z)$ [ms^{-1}] from case C of Proehl [1998]. Contours are every 0.1ms^{-1} with solid/dashed contours denoting eastward/westward flow. (Right): Mean potential density $\overline{\rho}(y, z)$ [kgm^{-3}] from case C of Proehl [1998].

We obtained two unstable modes that agree with those found by Proehl, as shown in figure 4.4 and whose stability characteristics are summarised in table 4.1. The unstable modes are both slightly shorter and slower than the corresponding unstable modes found by Proehl. The amplitude of the zonal velocity perturbation, shown in figure 4.5, has the

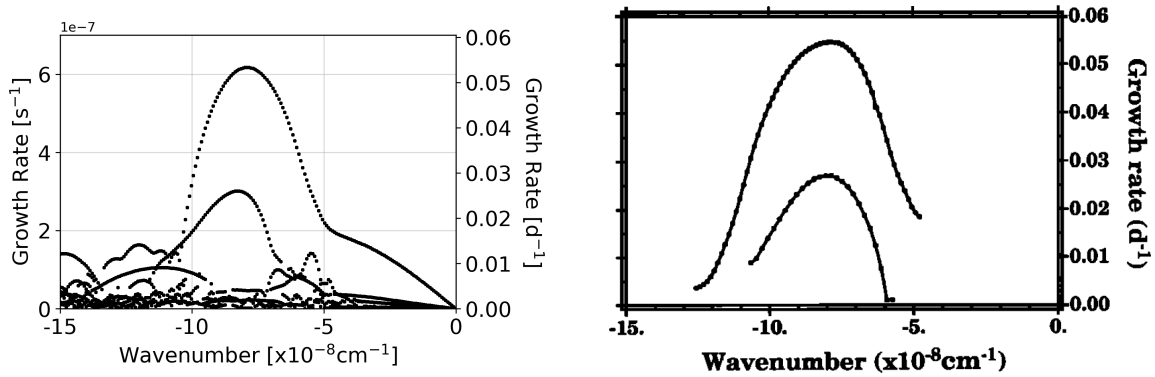


Figure 4.4: (Left): Growth rates for case C of Proehl [1998] obtained by solving the generalised eigenvalue problem over a range of zonal wavenumbers k. (Right): As in the left panel but from Proehl [1998, Figure 12].

	Wavelength [km]	Phase Speed [m/s]	Period [d]	E-folding Time [d]
Rees	**786**	**-0.227**	**39.9**	**18.7**
Proehl	801	-0.232	39.9	18.0
Rees	**757**	**-0.409**	**21.4**	**38.4**
Proehl	795	-0.421	21.9	37.0

Table 4.1: Stability characteristics of the two unstable modes obtained by solving the linear stability problem for case C of Proehl [1998]. Results obtained from our numerical solver are labelled with "Rees" and are highlighted in bold.

same key features as that of Proehl, namely the meridional asymmetry of the zonal velocity perturbation associated with the asymmetry of the westward flowing SEC branches. The spatial structure of the phase of the zonal velocity perturbation is similar to Proehl but the values of the phase do not agree. As shown in figure 4.6, the eddy energy conversions and eddy pressure fluxes obtained from our numerical solver agree with the original results of Proehl.

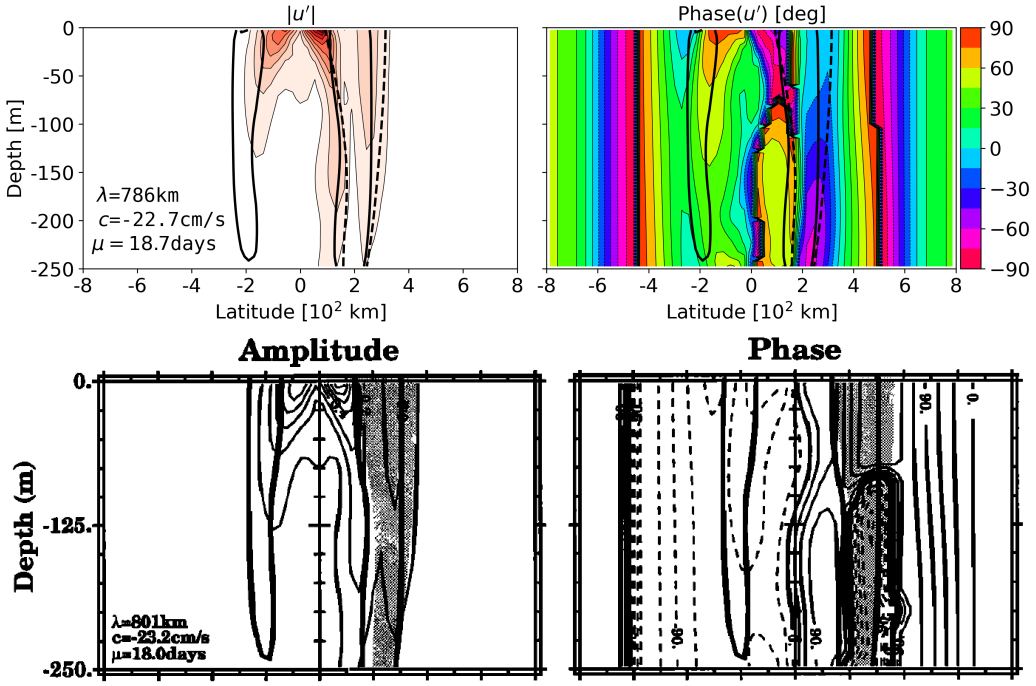


Figure 4.5: (Upper Left): Amplitude of the zonal velocity perturbation for the fastest growing instability from figure 4.4. For comparison with Proehl, we have normalised the amplitude to 1 with the stability characteristics of the most unstable mode stated in the bottom left of the panel. Contours are evenly spaced at every 0.1. The solid black line denotes locations where the meridional PV gradient is zero. The thick dashed line denotes the critical level locations where $U = c_r$. (Upper Right): Phase of the zonal velocity perturbation of the most unstable mode. (Bottom): As in the upper panels, but originally from Proehl [1998, Figure 13]. Proehl uses hatching to denote the locations where $U - c_r < 0$ hence our thick dashed lines correspond to the edges of this hatched region.

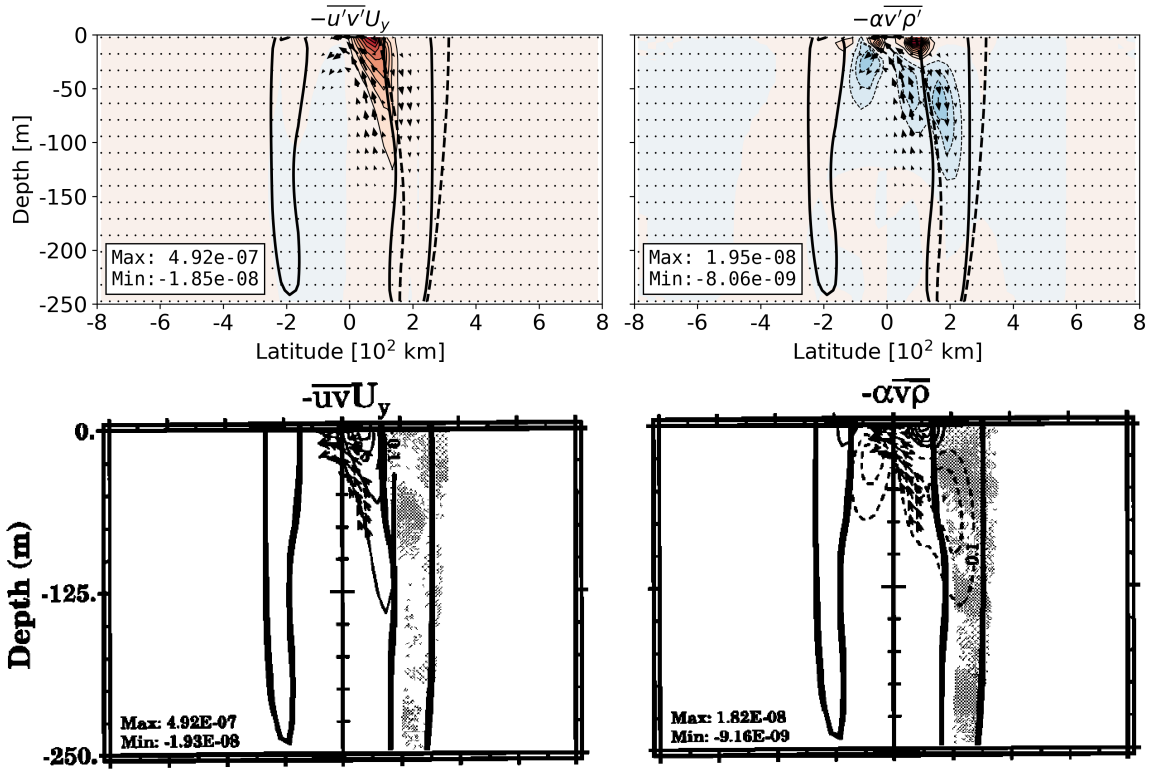


Figure 4.6: Spatial structure of barotropic (left) and baroclinic (right) conversions for the most unstable mode obtained from our findings (top) and Proehls original findings (bottom). All contoured figures are independently normalised to 1 with the maximum and minimum stated in the bottom left and with contour intervals every 0.1. For comparison with Proehl, we normalised the barotropic conversion such that the maximum value agreed with that of Proehl. Superposed are vectors for the normalised eddy pressure fluxes ($\overline{v'p'}, \overline{w'p'}$).

Comparing the findings from our numerical solver for each of the cases studied by Proehl, we generally find similar levels of agreement to those described above. This demonstrates that our numerical solver for the linear stability problem gives good results for two-dimensional equatorial linear stability problems.

Chapter 5

Linear Stability Analysis - Results

5.1 Results

In this chapter we extend our linear stability analysis, from comparative investigations with mean zonal flows comprising of linear combinations of zonal Gaussian jets as in Proehl [1996, 1998], to investigate the stability of mean zonal velocity and mean density fields obtained from the fully nonlinear AOGCM described in chapter 3. We consider mean fields immediately prior to TIW development and this corresponds to fields during the TIW-active period (July-August) which we had previously termed in chapter 3. We also consider mean fields from periods after TIW activity had ceased. This corresponds to fields during the TIW-inactive period (March-April). The findings associated with the TIW-inactive period are indicative of stability, and since the focus of this chapter is on instabilities of the mean flows, we do not present figures for the TIW-inactive case. To obtain the two-dimensional mean zonal velocity $U(y, z)$ and mean density $\overline{\rho}(y, z)$, we zonally average these fields over the longitudinal range 110°W to 160°W. Observational data has indicated active and energetic TIWs within this region [Baturin and Niiler, 1997]. We term the linear stability analysis of the mean fields obtained from the medium and high resolution integrations in chapter 3 as models M-LIN and H-LIN, respectively. In figure 5.1, we can identify each component of the equatorial current structure. The EUC is a strong eastward flowing subsurface current centered on the equator with a core around 100m. The NECC is an eastward flowing current located between $4° - 7°$N that transports warm western Pacific waters eastward. The SEC is a westward flowing current split into two branches, namely the SECS and SECN. We identify the signal of a warm NECC in the mean density evident from the dip in the isopycnals at 5° which is not evident in the southern part of the domain. Similarly, the shoaling of higher density waters indicates that the zonally averaged mean fields have captured the presence of an equatorial cold tongue. The structure of the meridional gradient in PV indicates that

instability is possible. Comparing the mean fields between the medium and high resolution integrations, we find that there are minimal differences aside from the structure of the meridional PV gradient whereby the region of weakly negative PV north of the equator near the surface is smaller for model H-LIN.

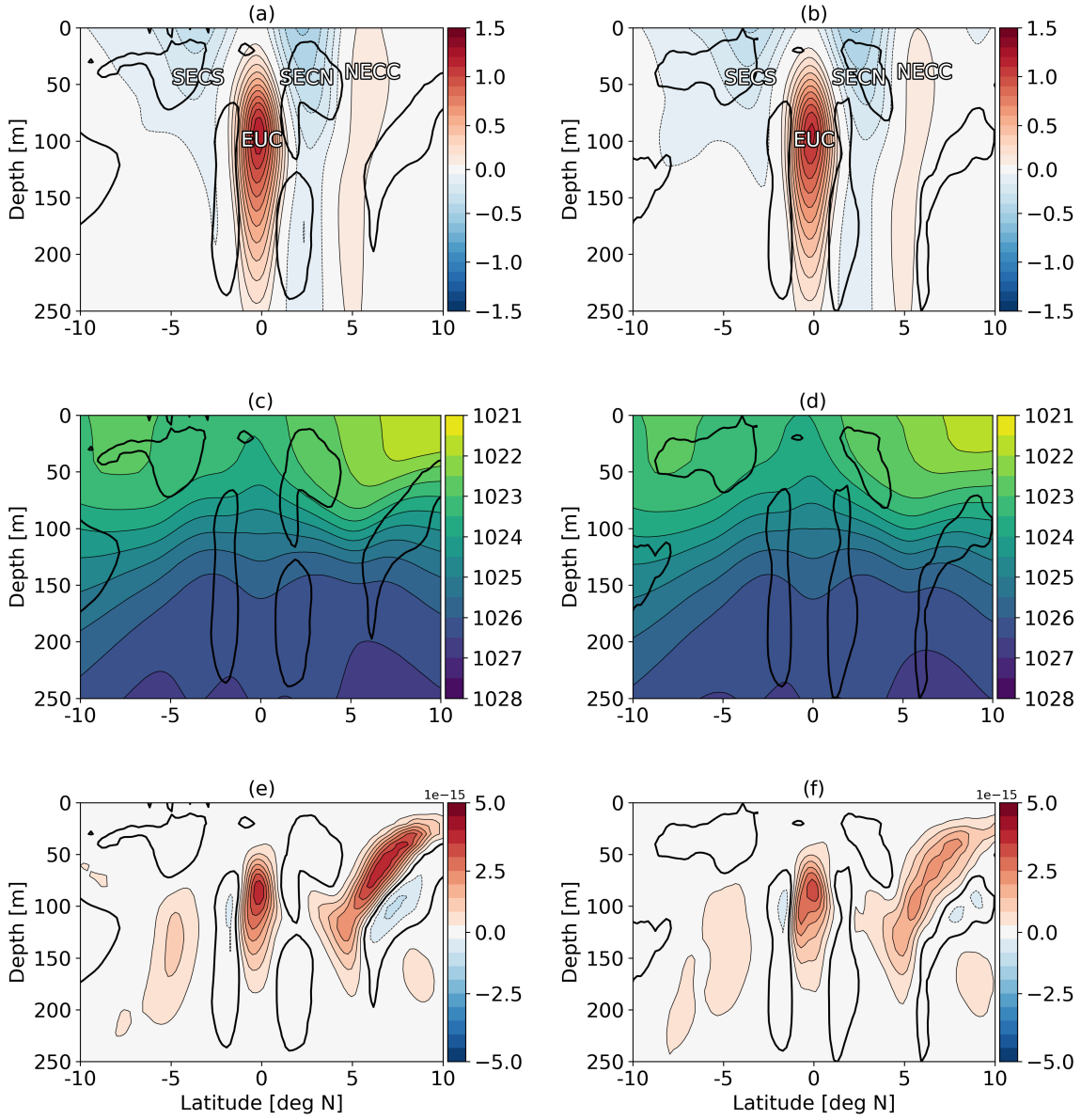


Figure 5.1: Depth-latitude plots of mean zonal velocity $U(y,z)[\mathrm{ms}^{-1}]$ ((a)-(b)), mean density $\rho_0 + \overline{\rho}(y,z)[\mathrm{kgm}^{-3}]$ ((c)-(d)), and meridional gradients of PV $[\mathrm{m}^{-2}\mathrm{s}^{-1}]$ ((e)-(f)) for model M-LIN (left column) and model H-LIN (right column). For (a) and (b), thin contours are every $0.1\mathrm{ms}^{-1}$ with solid/dashed contours denoting eastward/westward velocities, respectively. For (c)-(d), thin contours are every $0.5\mathrm{kgm}^{-3}$. For (e)-(f), thin contours are every $5 \times 10^{-16}\mathrm{m}^{-2}\mathrm{s}^{-1}$ with solid/dashed contours denoting positive/negative values, respectively. In all figures, we superpose thick solid contours denoting the regions where $Q_y = 0$.

We perturb about a mean state motivated by a fully nonlinear AOGCM and therefore this mean state contains physics, such as surface wind forcing or vertical mixing in the near-surface mixed layer, which are not captured by our highly idealised linear model. Therefore, the mean fields that we impose do not satisfy the system of equations (4.16)-(4.20). However, we argue that there is value to be gained from investigating the linear stability of these mean fields in the framework of a highly idealised linear model. We solve the system of equations (4.21)-(4.23) with the prescribed mean zonal velocity and density fields. The data from the coupled model is defined on a non-uniformly spaced grid of $(ny, nz) = (123, 47)$ points which we interpolate onto a uniform grid of $(150, 100)$ points before solving.

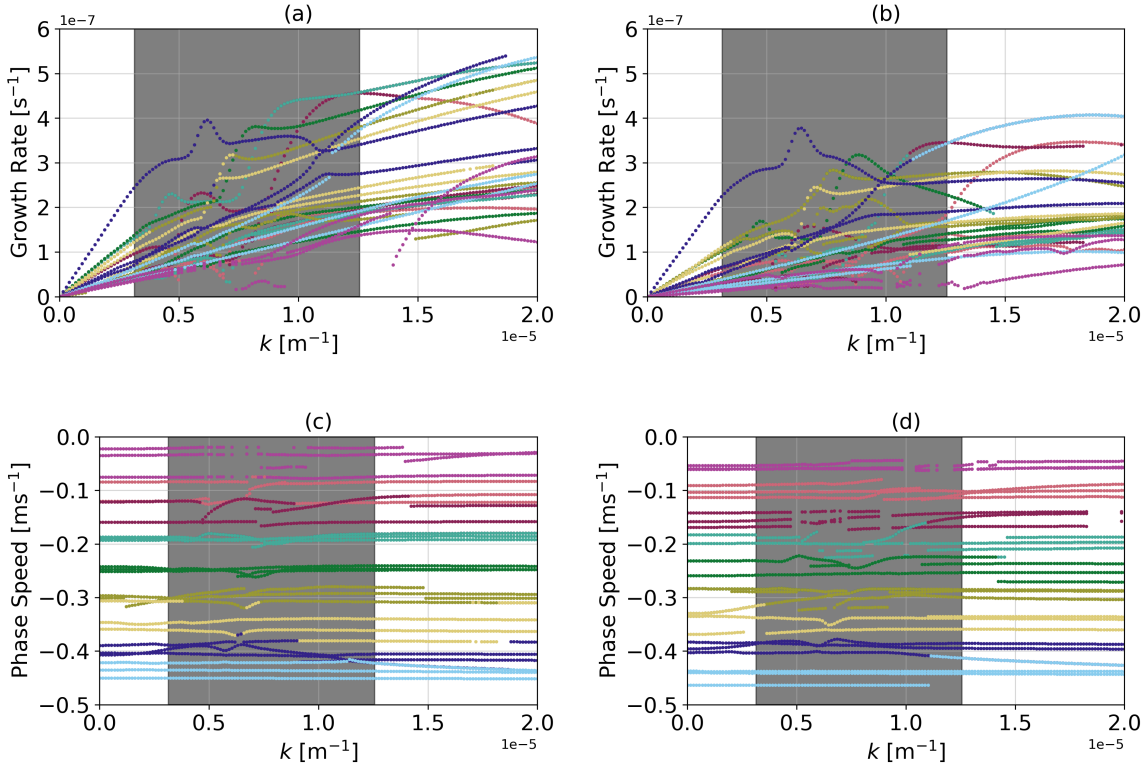


Figure 5.2: Growth rates kc_i [s^{-1}] ((a)-(b)) and phase speeds c_r [ms^{-1}] ((c)-(d)) for unstable modes as a function of zonal wavenumber k for model M-LIN ((a) and (c)) and model H-LIN ((b) and (d)). At each wavenumber and eigenvalue guess, which we use to initialise the numerical solver for the generalised eigenvalue problem, we solve the linear stability problem for the 3 most unstable modes (largest imaginary parts) and colour each marker corresponding to the real part of our initial eigenvalue guess. These initialisations range from $c_r = -0.05$ to $c_r = -0.45$ in steps of 0.05. The wavenumber range highlighted in grey denotes the range of wavelengths between $\lambda = 500$km and $\lambda = 2000$km in between which TIWs have been observed.

Figure 5.2 shows that the mean fields for both models M-LIN and H-LIN are unstable. In

Integration	Wavelength [km]	Phase Speed [m/s]	Period [d]	E-folding Time [d]
M-LIN	1017	-0.391	30.1	29.6
H-LIN	974	-0.382	29.5	30.6

Table 5.1: Stability characteristics of the unstable modes for models M-LIN and H-LIN.

each case, the most unstable mode occurs at short wavelengths which lie outside the range expected of TIWs in both observations or numerical models. For model M-LIN, we calculated the growth rates up to $k = 2 \times 10^{-4}\text{m}^{-1}$ and found that the most unstable mode occurs at $k = 1.3 \times 10^{-4}\text{m}^{-1}$ which corresponds to a wavelength of $\lambda = 48.3$km. The perturbations corresponding to this unstable mode (not shown) are strongest above 50m depth, lie between $5^\circ - 8^\circ$N, and primarily draw their energy from baroclinic conversion associated with the near vertical isopycnals north of the equator. These submesoscale instabilities may be generated by the equatorial mixed layer where there are signifiant turbulent transports and vertical mixing, the representation of which is not accurate in our linear model.

Unlike in Proehls idealised cases, there are no clear branches containing the global maximum in the growth rate. It is possible that perturbing about a basic state that is not in thermal wind balance, and hence does not solve the linearised equations of motion, results in unrealistic unstable modes appearing as solutions of the generalised eigenvalue problem. Another possibility is that the zero contours of the meridional PV gradient do not coincide with a single isotach. There could be instabilities associated with different values of c_r for which the critical level, $U = c_r$, coincides with the location of $Q_y = 0$. In models M-LIN and H-LIN, we identify distinct branches of unstable modes with similar structures between the integrations. The mean fields for models M-LIN and H-LIN have slight differences, therefore we might expect the branches of unstable modes to have similar growth rates. However, we find that nearly all branches of unstable modes for models H-LIN are weaker in growth rate than their counterparts in model M-LIN. We identify a single branch in both models M-LIN and H-LIN, given by purple dots, which have similar local maxima at wavenumbers $k = 6.18 \times 10^{-6}\text{m}^{-1}$ and $k = 6.45 \times 10^{-6}\text{m}^{-1}$, respectively. The properties of these unstable modes are provided in Table 5.1.

Since we have assumed solutions that vary zonally as $\exp(ikx)$, we are able to calculate the three-dimensional structure of these unstable modes which are shown in figure 5.3. Figure 5.3 shows significant similarities between the unstable modes from models M-LIN and H-LIN. We find alternating patterns of meridional velocity at the equator associated with the instability. Within the Tropical instability vortices (TIVs), the instability acts to

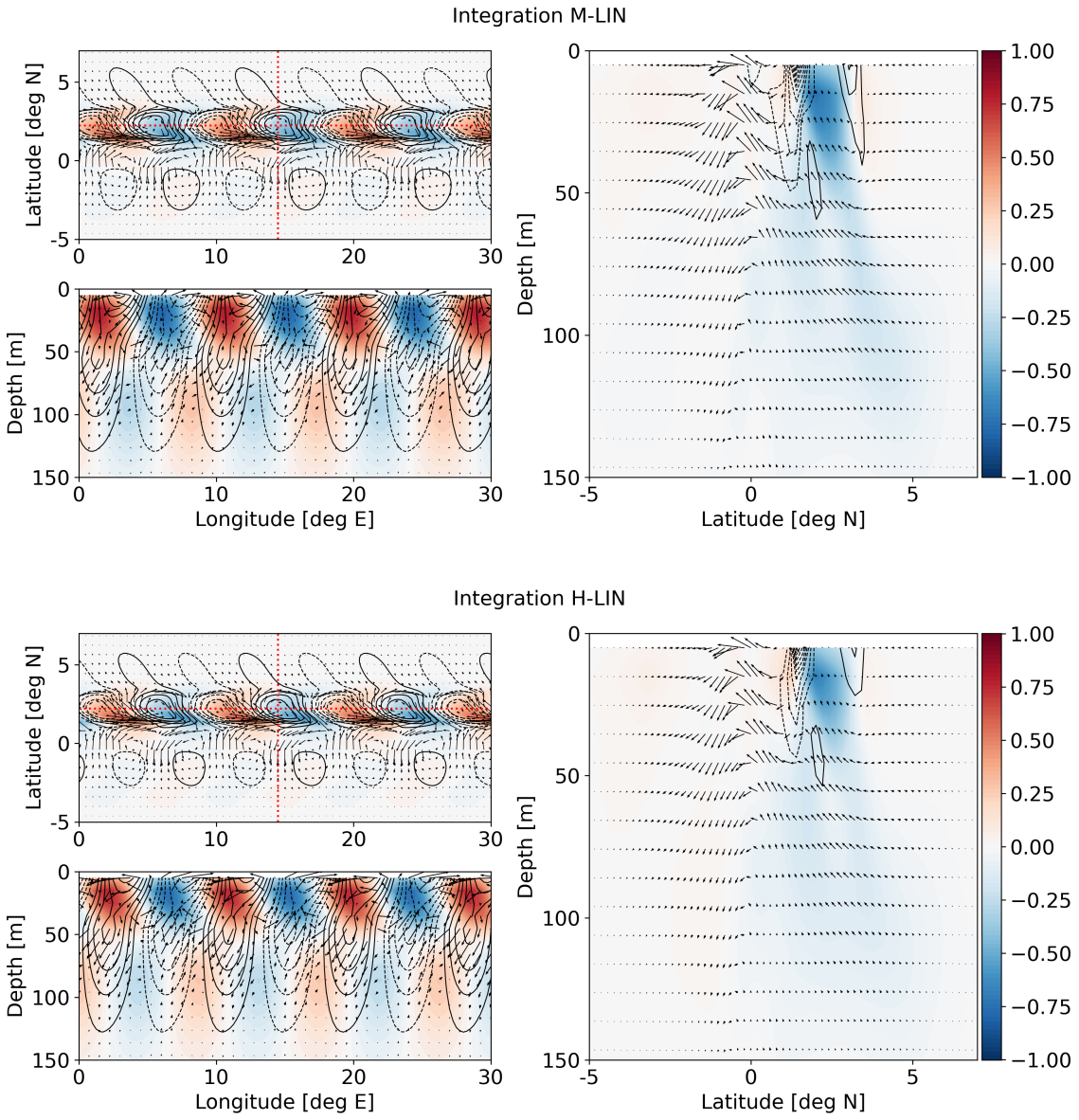


Figure 5.3: Three-dimensional structure of the eigenvectors for the fastest growing instabilities at wavenumber $k = 6.18 \times 10^{-6}\mathrm{m}^{-1}$ for model M-LIN (upper figure) and $k = 6.45 \times 10^{-6}\mathrm{m}^{-1}$ for model H-LIN (lower figure). The figures for each model are structured as follows. In the upper left, we plot a latitude-longitude slice of the perturbations of density ρ' (colour), pressure p' (solid/dashed contours) and horizontal velocity (u', v') (quivers) at a depth of 5m. Red dotted lines are used to denote the locations where we take cross sections for the depth-longitude and depth-latitude plots. In the lower left, we plot a depth-longitude slice, at 2.5°N for models M-LIN and H-LIN, of the perturbations of density (colour), meridional velocity (solid/dashed contours) and zonal and vertical velocities (u',w') (quivers) at a latitude of 2.5°N. On the right, we plot a depth-latitude slice, at 15°E for models M-LIN and H-LIN, of the perturbations of density (colour), zonal velocity (solid/dashed contours) and meridional and vertical velocities (v', w') (quivers). We have normalised the eigenvectors such that $\max(|\rho'|) = 1$.

transport deeper warmer waters, associated with the NECC north of the equator, upwards and towards the equator therefore offsetting the cooling by the equatorial cold tongue. Patterns in the density and horizontal velocity at the surface indicate anti-cyclonic vortices north of the equator which act to advect cold denser waters associated with the equatorial cold tongue northwards and exchange with warmer off-equatorial waters associated with the NECC advecting equatorwards.

The net effect of TIWs acting to warm the equatorial cold tongue is shown in figure 5.4. The meridional eddy heat flux is positive north of the equator which indicates northward transport of cold equatorial waters and equatorward transport of warm waters associated with the alternating patterns in the meridional velocity and density perturbations north of the equator. The zonal eddy momentum flux shown in figure 5.4 is indicative of an eastward momentum convergence at 2°N which coincides with the core of the SECN and hence suggests that TIWs act to weaken the SECN and its meridional shear with the EUC.

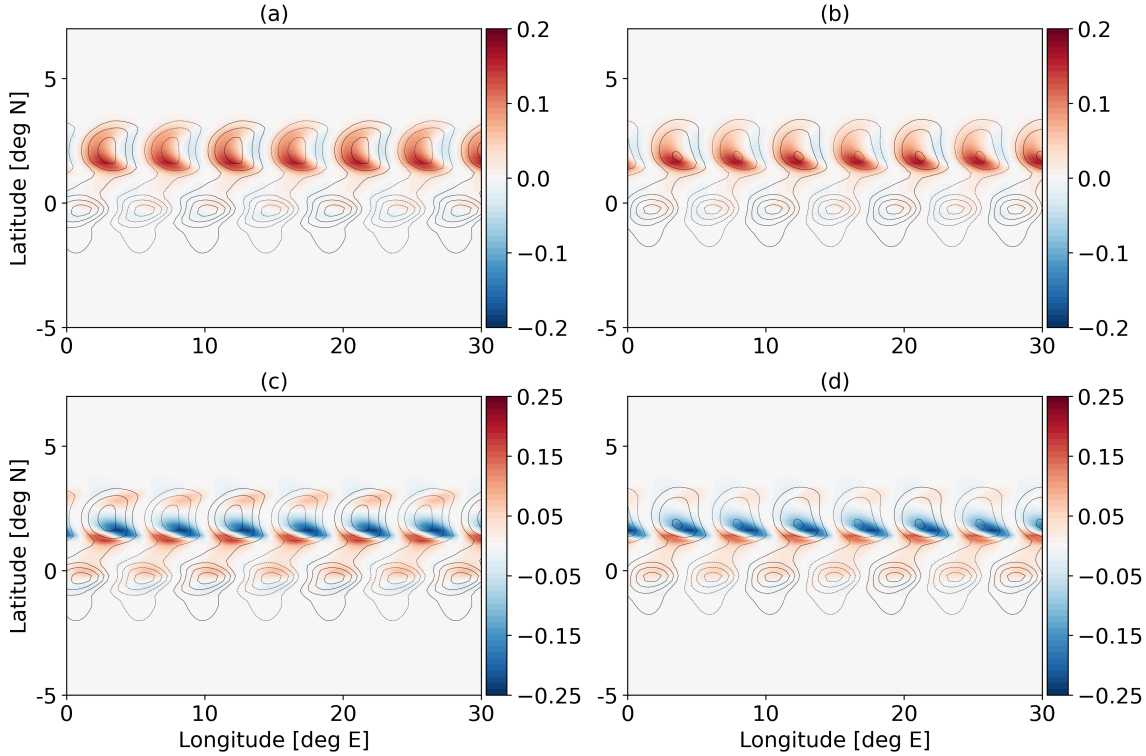


Figure 5.4: Latitude-longitude slice of the meridional eddy heat flux $\overline{v'\rho'}$ (colour) ((a),(b)) and zonal eddy momentum flux $\overline{u'v'}$ (colour) ((c),(d)) at a depth of 5m for models M-LIN (left column) and H-LIN (right column). Superposed are solid (dashed) contours of meridional velocity perturbations denoting positive (negative) values.

Figure 5.5 shows that baroclinic conversions are strongest within the SECN with preference towards the equatorward flank associated with the strongly tilted isopycnals.

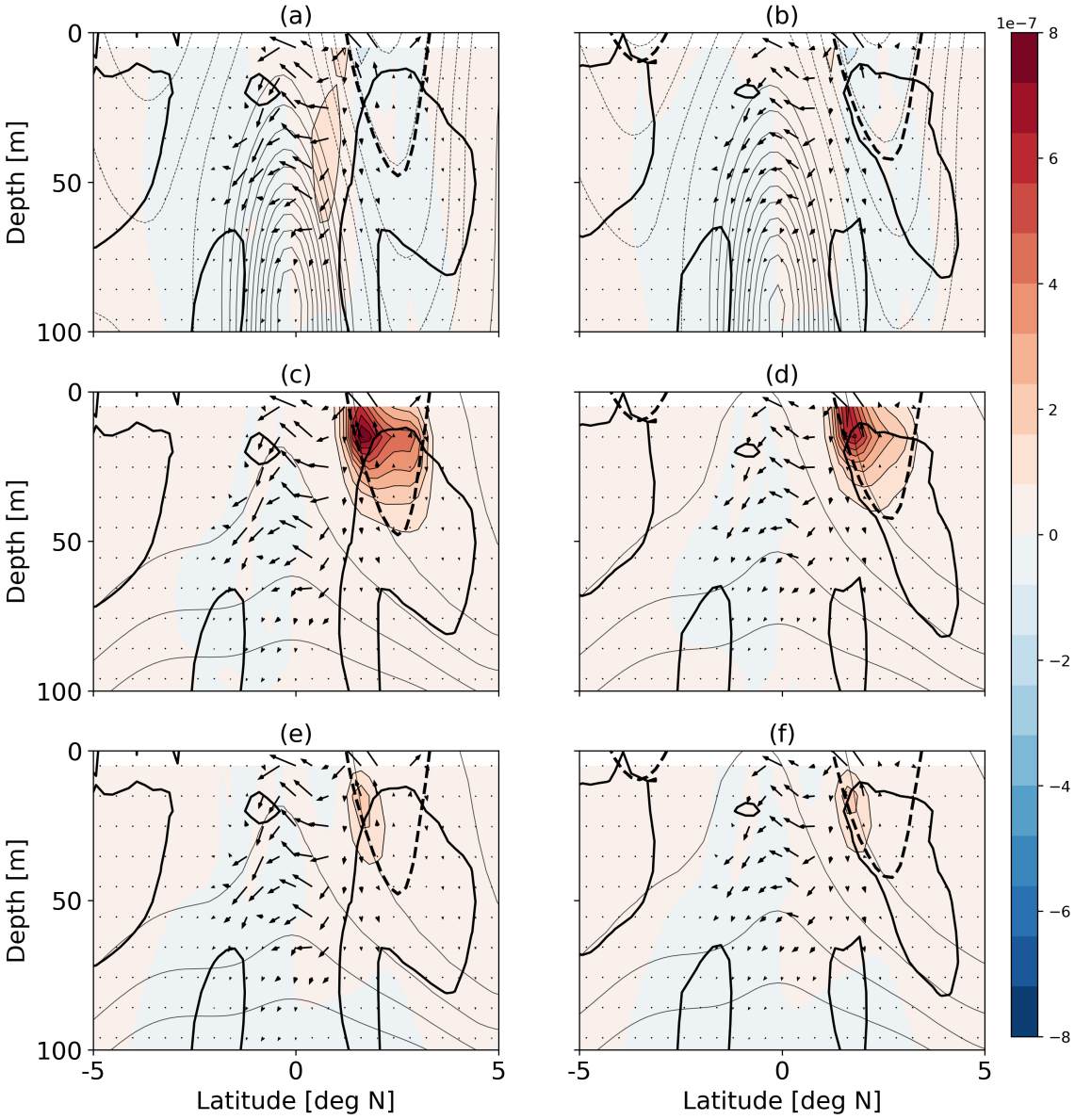


Figure 5.5: Spatial structure of the energy conversion mechanisms for the fastest growing instability at wavenumber $k = 6.18 \times 10^{-6}\mathrm{m}^{-1}$ for model M-LIN (left column) and wavenumber $k = 6.45 \times 10^{-6}\mathrm{m}^{-1}$ for model H-LIN (right column). ((a)-(b)): Barotropic conversion $-\overline{u'v'}U_y$. ((c)-(d)): Baroclinic conversion $-\alpha\overline{v'\rho'}$. ((e)-(f)): Eddy potential energy to eddy kinetic energy conversion $-(g/\rho_0)\overline{w'\rho'}$. On each plot, we superpose the eddy pressure work fields ($\overline{v'p'}$, $\overline{w'p'}$) as quivers. For barotropic conversion, we superpose the mean zonal velocity as contours, whereas for the other conversion mechanisms we superpose the mean density field. On each plot we have superposed the locations where $Q_y = 0$ (thick solid contour) and $U = c_r$ (thick dashed contour).

Although contributing nothing to the changing total eddy energy budget, there is conversion from eddy potential to eddy kinetic energy on the equatorward flank of the SECN at approximately the same location as the maximum in baroclinic conversion. The

Integration	BTC ($-\overline{u'v'}U_y$)	BCC ($-\alpha\overline{v'\rho'}$)	KHC ($-\overline{u'w'}U_z$)
M-LIN	10.5%	90.1%	-0.6%
H-LIN	9.1%	90.2%	0.7%

Table 5.2: Domain average eddy energy conversions, for models M-LIN and H-LIN, as a percentage of the rate of change of total eddy energy.

model M-LIN differs from model H-LIN whereby there is a greater contribution from barotropic conversion along the northern flank of the EUC which is not present in model H-LIN. The eddy pressure fluxes indicate that energy is radiated from the equatorward flank of the SECN across the equator to the southern flank of the EUC. We find that the maximum in baroclinic conversion lies almost directly at the location where the zero in the meridional PV gradient meets the critical level.

We characterise the contributions from energy conversion mechanisms as percentages of the domain averaged rate of change of total eddy energy with respect to time. The eddy energy conversion between eddy kinetic and eddy potential energies is not included since this term does not contribute to total eddy energy budget. Table 5.2 shows that baroclinic conversion dominates the instability for both integrations. Barotropic conversion contributions are weaker, but the weakest contribution comes from Kelvin-Helmholtz conversions which are near negligible and are therefore not plotted.

5.2 Shortcomings and Limitations

In light of our existing findings from the linear model, we acknowledge that there are certain shortcomings and limitations which we now discuss and for which we propose possible solutions. Firstly, our linear model fails to obtain distinct branches for unstable modes unlike Proehl [1996, 1998], whereby typically one or two distinct branches of unstable modes are found. One reason for this discrepancy is that our linear model detects instabilities whose wavelengths are too short to be associated with TIWs. These instabilities are likely due to the simplification of our model whereby we have neglected to include physics such as surface wind forcing and vertical mixing which is important in the near-surface mixed layer. One method to improve this aspect would be to introduce a biharmonic viscosity scheme which acts to selectively dampen grid-scale noise whilst preserving larger structures [McCreary Jr and Yu, 1992]. Another approach could be to incorporate an Ekman pumping boundary condition at the base of the mixed layer to account for the vertical transport of momentum and capture the influence of vertical mixing. Although we have compared our findings with the existing literature to ensure

that the linear solver that we employed is accurate, we could improve the reliability of this solver by utilising an independent numerical method, other than finite differences, such as a Chebyshev collocation method. We had used this discretisation scheme to solve the one-dimensional Rayleigh-Kuo and Eady problems. However, due to time constraints, we did not make further progress with this method.

By addressing these limitations, we can enhance the capabilities of our linear model whilst maintaining its idealised representation of the equatorial Pacific ocean that allows us insight into the dynamics and behaviour of TIWs.

5.3 Discussion

In this chapter, we have solved the linearised equations of motion (4.21)-(4.23) using mean fields representative of periods prior to TIW growth. We find that the most unstable mode occurs at an unrealistic short wavelength, which raises concerns about the limitations of this highly idealised linear model. For both models M-LIN and H-LIN, we find unstable modes along similar growth rate branches whose properties resemble the 33 day wave documented in the literature [Lyman et al., 2007]. However, our model fails to capture the unstable mode representative of the 17 day wave. It is uncertain as to whether we can expect our linear model to capture these 17 day waves. Some linear models successfully obtain this wave [Yu et al., 1995], whereas experimental studies [Luther and Johnson, 1990] and numerical investigations [Zhou and Boyd, 2009] suggest that this mode emerges later in TIW development, beyond periods whereby linear theory holds. The use of an idealised fully nonlinear model of the equatorial Pacific will allow us to investigate the properties of TIWs throughout their life-cycle, and is not limited to the early (linear) stages of TIW development.

Chapter 6

Idealised Nonlinear Model

6.1 Model Description

To expand our investigation of Tropical Instability Waves (TIWs) beyond a zonally averaged idealised linear model of the equatorial Pacific, we employ a three-dimensional idealised nonlinear configuration. We build such a model of the equatorial Pacific by adapting the CANAL test case from the NEMO ocean model which is defined as an east-west canal with adjustable dimensions. The nonlinear model solves the Primitive equations with variables defined on the staggered Arakawa C-grid [Arakawa, 1966]. We employ an equatorial beta-plane approximation with the domain centered on the equator, spanning a length of 5550km, a width of 3330km, and featuring a flat ocean bottom with a depth of 1km. The domain is zonally periodic and bounded meridionally and at the bottom of the domain by rigid walls where free-slip boundary conditions are applied. The domain is bounded above by the free surface $\eta(x, y, t)$, where η is the sea surface height relative to $z = 0$, and which is subject to kinematic and dynamic boundary conditions. There are no external forces such as surface wind stresses or surface heating.

To initialise the model, we input zonally invariant zonal velocity, temperature, and sea surface height fields calculated by zonally and temporally averaging data from the coupled model in Chapter 3, specifically those of integrations M and H for the TIW-active and TIW-inactive periods. These fields are then interpolated onto a uniform grid and broadcasted in longitude over the zonal extent of the domain. We set the input meridional velocity and salinity fields as 0ms^{-1} and 35psu everywhere, respectively. A perturbation is applied to the temperature field by adding random noise drawn from a uniform distribution $\mathcal{U}(-0.05, 0.05)$. The model is run in two configurations depending on the horizontal resolution. The medium resolution model (integration M-NONLIN) has horizontal and vertical grid spacings of 27.75km and 10m, respectively. The equation of

state used is EOS80, and the model is run for 2 years with a timestep of 20 minutes. The high resolution version (integration H-NONLIN) has horizontal and vertical grid spacings of 9.25km and 10m, respectively. The equation of state used is TEOS10, and we attempted to run the model for 2 years with a timestep of 10 minutes. Due to unrealistic velocities ($|u| > 10\text{ms}^{-1}$) at day 313, integration H-NONLIN aborted its run and therefore we only have data up to day 313. Running the model at a shorter timestep of 5 minutes did not fix the issue. The mean fields are extracted from a fully nonlinear coupled model which contains additional physics, such as surface wind forcing, that is not present within our idealised nonlinear model. We found that model outputs exhibited meridional "sloshing" starting from day 0. This sloshing had a signal with a period of less than 10 days. Since this sloshing is due to the initialisation of the model and has a period shorter than any observed TIWs, we filter the output data with a Butterworth filter [Butterworth et al., 1930] to damp signals less than 10 days. For both M-NONLIN and H-NONLIN integrations, outputs are averaged over 6-hour intervals. Further details for the NEMO model can be found in Madec [2016]. Outputs of the idealised nonlinear model for initial fields representative of the TIW-inactive period are stable (not shown). In this chapter, we present outputs for the TIW-active period only.

6.2 Nonlinear Eddy Energy Budget

Before discussing the outputs from the idealised nonlinear model for the TIW-active period, we derive the eddy kinetic and eddy potential energy budgets. This allows us to extend our discussion from chapter 5 by investigating which eddy energy conversion mechanisms are important throughout the TIW life-cycle and not only the early (linear) phase of TIW-activity from our idealised linear model. Recall from chapter 4 that the governing equations for the continuous, three-dimensional, inviscid, hydrostatic, unforced motions of an incompressible, rotating, stratified fluid subject to Boussinesq and equatorial beta plane approximations are

$$\frac{\partial u}{\partial t} + u\frac{\partial u}{\partial x} + v\frac{\partial u}{\partial y} + w\frac{\partial u}{\partial z} - \beta yv = -\frac{1}{\rho_0}\frac{\partial p}{\partial x}, \tag{6.1}$$

$$\frac{\partial v}{\partial t} + u\frac{\partial v}{\partial x} + v\frac{\partial v}{\partial y} + w\frac{\partial v}{\partial z} + \beta yu = -\frac{1}{\rho_0}\frac{\partial p}{\partial y}, \tag{6.2}$$

$$\frac{\partial p}{\partial z} = -\rho g, \tag{6.3}$$

$$\frac{\partial \rho}{\partial t} + u\frac{\partial \rho}{\partial x} + v\frac{\partial \rho}{\partial y} + w\frac{\partial \rho}{\partial z} = 0, \tag{6.4}$$

$$\frac{\partial u}{\partial x} + \frac{\partial v}{\partial y} + \frac{\partial w}{\partial z} = 0. \tag{6.5}$$

We impose no-normal flow boundary conditions as

$$v = 0, \qquad y = \pm 15^\circ, \tag{6.6}$$

$$w = 0, \qquad z = -1000, 0. \tag{6.7}$$

We expand the velocity, pressure and density fields about a zonally invariant background state as follows:

$$u(x,y,z,t) = U(y,z,t) + u'(x,y,z,t), \tag{6.8}$$

$$v(x,y,z,t) = V(y,z,t) + v'(x,y,z,t), \tag{6.9}$$

$$w(x,y,z,t) = W(y,z,t) + w'(x,y,z,t), \tag{6.10}$$

$$p(x,y,z,t) = \overline{p}(y,z,t) + p'(x,y,z,t), \tag{6.11}$$

$$\rho(x,y,z,t) = \rho_0 + \overline{\rho}(y,z,t) + \rho'(x,y,z,t), \tag{6.12}$$

where primes are used to denote perturbations from the mean. We have also separated the mean density into components as the constant reference background density ρ_0 and the mean background density structure $\overline{\rho}(y,z,t)$. Substituting (6.8)-(6.12) into (6.1)-(6.5) yields, at leading order, the following equations of motion for the mean fields:

$$\frac{\partial U}{\partial t} + V\frac{\partial U}{\partial y} + W\frac{\partial U}{\partial z} - \beta y V = 0, \tag{6.13}$$

$$\frac{\partial V}{\partial t} + V\frac{\partial V}{\partial y} + W\frac{\partial V}{\partial z} + \beta y U = -\frac{1}{\rho_0}\frac{\partial \overline{p}}{\partial y}, \tag{6.14}$$

$$\frac{\partial \overline{p}}{\partial z} = -(\rho_0 + \overline{\rho})g, \tag{6.15}$$

$$\frac{\partial \overline{\rho}}{\partial t} + V\frac{\partial \overline{\rho}}{\partial y} + W\frac{\partial \overline{\rho}}{\partial z} = 0, \tag{6.16}$$

$$\frac{\partial V}{\partial y} + \frac{\partial W}{\partial z} = 0. \tag{6.17}$$

At next-to-leading and higher order, the perturbation equations of motion are given by

$$\frac{\partial u'}{\partial t} + U\frac{\partial u'}{\partial x} + V\frac{\partial u'}{\partial y} + W\frac{\partial u'}{\partial z} + u'\frac{\partial u'}{\partial x} + v'\frac{\partial u'}{\partial y} + w'\frac{\partial u'}{\partial z} + v'\frac{\partial U}{\partial y} + w'\frac{\partial U}{\partial z} - \beta y v' = -\frac{1}{\rho_0}\frac{\partial p'}{\partial x}, \tag{6.18}$$

$$\frac{\partial v'}{\partial t} + U\frac{\partial v'}{\partial x} + V\frac{\partial v'}{\partial y} + W\frac{\partial v'}{\partial z} + u'\frac{\partial v'}{\partial x} + v'\frac{\partial v'}{\partial y} + w'\frac{\partial v'}{\partial z} + v'\frac{\partial V}{\partial y} + w'\frac{\partial V}{\partial z} + \beta y u' = -\frac{1}{\rho_0}\frac{\partial p'}{\partial y}, \tag{6.19}$$

$$\frac{\partial p'}{\partial z} = -\rho' g, \tag{6.20}$$

$$\frac{\partial \rho'}{\partial t} + \overline{u}\frac{\partial \rho'}{\partial x} + \overline{v}\frac{\partial \rho'}{\partial y} + \overline{w}\frac{\partial \rho'}{\partial z} + u'\frac{\partial \rho'}{\partial x} + v'\frac{\partial \rho'}{\partial y} + w'\frac{\partial \rho'}{\partial z} + v'\frac{\partial \overline{\rho}}{\partial y} + w'\frac{\partial \overline{\rho}}{\partial z} = 0, \tag{6.21}$$

$$\frac{\partial u'}{\partial x} + \frac{\partial v'}{\partial y} + \frac{\partial w'}{\partial z} = 0. \tag{6.22}$$

The eddy kinetic energy budget is obtained from

$$u' \times (6.18) + v' \times (6.19). \tag{6.23}$$

Using (6.20) and (6.22) in (6.23), and then zonal averaging, we obtain

$$\frac{\partial}{\partial t}\left(\frac{1}{2}\left(\overline{u'^2}+\overline{v'^2}\right)\right) = -V\frac{\partial}{\partial y}\left(\frac{1}{2}\left(\overline{u'^2}+\overline{v'^2}\right)\right) - W\frac{\partial}{\partial z}\left(\frac{1}{2}\left(\overline{u'^2}+\overline{v'^2}\right)\right) \tag{6.24}$$

$$-\overline{u'v'}\frac{\partial U}{\partial y} - \overline{u'w'}\frac{\partial U}{\partial z} - \overline{v'^2}\frac{\partial V}{\partial y} - \overline{v'w'}\frac{\partial V}{\partial z} \tag{6.25}$$

$$-\frac{g}{\rho_0}\overline{w'\rho'} \tag{6.26}$$

$$-\frac{1}{\rho_0}\frac{\partial}{\partial y}(\overline{v'p'}) - \frac{1}{\rho_0}\frac{\partial}{\partial z}(\overline{w'p'}) \tag{6.27}$$

$$-\frac{\partial}{\partial y}\left(\overline{\frac{1}{2}\left(u'^2+v'^2\right)v'}\right) - \frac{\partial}{\partial z}\left(\overline{\frac{1}{2}\left(u'^2+v'^2\right)w'}\right). \tag{6.28}$$

The term on the left hand side of (6.24) denotes the rate of change of EKE with respect to time. The terms on the right hand side of (6.24) correspond to the advection of EKE by the mean flow. The barotropic eddy energy conversion mechanisms are given by (6.25). The eddy energy conversion between the EPE and EKE fields is given by (6.26) with positive (negative) values acting to increase (decrease) eddy kinetic energy. The meridional and vertical eddy pressure flux divergences are shown on (6.27) which act to redistribute EKE and are zero in the domain average. The divergence of EKE by the perturbation velocity fields is given by (6.28). The eddy potential energy budget is calculated from

$$-\left(\frac{g}{\rho_0 \partial\overline{\rho}/\partial z}\right)\rho' \times (6.21), \tag{6.29}$$

and, upon zonal averaging, yields

$$\frac{\partial}{\partial t}\left(\frac{\overline{b'^2}}{2N_0^2}\right) = -V\frac{\partial}{\partial y}\left(\frac{\overline{b'^2}}{2N_0^2}\right) - W\frac{\partial}{\partial z}\left(\frac{\overline{b'^2}}{2N_0^2}\right) \tag{6.30}$$

$$-\alpha\overline{v'\rho'} \tag{6.31}$$

$$+\frac{g}{\rho_0}\overline{w'\rho'} \tag{6.32}$$

$$-\frac{1}{2}\frac{g}{\rho_0}\frac{1}{\partial\overline{\rho}/\partial z}\left(\overline{v'\frac{\partial}{\partial y}(\rho'^2)} + \overline{w'\frac{\partial}{\partial z}(\rho'^2)}\right). \tag{6.33}$$

The term on the left hand side of (6.30) denotes the rate of change of EPE with respect to time. The terms on the right hand side of (6.30) correspond to the advection of EPE by the mean flow. The baroclinic eddy energy conversion mechanism is given by (6.31) with positive values implying transfer of energy from the mean potential energy field to the EPE field, and vice versa for negative values. The energy conversion between the EKE and EPE fields is given by (6.32). The advection of EPE by the perturbation fields is given by (6.33).

Integration		λ [km]	P [days]	c_r [ms^{-1}]
M-NONLIN	V_E	929.6	37.5	-0.287
	V_N	929.6	37.5	-0.287
	T_N	929.6	50	-0.215
H-NONLIN	V_E	926.5	34.7	-0.310
	V_N	926.5	39	-0.275
	T_N	926.5	39	-0.275

Table 6.1: A summary of wavelengths λ, periods P and phase speeds c_r for the dominant waves that develop in integrations M-NONLIN and H-NONLIN. These waves are evident in signals of the meridional velocity perturbation about the equator (V_E), north of the equator (V_N), and also the temperature perturbation north of the equator in the subsurface (T_N).

6.3 Model Output - Stages of the TIW Life-Cycle

In both M-NONLIN and H-NONLIN integrations, the mean fields are unstable and develop into TIWs. Figure 6.1 shows time-longitude plots of meridional velocity at the near surface about the equator (V_E) and north of the equator (V_N). Westward propagating waves develop from approximately day 200 in integration M-NONLIN and day 260 in integration H-NONLIN. Since integration H-NONLIN aborted the model run, the data stops at day 313. Signals of TIWs are also present in sea surface height north of the equator corresponding to the center of the TIVs (not shown) and in temperature at depths below 100m (T_N). Using a power spectral density analysis, we are able to extract the properties of the dominant signals associated with TIWs. The stability characteristics of the unstable waves are summarised in table 6.1. The wavelengths of the waves are similar between integrations M-NONLIN and H-NONLIN, and TIWs are slower for integration M-NONLIN with the signal in T_N having a period of 50 days. The signal in V_N is associated with the anti-cyclonic vortices evident from thin strips of positive (poleward) meridional velocity on the outward edge of the TIVs followed by negative (equatorward) meridional velocities on the right hand of the TIVs. Considering the patterns in meridional velocity north of the equator, TIW activity has significantly diminished after day 300. However, the alternating patterns of meridional velocity at the equator are persistent even up to the end of the model run.

To draw comparison to the outputs of the linear model, and to investigate the properties of TIWs during the equilibrated and decaying stages of their development, we calculate time series of domain averaged eddy kinetic and eddy potential energy shown in figure 6.2. This allows us to determine the approximate time periods during which each stage of the TIW life-cycle occurs. Since integration H-NONLIN aborted its model run early, we are only able to consider the linear stage of the TIW life-cycle in this case.

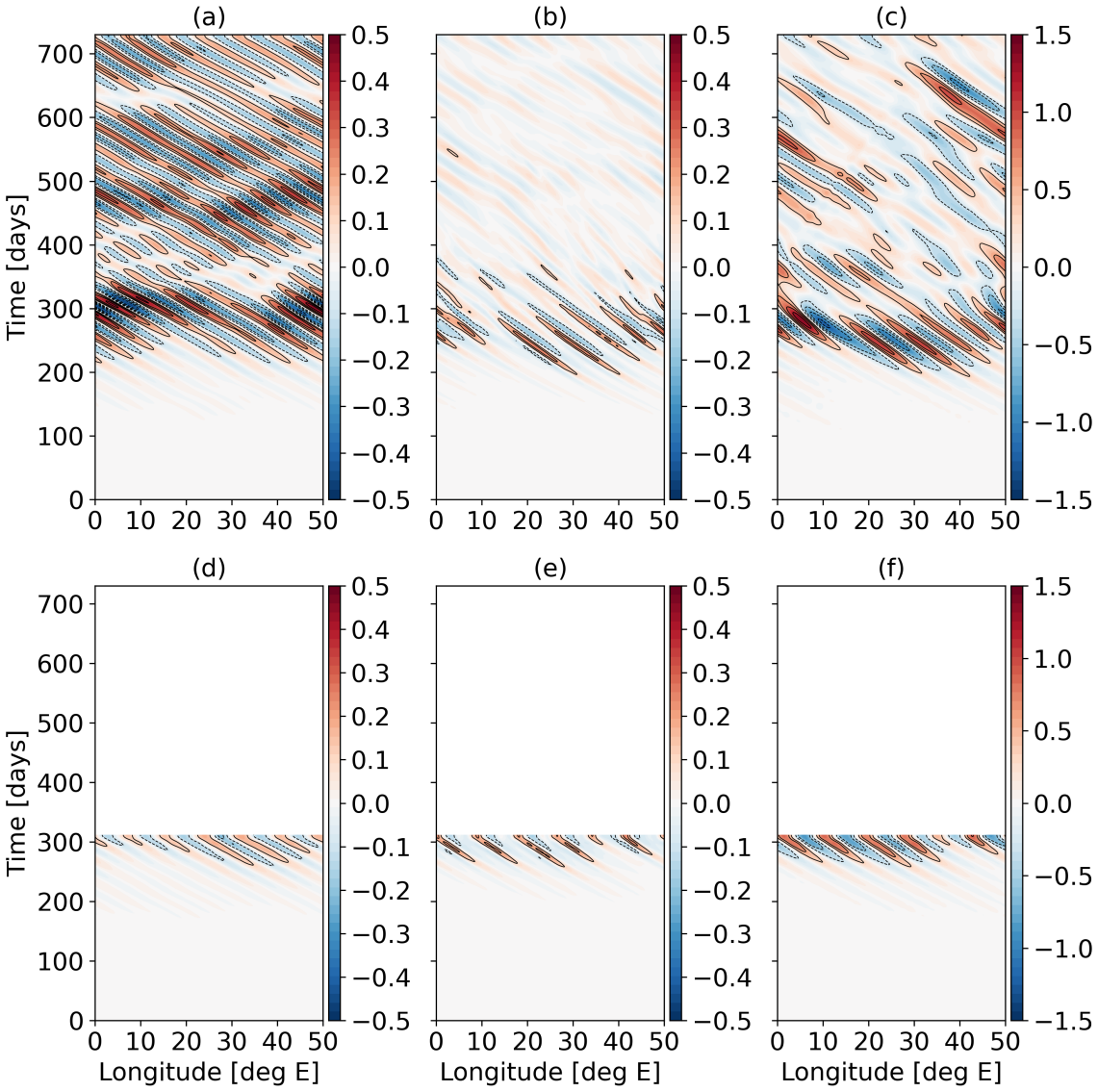


Figure 6.1: Time-longitude plots of perturbation fields from integrations M-NONLIN ((a)-(c)) and H-NONLIN ((d)-(f)). Plots (a) and (d) show the meridional velocity perturbation [ms^{-1}] (filled colour and solid contours) at a depth of 5m and averaged meridionally between $[-0.5°\mathrm{N}, 0, 5°\mathrm{N}]$. Plots (b) and (e) show the meridional velocity perturbation [ms^{-1}] at a depth of 5m and averaged meridionally between $[3°\mathrm{N}, 4°\mathrm{N}]$. Plots (c) and (f) show the temperature perturbation [°C] at a depth of 125m and averaged meridionally between $[3°\mathrm{N}, 6°\mathrm{N}]$. From plots (d)-(f), it is evident that integration H-NONLIN aborted the run at day 313.

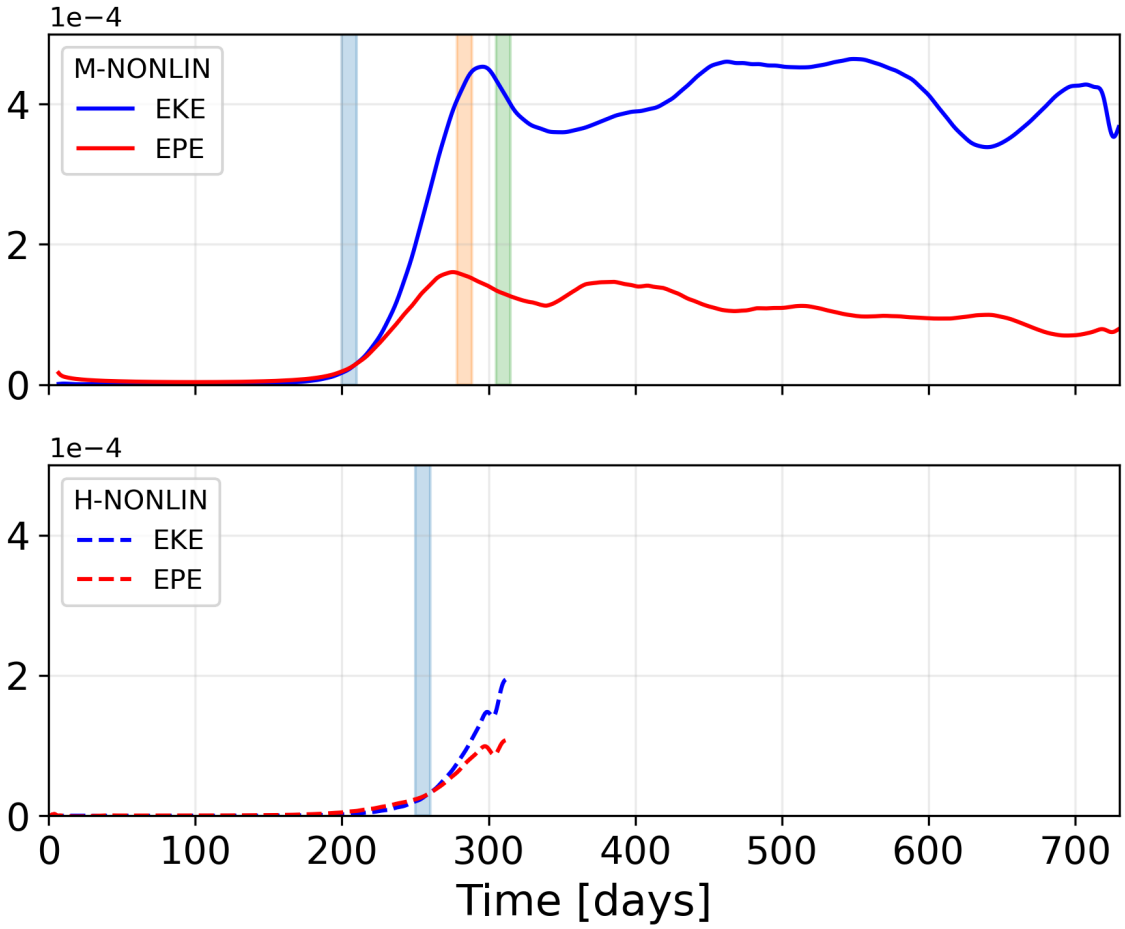


Figure 6.2: Time series of domain averaged eddy kinetic energy (EKE) and eddy potential energy (EPE) for integrations M-NONLIN (top) and H-NONLIN (bottom). Units are m^2s^{-2}. Highlighted vertical strips of blue, orange and green are used to denote periods of TIW development corresponding to the linear, equilibrated and decaying stages of the TIW life-cycle. Due to integration H-NONLIN failing to complete its integration, we are only able to consider data for the linear stage ($250-260$ days). For integration M-NONLIN, the linear stage is the time range of 200 to 210 days, equilibrated stage is 278 to 288 days, and the decaying stage is 305 to 315 days.

To investigate which eddy energy conversion mechanisms are important for the development of TIWs, we plot a time series of the domain average of each eddy conversion mechanism in figure 6.3. Baroclinic conversions dominate the early linear stage of TIW growth which is in agreement with the findings of the idealised linear model in chapter 5. However, barotropic conversion ($-\overline{u'v'}U_y$) becomes the dominant eddy conversion mechanism as the eddies tend to equilibration. During the equilibrated stage, barotropic conversion associated with the mean meridional velocity field becomes non-negligible but remains small throughout the remainder of model run. The domain averaged eddy energy conversions are summarised in table 6.2 along with those from the idealised linear model.

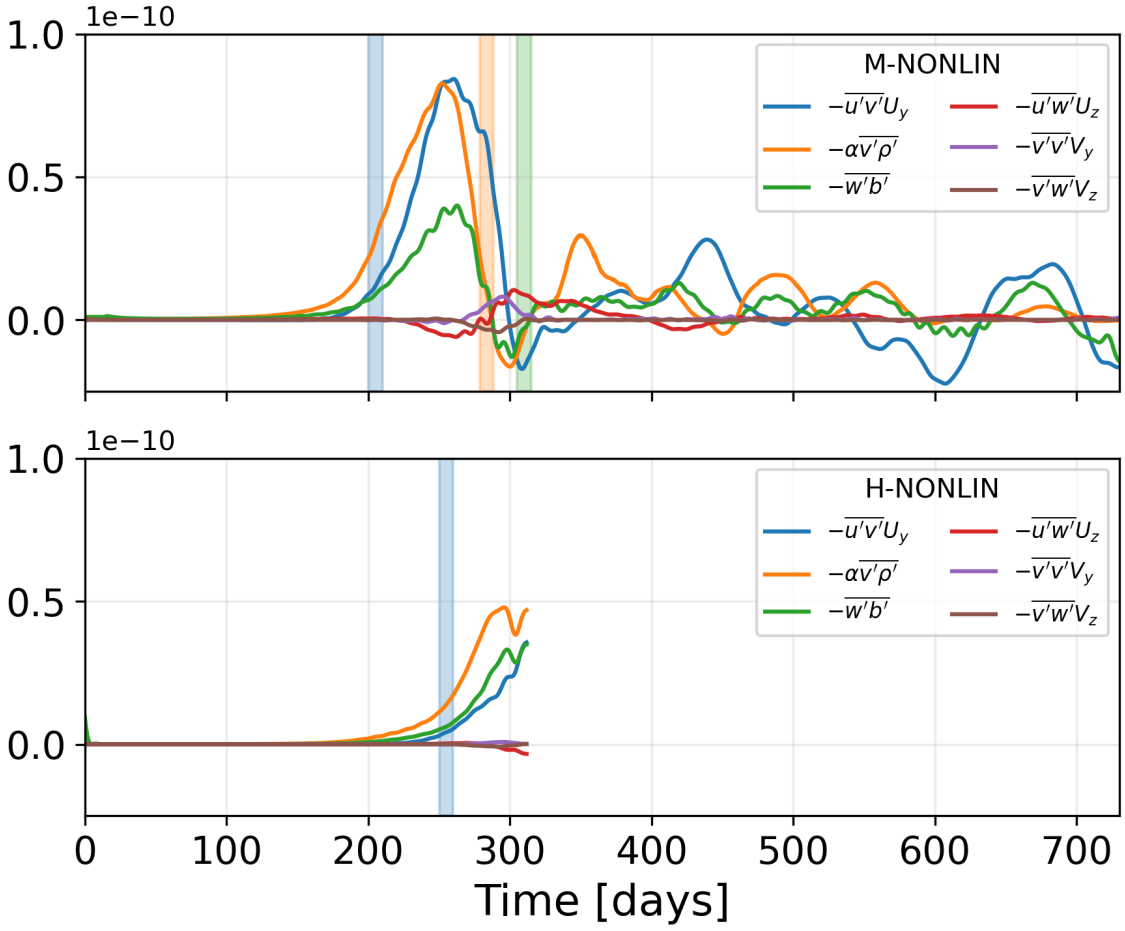


Figure 6.3: Time series of the domain average eddy energy conversion mechanisms at each timestep for integrations M-NONLIN (top) and H-NONLIN (bottom). Units are m^2s^{-3}. The coloured highlighted regions are as in figure 6.2 and denote the linear (blue), equilibrated (orange) and decaying (green) stages of the TIW life-cycle.

Integration	Stage	$-\overline{u'v'}U_y$	$-\alpha\overline{v'\rho'}$	$-\overline{u'w'}U_z$	$-\overline{v'^2}V_y$	$-\overline{v'w'}V_y$
M-LIN	Linear	10.5%	90.1%	-0.6%	-	-
H-LIN	Linear	9.1%	90.2%	0.7%	-	-
M-NONLIN	Linear	29.7%	69.5%	0.8%	0.0%	0.0%
H-NONLIN	Linear	25.3%	74.2%	0.5%	0.0%	0.0%
M-NONLIN	Equilibrated	83.8%	13.8%	0.0%	7.0%	-4.6%

Table 6.2: Percentage contribution of the domain averaged eddy energy conversions to the rate of change of the total eddy energy time averaged over the linear and equilibrated stages of the TIW life-cycle for both the linear (M-LIN and H-LIN) and nonlinear (M-NONLIN and H-NONLIN) integrations. Dashes are used for integrations M-LIN and H-LIN where the eddy energy conversion mechanisms are not included in the eddy energy budgets of the linear model.

6.3.1 Linear Stage

A visualisation of the three-dimensional output of integrations M-NONLIN and H-NONLIN during the linear stage of the TIW life-cycle are shown in figure 6.4. The main features of the instabilities that develop in integrations M-NONLIN and H-NONLIN are similar. The vortices which develop at the equator yield the alternating patters of meridional velocity typical of TIWs. Further north, westward propagating vortices develop with meridional velocity and density perturbation patterns indicative of a northward transport of cold water on the leading edge of a TIV and equatorward transport of warm water on the trailing edge. The vortices north of the equator are readily identifiable from sea surface height perturbations which are maximal (minimal) at the centre of the warm (cold) vortices. The sea surface height perturbations also extend further northwards and lean with the flow. The structure of the vortices that develop near the surface are similar between integrations M-NONLIN and H-NONLIN with the exception of short wavelength sea surface height signals developing south of the equator for integration H-NONLIN.

The depth-longitude and depth-latitude structures of the instability are indicative of a downwards and polewards transport of cold waters on the leading edge of a TIV and upwards and equatorwards transport of warm waters within the core of a TIV. The meridional velocity and density perturbation lean with the westward propagating flow with depth. The vertical extent of these perturbations is weaker for integration H-NONLIN.

Eddy energy conversions associated with the linear stage of the TIW life cycle are shown in figure 6.5. Baroclinic conversion is dominant north of the equator associated with the strong meridional temperature gradient between the cool upwelled waters at the equator

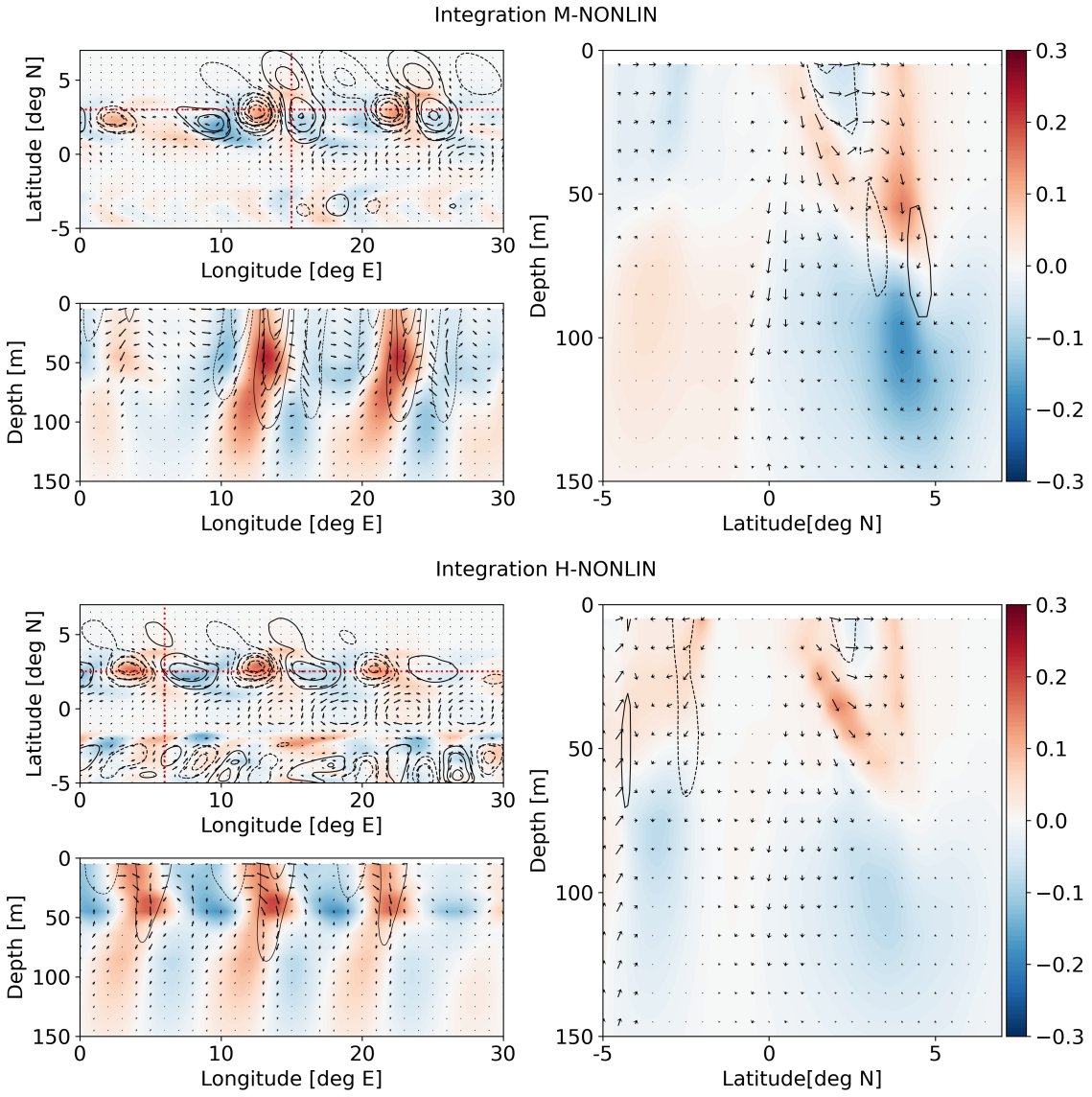


Figure 6.4: Three-dimensional structure of the outputs of the perturbation fields for integration M-NONLIN (top) at day 205 and integration H-NONLIN (bottom) at day 255. The figures for each integration are structured as follows. In the upper left, we plot a latitude-longitude slice of the perturbations of density ρ' [kgm^{-3}] (colour), sea surface height [m] (solid/dashed contours), and horizontal velocity (u', v') [ms^{-1}] (quivers) at a depth of 5m. Red dotted lines are used to denote the locations where we take cross sections for the depth-longitude and depth-latitude plots. In the lower left, we plot a depth-longitude slice, at 3°N for integration M-NONLIN and 2.5°N for integration H-NONLIN, of the perturbations of density (colour), meridional velocity (solid/dashed contours) and (u', w') (quivers). On the right, we plot a depth-latitude slice, at 15°E for integration M-NONLIN and 6°E for integration H-NONLIN, of the perturbations of density (colour), zonal velocity (solid/dashed contours) and (v', w') (quivers).

and the warm off-equatorial water associated with the NECC. There are also significant contributions from barotropic conversion on both flanks of the SECN, as well as eddy potential to eddy kinetic energy conversions. The eddy energy conversions are significant primarily local to the zero in the meridional PV gradient or the critical level. In particular, the baroclinic conversion is maximal close to where these surfaces intersect. In comparison to the linear model, there is a larger contribution from barotropic production. Baroclinic production has greater vertical extent and is maximal near 50m as opposed to 15m in the linear model.

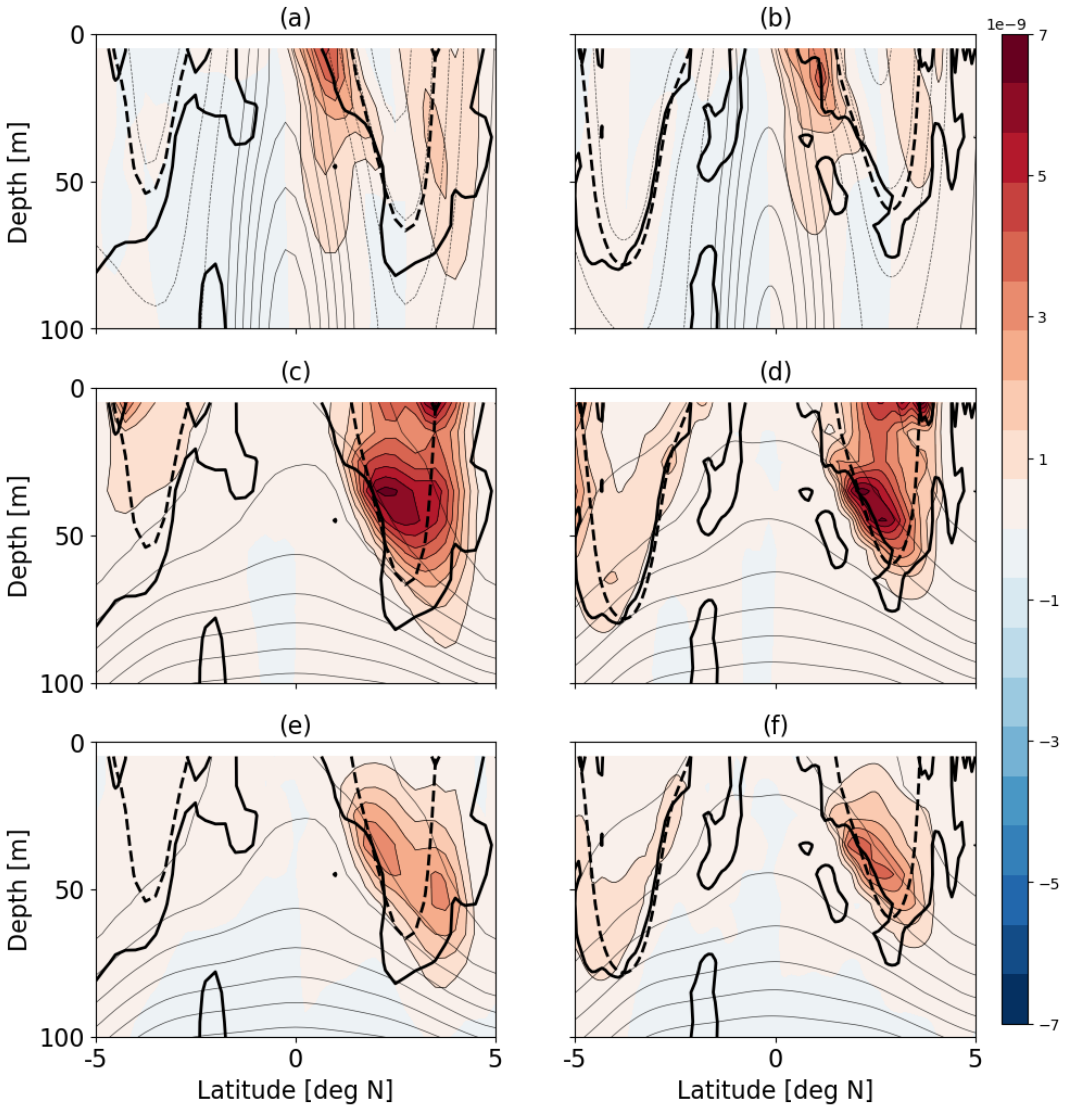


Figure 6.5: As in figure 5.5, but time averaged over the linear stage of the TIW life-cycle for integrations M-NONLIN (left column) and H-NONLIN (right column). Thick solid contours denote the locations where $Q_y = 0$. Thick dashed contours denote the locations $U = c_r$ where $c_r = -0.287\text{ms}^{-1}$ for integration M-NONLIN and $c_r = -0.275\text{ms}^{-1}$ for integration H-NONLIN.

6.3.2 Equilibrated Stage

A visualisation of the three-dimensional output of integration M-NONLIN during the equilibrated stage of the TIW life-cycle is shown in figure 6.6.

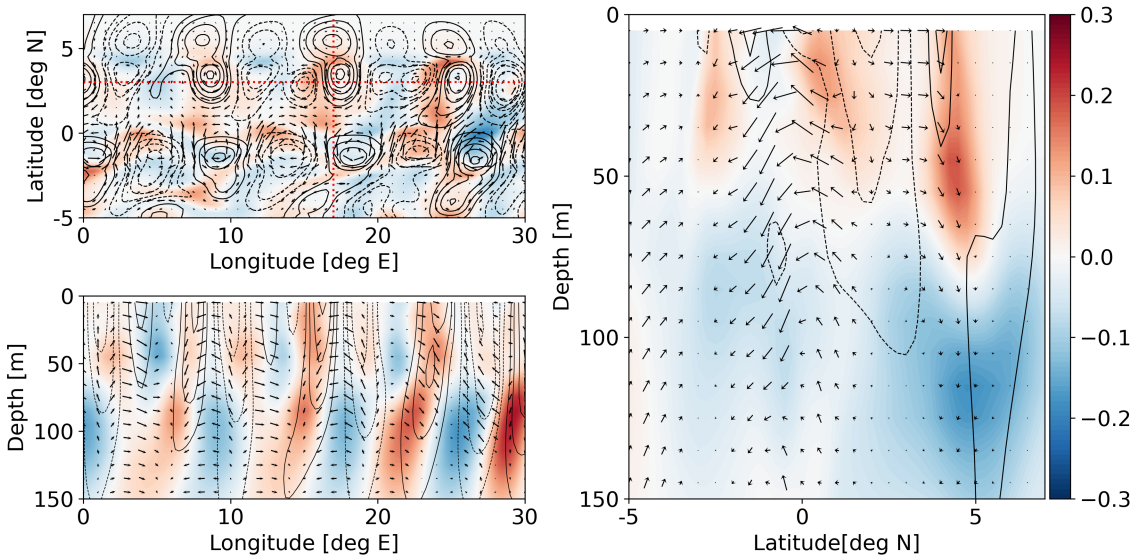


Figure 6.6: As in figure 6.4, but for integration M-NONLIN at day 283 which is the midpoint of the equilibration stage of the TIW life-cycle.

TIWs have fully developed with westward propagating trains of vortices evident on both sides of the equator. Compared to the linear stage, sea surface perturbations are now apparent south of the equator associated with the vortices. The depth-longitude structure of the TIWs at 3°N is similar to that of the linear stage, but has a stronger signal in depth with the density perturbations at a maximum below 50m. The depth-latitude structure in the leading edge of the TIWs has a similar density perturbation structure as the linear stage. However, the spatial structure of the meridional and vertical velocity perturbations differs significantly with strong north-to-south cross-equatorial transports for the equilibrated stage.

The eddy energy conversions for the linear (left column), equilibrated (center column), and decaying (right column) stages of the TIW life-cycle are shown in figure 6.7. Barotropic conversion during the equilibrated stage is the largest source of eddy kinetic energy associated with the meridional shear on the southern flank of the SECN. However, barotropic conversion is also the largest sink in eddy kinetic energy associated with the meridional shear on the southern flank of the EUC. Figure 6.6 indicates that there is significant cross-equatorial transport from the northern to southern flank of the EUC

during the equilibrated stage. The contributions from other eddy energy conversion mechanisms are weak compared to barotropic conversion. The critical level on the southern part of the domain persists throughout the duration of TIW activity, whereas the critical level north of the equator vanishes before equilibration.

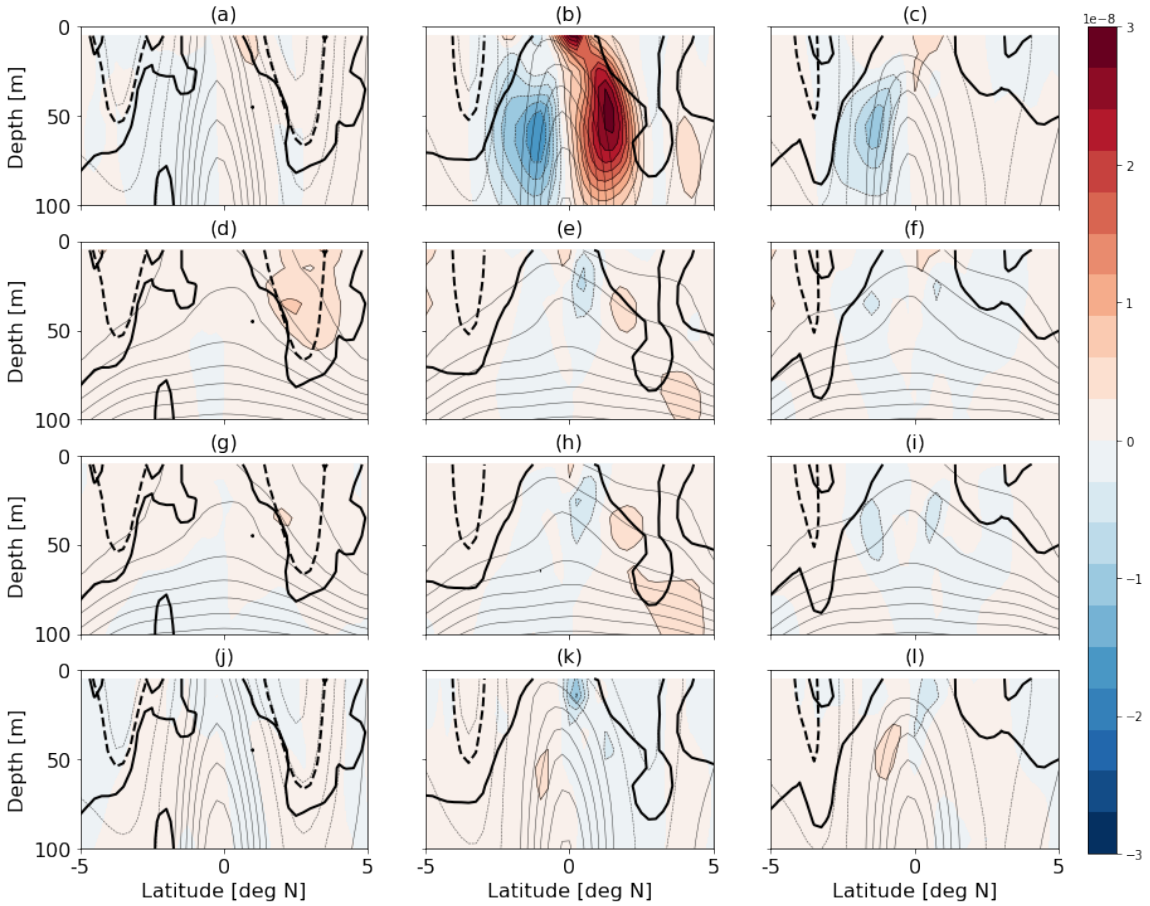


Figure 6.7: Spatial structure of eddy energy conversion mechanisms time averaged over the linear (left column), equilibrated (middle column) and decaying (right column) stages of the TIW life-cycle for integration M-NONLIN. Thick solid contours denote the locations where $Q_y = 0$. Thick dashed contours denote the locations $U = c_r$ where $c_r = -0.287\text{ms}^{-1}$. The barotropic (first row), baroclinic (second row), eddy potential to eddy kinetic (third row) and Kelvin-Helmholtz (fourth row) eddy energy conversion mechanisms are plotted as filled colour contours. Units are m^2s^{-3}. We have superposed the mean zonal velocity [ms^{-1}] (first and fourth rows) and mean density [kgm^{-3}] (second and third rows) onto each plot.

6.3.3 Decaying Stage

A visualisation of the three-dimensional output of integration M-NONLIN during the decaying stage of the TIW life-cycle is shown in figure 6.8. The TIWs north of the equator are weaker than those in the equilibrated stage indicating reduced eddy heat transport

north of the equator. The alternating patterns of meridional velocity at the equator remain strong and are persistent as shown figure 6.1. The fingers of meridional velocity and density perturbations in the depth-longitude plots for the linear and equilibrated stages are weaker in the decaying stage with the perturbations only weakly tilting westwards. The depth-latitude structure exhibits strong perturbation signals near the equator which are associated with the westward propagating vortices located at the equator.

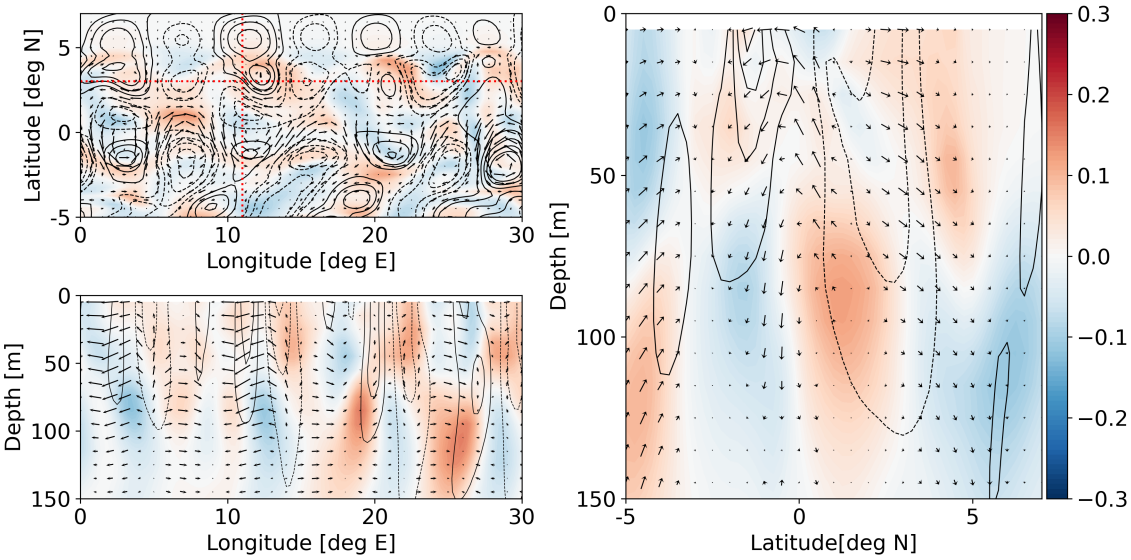


Figure 6.8: As in figure 6.4, but for integration M-NONLIN only, at day 310 which is the midpoint of the decaying stage of the TIW life-cycle.

To gain insight into why TIW activity ceases, we can consider the difference in mean fields prior to TIW activity (day 200) and after TIW activity has ceased (day 315) which is shown in figure 6.9. The difference in the temperature and zonal velocity fields demonstrates that the net impact of TIWs on the mean fields is to heat the surface equatorial waters, cool the northern subsurface waters, and to decrease the strength of the SECN. Figure 6.9 shows that the amplitude of the SECN decreases by approximately 0.3ms^{-1} and is such that the critical level north of the equator, occurring where $U = c_r = -0.287\text{ms}^{-1}$, vanishes. Over the course of TIW activity, both the surface equatorial waters and subsurface northern waters are heated/cooled by 0.5° C, respectively. We can gain greater insight into eddy-mean flow interactions associated with TIWs by examining the eddy stress tensor, whose components consist of eddy Reynolds stresses and eddy form stresses, and its interpretation via eddy ellipse geometry.

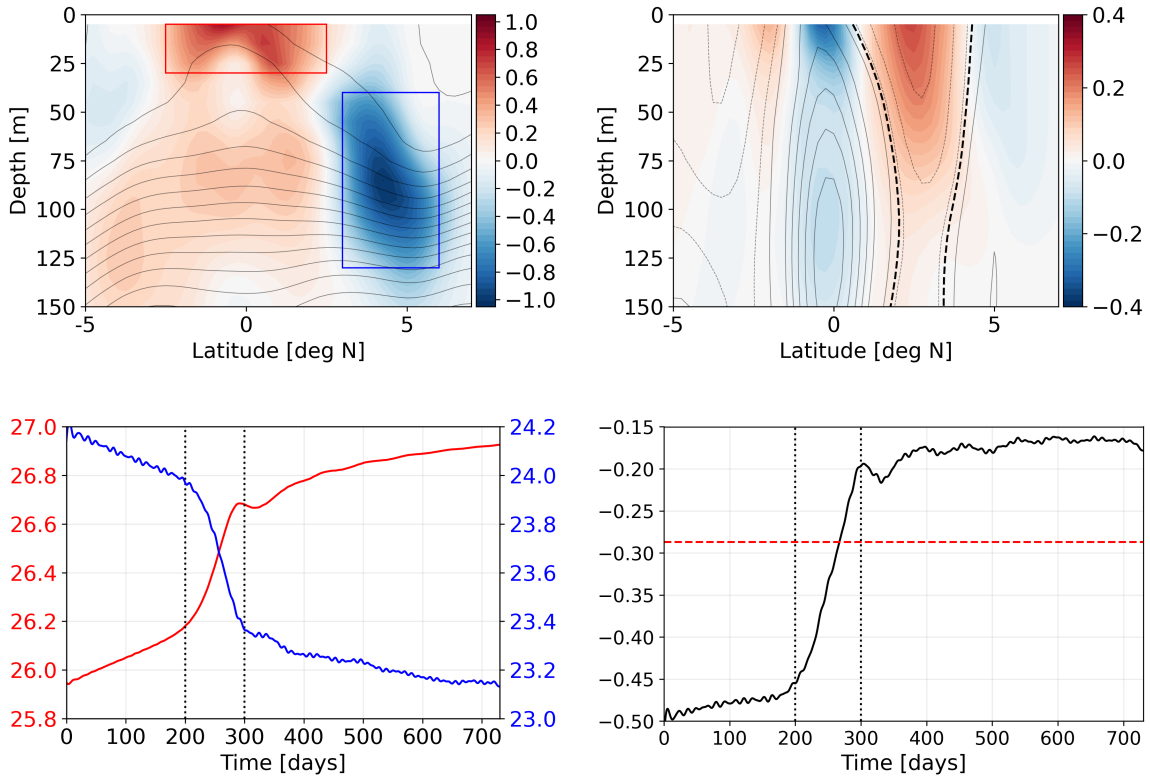


Figure 6.9: (Top left): Difference in the mean temperature field at days 315 and 200 (filled colour contours). Superposed is the mean temperature field at day 250. Red/blue boxes bound the regions where the heating/cooling are strongest. (Top right): Difference in the mean zonal velocity field at days 315 and 200 (filled colour contours). Superposed is the mean zonal velocity field at day 250. Thick dashed contours bound the edges of the westward flowing SECN. (Lower left): Time series of the mean temperature (red/blue line) given by the domain average of the red/blue bounding boxes which are shown in the upper left plot. (Lower right): Time series of the mean zonal velocity within the bounding dashed lines of the SECN. In both cases, dashed lines denote the times between which TIWs are predominantly active, namely days 200 and 300. The red dashed line denotes the phase speed of the unstable wave ($c_r = -0.287\text{ms}^{-1}$).

Chapter 7

Eddy Transports

7.1 Residual-Mean Equations

To investigate eddy-mean flow feedbacks, one can start from the equations of motion written in residual-mean form obtained by using a transformed Eulerian mean (TEM) framework. The advantage of this framework is that it allows the eddy forcing to appear as an effective body force in the mean momentum equations. The disadvantage of the TEM framework is the assumption of quasigeostrophy which is not applicable at the equator. More recently, a thickness-weighted average formulation of the Boussinesq primitive equations written in residual-mean form was derived by Young [2012]. This formulation requires only that the mean density field increases monotonically with height;

$$\frac{\partial u}{\partial t} + u\frac{\partial u}{\partial x} + v\frac{\partial u}{\partial y} + w\frac{\partial u}{\partial z} - fv + \frac{1}{\rho_0}\frac{\partial p}{\partial x} = -\nabla \cdot \boldsymbol{E}^u, \tag{7.1}$$

$$\frac{\partial v}{\partial t} + u\frac{\partial v}{\partial x} + v\frac{\partial v}{\partial y} + w\frac{\partial v}{\partial z} + fu + \frac{1}{\rho_0}\frac{\partial p}{\partial y} = -\nabla \cdot \boldsymbol{E}^v, \tag{7.2}$$

$$\frac{1}{\rho_0}\frac{\partial p}{\partial z} = b, \tag{7.3}$$

$$\frac{\partial b}{\partial t} + u\frac{\partial b}{\partial x} + v\frac{\partial b}{\partial y} + w\frac{\partial b}{\partial z} = 0, \tag{7.4}$$

$$\frac{\partial u}{\partial x} + \frac{\partial v}{\partial y} + \frac{\partial w}{\partial z} = 0, \tag{7.5}$$

where all variables now represent the residual-mean forms as defined in detail in Young [2012]. This form allows one to confine eddy forcing on the mean flow entirely by the horizontal momentum equations and is via the divergence of the Eliassen-Palm [Eliassen, 1961] (EP) vectors $\boldsymbol{E}^u$ and $\boldsymbol{E}^v$ which are three-dimensional generalisations of the zonally averaged EP vectors derived in Andrews and Mcintyre [1976]. The EP vectors are encapsulated by the eddy stress tensor [Plumb, 1986]

$$\boldsymbol{E} = \begin{pmatrix} -M + P & N & 0 \\ N & M + P & 0 \\ -S & R & 0 \end{pmatrix}, \tag{7.6}$$

where

$$M = \frac{1}{2}\left(\overline{v'^2} - \overline{u'^2}\right), \quad N = \overline{u'v'}, \quad P = \frac{\overline{b'^2}}{2N_0^2}, \quad R = \frac{f_0}{N_0^2}\overline{u'b'}, \quad S = \frac{f_0}{N_0^2}\overline{v'b'}. \tag{7.7}$$

Here, M and N represent the eddy Reynolds stresses associated with horizontal fluxes of horizontal momentum. Recall that the eddy potential energy, P, is defined as in the eddy energy budget in equation (4.25). The eddy form stresses, R and S, are proportional to the components of the eddy buoyancy flux. Note that in the literature, M is sometimes defined as $(\overline{u'^2} - \overline{v'^2})/2$ [Hoskins et al., 1983, Waterman and Hoskins, 2013, Waterman and Lilly, 2015].

Despite the formal breakdown of the quasi-geostrophic approximation close to the equator, nevertheless we will follow the quasi-geostrophic framework here, firstly because oceanic motions remain close to geostrophic balance to leading order within a degree or two of the equator, and secondly because the quasi-geostrophic framework is mathematically much simpler. The reader is referred to Young [2012] to see how the results may be generalised beyond the quasi-geostrophic approximation.

7.2 Eddy forcing on the mean flow

The mean momentum equations can be written as

$$\frac{\partial \boldsymbol{u}}{\partial t} + \boldsymbol{u}\cdot\nabla\boldsymbol{u} + f\hat{\boldsymbol{k}}\times\boldsymbol{u} = -\frac{1}{\rho_0}\nabla\left(p + \rho_0 P\right) - \nabla\cdot\boldsymbol{F}, \tag{7.8}$$

where ∇ is the horizontal gradient operator, $\hat{\boldsymbol{k}}$ is the unit vertical vector, $\boldsymbol{u}$ is the horizontal velocity field and

$$\boldsymbol{F} = \begin{pmatrix} -M & N & 0 \\ N & M & 0 \\ -S & R & 0 \end{pmatrix}, \tag{7.9}$$

describes the forcing on the mean field by the eddies. We have separated the eddy potential energy from (7.6) which allows the right hand side of (7.8) to be written as the sum of irrotational and rotational components. Eddy forcing affects the mean flow through the vorticity equation obtained by taking the curl of (7.8). The curl of the gradient of a scalar field is the zero vector, therefore the irrotational force due to the mean pressure field and eddy potential energy do not contribute to the dynamics. The local mean momentum forcing by the eddies is given by

$$-\nabla\cdot\boldsymbol{F} = \frac{\partial M}{\partial x} - \frac{\partial N}{\partial y} + \frac{\partial S}{\partial z}. \tag{7.10}$$

If we consider a zonally periodic system, and apply zonal averaging, then the local mean momentum forcing by the eddies corresponds to a local mean acceleration and is given by

$$-\nabla \cdot \boldsymbol{F} = -\frac{\partial N}{\partial y} + \frac{\partial S}{\partial z}. \tag{7.11}$$

In the case of a purely barotropic instability, eddy forcing of the mean flow is due to the eddy Reynolds stresses only. Observing patterns in N_y leads to understanding how eddies feedback to the mean flow. Eddy momentum fluxes associated with a "banana-shaped" eddy, as shown in patterns of N in figure 7.1, indicate that the effect of eddies is transport eastward momentum into the center of the jet.

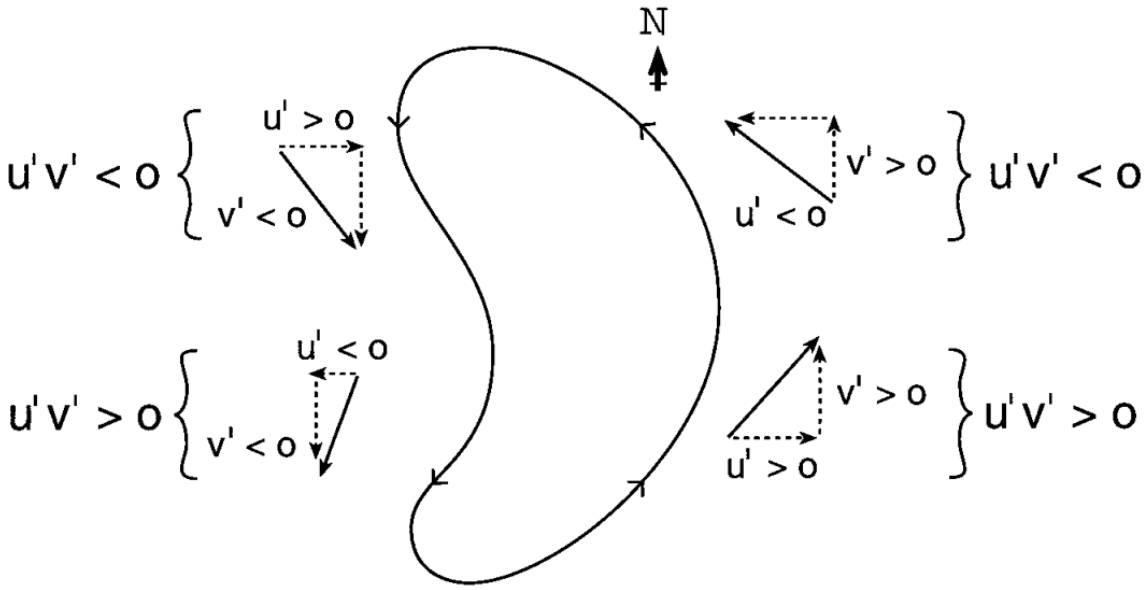


Figure 7.1: Eddy momentum fluxes associated with a "banana-shaped" eddy. Momentum converges at the centre of the eddy and yields an eastward momentum flux. The zonal average of the eddy velocities is zero, but their product can be non-zero if the eddy is anisotropic. The zonal average of $u'v'$ gives $N > 0$ and $N < 0$ on the southern and northern flanks of the eddy, respectively. Figure originally from Wardle and Marshall [2000].

In the case of a purely baroclinic instability, eddy forcing of the mean flow is due to eddy form stresses only. Under the quasigeostrophic approximation, horizontal eddy buoyancy fluxes, that develop from a baroclinically unstable mean flow, are dynamically equivalent to interfacial eddy form stresses associated with a vertical flux of momentum [Munk and Palmen, 1951, Johnson and Bryden, 1989]. A equatorward transport of heat by eddies, for which $S > 0$, results in an upward vertical transport of eastward momentum from the source region. This arises due to zonal pressure gradients correlated with undulations in isopycnals, leading to both: (i) opposing meridional transports of buoyant and dense fluid

through geostrophy; and (ii) a vertical transfer of zonal momentum from the dense fluid below to the buoyant fluid above.

7.3 GEOMETRIC framework

The GEOMETRIC framework allows one to interpret eddy feedbacks onto the mean flow in terms of non-dimensional bounded parameters related to the geometry of eddy fluxes as the principal axes of an ellipse. To achieve this, we will make use of quadratic forms, $\boldsymbol{x}^T \boldsymbol{A} \boldsymbol{x} = 1$, where $\boldsymbol{A}$ is a symmetric rank-two tensor, $\boldsymbol{x} = (x, y, z)$, and the superscript T denotes the transpose of the matrix. Quadratic forms are representations of conic sections whose eigenvectors are the orthogonal principal axes with corresponding eigenvalues equal to the square radii along the principal axes.

The following discussion of the eddy stress tensor and the geometric decomposition of the components of $\boldsymbol{E}$ largely follows that of Poulsen et al. [2019]. Due to two applications of the divergence operator on $\boldsymbol{E}$ for the eddy forcing on the potential vorticity equation, there is a gauge freedom in the specification of $\boldsymbol{E}$. There are several choices for $\boldsymbol{E}$ [Maddison and Marshall, 2013], and we will consider

$$\boldsymbol{E} = \begin{pmatrix} -M + 2K & N & 0 \\ N & M + 2K & 0 \\ -S & R & 0 \end{pmatrix}. \tag{7.12}$$

This choice allows us to decompose $\boldsymbol{E}$ into parts that allows us to investigate the eddy Reynolds stress and eddy form stress components, separately. The eddy stress tensor can be decomposed as

$$\boldsymbol{E} = \boldsymbol{E}_m + \boldsymbol{E}_b, \tag{7.13}$$

where

$$\boldsymbol{E}_m = \begin{pmatrix} -M + K & N & 0 \\ N & M + K & 0 \\ 0 & 0 & -P^* \end{pmatrix}, \qquad \boldsymbol{E}_b = \begin{pmatrix} K & 0 & 0 \\ 0 & K & 0 \\ -S & R & P^* \end{pmatrix}, \tag{7.14}$$

which we term the eddy Reynolds stress tensor and eddy form stress tensor, respectively. We consider a scaled eddy potential energy

$$P^* = \frac{f_0^2}{N_0^2} P, \tag{7.15}$$

where $P = \overline{b'^2}/2N_0^2$. This scaling is taken primarily to allow us to simplify the mathematics by removing coefficients of N_0/f_0 that would appear as the weighting of

vertical components which is common in quasi-geostrophic theory. In the absence of this scaling, one could derive the appropriate eddy stress tensor and its decomposition as shown in Poulsen et al. [2019, Section 2d] and Marshall et al. [2012]. The tensor $\boldsymbol{E}_b$ is not symmetric. However, one can separate $\boldsymbol{E}_b$ into symmetric and antisymmetric parts as follows:

$$\boldsymbol{E}_b = \underbrace{\frac{1}{2}\left(\boldsymbol{E}_b + \boldsymbol{E}_b^T\right)}_{\text{symmetric}} + \underbrace{\frac{1}{2}\left(\boldsymbol{E}_b - \boldsymbol{E}_b^T\right)}_{\text{antisymmetric}}. \tag{7.16}$$

Since $\boldsymbol{x}^T\boldsymbol{B}\boldsymbol{x} = 0$ for any antisymmetric tensor $\boldsymbol{B}$, the geometry described by any $\boldsymbol{B}$ is associated with its symmetric part. The symmetric contribution to the eddy form stress tensor $\boldsymbol{E}_b$ is

$$\frac{1}{2}\left(\boldsymbol{E}_b + \boldsymbol{E}_b^T\right) = \begin{pmatrix} K & 0 & -S/2 \\ 0 & K & R/2 \\ -S/2 & R/2 & P^* \end{pmatrix}. \tag{7.17}$$

Since we are only interested in the geometry described by the symmetric part of the eddy from stress tensor, from this points onwards we denote (7.17) as the eddy form stress tensor $\boldsymbol{E}_b$.

7.3.1 Eddy Reynolds stress decomposition

The eddy Reynolds stress tensor $\boldsymbol{E}_m$ has eigenvalues $-P$ and

$$\lambda_\pm = K(1 \pm \gamma_m), \tag{7.18}$$

where

$$\gamma_m = \sqrt{\frac{M^2 + N^2}{K^2}}, \tag{7.19}$$

is the eddy momentum flux anisotropy. The details of the calculation of the eigenvalues is given in section A.1 of the appendix. This quantity is denoted as L/K in Waterman and Lilly [2015] and $\hat{M}$ in Hoskins et al. [1983]. As in Marshall et al. [2012], one can derive the energetic bound

$$\begin{aligned} M^2 + N^2 &= \frac{1}{4}\left(\left(\overline{v'^2}\right)^2 - 2\overline{u'^2v'^2} + \left(\overline{u'^2}\right)^2\right) + \left(\overline{u'v'}\right)^2, && (7.20)\\ &= \frac{1}{4}\left(\left(\overline{v'^2}\right)^2 - 2\overline{u'^2v'^2} + 4\left(\overline{u'v'}\right)^2 + \left(\overline{u'^2}\right)^2\right), && (7.21)\\ &\leq \frac{1}{4}\left(\left(\overline{v'^2}\right)^2 + 2\overline{u'^2v'^2} + \left(\overline{u'^2}\right)^2\right), && (7.22)\\ &= K^2, && (7.23) \end{aligned}$$

where we have used the Cauchy-Schwartz inequality in (7.22). The energetic bound on the eddy Reynolds stresses implies that the eddy momentum flux anisotropy is bounded between zero and unity such that $0 \leq \gamma_m \leq 1$. The eddy Reynolds stress tensor has two positive eigenvalues and one negative eigenvalue. Therefore, the quadratic form $\boldsymbol{x}^T \boldsymbol{E}_m \boldsymbol{x} = 1$ geometrically describes a hyperboloid of one sheet. The only off-diagonal elements of $\boldsymbol{E}_m$ are the horizontal velocity covariances $N = \overline{u'v'}$ and this suggests that a horizontal cross section of the hyperboloid, which describes an ellipse in (u', v')-space, provides a more concise representation of the relevant eddy Reynolds stress geometry. Let

$$\boldsymbol{T}_h = \begin{pmatrix} 1 & 0 & 0 \\ 0 & 1 & 0 \end{pmatrix}, \tag{7.24}$$

be the transformation matrix that consists of the two basis vectors in $\mathbb{R}^3$ that span the horizontal plane. A linear transformation of $\boldsymbol{E}_m$ using $\boldsymbol{T}_h$ gives

$$\boldsymbol{E}_m^\dagger = \boldsymbol{T}_h \boldsymbol{E}_m \boldsymbol{T}_h^T = \begin{pmatrix} -M + K & N \\ N & M + K \end{pmatrix}, \tag{7.25}$$

which is the tensor studied by Waterman and Lilly [2015] for barotropic systems. The geometric and dynamic properties of the eddy ellipse are described in Waterman and Lilly [2015, Section 2] of which we now provide a summary.

The eddy Reynolds stress tensor $\boldsymbol{E}_m^\dagger$ can be separated into isotropic and anisotropic parts as

$$\boldsymbol{E}_m^\dagger = K\boldsymbol{I} + \begin{pmatrix} -M & N \\ N & M \end{pmatrix}, \tag{7.26}$$

where $\boldsymbol{I}$ is the 2×2 identity matrix. Separating into isotropic and anisotropic parts allows one to determine which elements describe tendency for variability to align along a preferred axis. In this case, we see that the eddy kinetic energy has no effect on the anisotropy of the eddy ellipse and that it is solely the eddy Reynolds stresses which contribute. The eddy Reynolds stress tensor $\boldsymbol{E}_m^\dagger$ is equivalent to the horizontal velocity covariance matrix

$$\boldsymbol{E}_m^\dagger = \begin{pmatrix} -M + K & N \\ N & M + K \end{pmatrix} = \begin{pmatrix} \overline{u'^2} & \overline{u'v'} \\ \overline{u'v'} & \overline{v'^2} \end{pmatrix}. \tag{7.27}$$

Visualisation of covariance matrices as ellipses is well-studied [Preisendorfer and Mobley, 1988] and provides a convenient framework to obtain a visual representation of eddy momentum fluxes. The horizontal velocity covariance matrix $\boldsymbol{E}_m^\dagger$ is real and symmetric, therefore $\boldsymbol{E}_m^\dagger$ has an eigenvalue decomposition given by

$$\boldsymbol{E}_m^\dagger = \boldsymbol{Q}\boldsymbol{\Lambda}\boldsymbol{Q}^T \tag{7.28}$$

$$= \begin{pmatrix} \cos\phi_m & -\sin\phi_m \\ \sin\phi_m & \cos\phi_m \end{pmatrix} \begin{pmatrix} \lambda_+ & 0 \\ 0 & \lambda_- \end{pmatrix} \begin{pmatrix} \cos\phi_m & -\sin\phi_m \\ \sin\phi_m & \cos\phi_m \end{pmatrix}^T, \tag{7.29}$$

where $\boldsymbol{Q}$ is an orthogonal square matrix whose columns are the real, orthonormal eigenvectors of $\boldsymbol{E}_m^\dagger$, and $\boldsymbol{\Lambda}$ is the diagonal matrix whose elements are the corresponding eigenvalues λ_+ and λ_- from (7.18). One can summarise $\boldsymbol{E}_m^\dagger$ as a linear transformation $\boldsymbol{x} \mapsto \boldsymbol{E}_m^\dagger \boldsymbol{x}$ of the space $\mathbb{R}^2$ with $\boldsymbol{x} = (x, y)$ whereby the matrix $\boldsymbol{Q}$ represents a rotation anti-clockwise through an angle ϕ_m with respect to the positive x-axis, and the matrix $\boldsymbol{\Lambda}$ represents a scaling of each coordinate (x, y) by the factors (λ_+, λ_-). By considering the quadratic form $\boldsymbol{x}^T \boldsymbol{E}_m^\dagger \boldsymbol{x}$, and also that the eigenvalues of $\boldsymbol{E}_m^\dagger$ are non-negative, one can show that $\boldsymbol{E}_m^\dagger$ describes an ellipse whose eigenvectors, given by the ith column of $\boldsymbol{Q}$, lie along the principal axes, and whose corresponding eigenvalues are equal to the squared radii along the principal axes.

Expanding out (7.29), one can rewrite $\boldsymbol{E}_m^\dagger$ as the sum of isotropic and anisotropic parts

$$\boldsymbol{E}_m^\dagger = K\boldsymbol{I} + \gamma_m K \begin{pmatrix} \cos 2\phi_m & \sin 2\phi_m \\ \sin 2\phi_m & -\cos 2\phi_m \end{pmatrix}, \tag{7.30}$$

where $\boldsymbol{I}$ is the identity matrix. Note that $\gamma_m K = \sqrt{M^2 + N^2}$ and therefore the eddy kinetic energy makes no contribution to the anisotropic part of the ellipse. A value of $\gamma_m = 0$ implies that eddies are on average locally isotropic, whereas a value of γ_m close to 1 implies that eddies are on average locally extended along the major axis and compressed along the minor axis. Comparing the components of (7.30) to the horizontal velocity covariance tensor, one can show that the ellipse is tilted at an angle

$$\phi_m = \frac{1}{2} \tan^{-1}\left(-\frac{N}{M}\right), \tag{7.31}$$

with the positive x-axis, which describes the average local orientation of the eddy variability and hence the local direction of the eddy elongation characterised by γ_m.

Comparing (7.30) with (7.25), one can write the eddy Reynolds stresses in terms of the eddy kinetic energy and dimensionless eddy ellipse parameters as

$$M = -\gamma_m K \cos 2\phi_m, \qquad N = \gamma_m K \sin 2\phi_m. \tag{7.32}$$

It is important to note that the geometric eddy ellipse described by the parameters K, γ_m and ϕ_m is not a description of the shape of the eddies themselves, but a local description of their average stresses. Let $E = K + P$ be the total eddy energy and define ξ to be the energy partitioning angle with respect to E,

$$\frac{K}{E} = \cos^2(\lambda), \qquad \frac{P}{E} = \sin^2(\lambda). \tag{7.33}$$

The eddy Reynolds stresses can then be written as

$$M = -\gamma_m E \cos(2\phi_m)\cos^2(\lambda), \qquad N = \gamma_m E \sin(2\phi_m)\cos^2(\lambda). \tag{7.34}$$

7.3.2 Eddy form stress decomposition

The eddy form stress tensor (7.17) has eigenvalues K and

$$\lambda_{\pm} = \frac{L}{2}\left(1 \pm \gamma_t\right), \tag{7.35}$$

where

$$L = K + \frac{f_0^2}{N_0^2}P = K + P^*, \tag{7.36}$$

is the sum of the eddy kinetic energy and scaled eddy potential energy, and

$$\gamma_t = \sqrt{\cos^2(2\lambda^*) + \sin^2(2\lambda^*)\gamma_b^2}, \tag{7.37}$$

with

$$\gamma_b = \frac{N_0}{2|f_0|}\sqrt{\frac{R^2+S^2}{KP}}. \tag{7.38}$$

Similarly to the eddy partitioning angle of the eddy energy E (7.33), the angle λ^* corresponds to the eddy energy partitioning of L between the eddy kinetic energy and scaled eddy potential energy as

$$\frac{P^*}{L} = \sin^2(\lambda^*), \qquad \frac{K}{L} = \cos^2(\lambda^*). \tag{7.39}$$

The details of the calculation of the eigenvalues is given in section A.2 of the appendix. As in Marshall et al. [2012], one can derive the following energetic bound on the eddy form stresses

$$\begin{aligned}
\frac{N_0^2}{2f_0^2}(R^2+S^2) &= \frac{N_0^2}{2f_0^2}\left(\frac{f_0^2}{N_0^2}\left(\overline{u'b'}\right)^2 + \frac{f_0^2}{N_0^2}\left(\overline{v'b'}\right)^2\right), && (7.40)\\
&= \frac{1}{2}\left(\left(\overline{u'b'}\right)^2 + \left(\overline{v'b'}\right)^2\right), && (7.41)\\
&\leq \frac{1}{2}\left(\overline{u'^2b'^2} + \overline{v'^2b'^2}\right), && (7.42)\\
&= \frac{\overline{b'^2}}{2}\left(\overline{u'^2} + \overline{v'^2}\right), && (7.43)\\
&\leq 2\cdot\frac{1}{2}\left(\overline{u'^2} + \overline{v'^2}\right)\cdot\frac{\overline{b'^2}}{2N_0^2}, && (7.44)\\
&= 2KP, && (7.45)\\
&= 2K(E-K), && (7.46)\\
&\leq \frac{E^2}{2}, && (7.47)
\end{aligned}$$

where we have used Cauchy-Schwartz inequality in lines (7.41) to (7.42). The energetic bound (7.40) implies that that the eddy buoyancy flux anisotropy γ_b is bounded between

zero and unity such that $0 \leq \gamma_b \leq 1$. This also implies that $0 \leq \gamma_t \leq 1$. The eddy form stress tensor has three positive eigenvalues and therefore the quadratic form $\boldsymbol{x}^T \boldsymbol{E}_b \boldsymbol{x} = 1$ describes an ellipsoid. The major axis of the ellipsoid, corresponding to the eigenvector of the largest eigenvalue λ_+, is oriented at an angle ϕ_e to the zonal direction and is given by

$$\cos(\phi_e) = \mp \frac{S}{\sqrt{R^2 + S^2}}, \qquad \sin(\phi_e) = \pm \frac{R}{\sqrt{R^2 + S^2}}. \tag{7.48}$$

The horizontal orientation of the eddy buoyancy flux vector is defined by

$$\cos(\phi_b) = \frac{R}{\sqrt{R^2 + S^2}}, \qquad \sin(\phi_b) = \frac{S}{\sqrt{R^2 + S^2}}. \tag{7.49}$$

One can see that the major axis of the ellipse leads/lags the eddy buoyancy flux vector by $\pi/2$ in the horizontal such that

$$\phi_e = \phi_b \pm \pi/2. \tag{7.50}$$

The off-diagonal elements of $\boldsymbol{E}_b$ are terms proportional to the covariances $\overline{u'b'}$ and $\overline{v'b'}$ and this suggests that a vertical section of the ellipsoid, which is described by an ellipse, provides a more concise representation of the relevant eddy form stress geometry. Let

$$\boldsymbol{T}_v = \begin{pmatrix} \cos(\phi_e) & -\sin(\phi_e) & 0 \\ 0 & 0 & 1 \end{pmatrix}, \tag{7.51}$$

be the transformation matrix that consists of two basis vectors in $\mathbb{R}^3$ that span the vertical plane along the major axis of the ellipsoid. A linear transformation of $\boldsymbol{E}_b$ using $\boldsymbol{T}_v$ gives

$$\boldsymbol{E}_b^\dagger = \boldsymbol{T}_v \boldsymbol{E}_b \boldsymbol{T}_v^T = \begin{pmatrix} K & \frac{1}{2}\sqrt{R^2 + S^2} \\ \frac{1}{2}\sqrt{R^2 + S^2} & P^* \end{pmatrix}, \tag{7.52}$$

where we have used (7.48). Similarly to the eddy Reynolds stress tensor, $\boldsymbol{E}_b^\dagger$ describes a vertical ellipse with eccentricity γ_t and horizontal orientation ϕ_e. From equations (7.33), (7.38), and (7.49), one can write the eddy form stresses as

$$R = \gamma_b \frac{f_0}{N_0} L \cos(\phi_b) \sin(2\lambda^*), \qquad S = \gamma_b \frac{f_0}{N_0} L \sin(\phi_b) \sin(2\lambda^*). \tag{7.53}$$

One can equivalently write the eddy form stresses in terms of the vertical orientation of the ellipse, instead of the horizontal orientation as in (7.53). One can show that the vertical tilt of the ellipse is given by

$$\tan(2\phi_t) = \gamma_b \tan(2\lambda^*). \tag{7.54}$$

Rearranging (7.54) for γ_b and then substituting into (7.37) yields an alternate expression for the ellipse eccentricity as

$$\gamma_t = \frac{\cos(2\lambda)}{\cos(2\phi_t)}. \tag{7.55}$$

This allows the eddy form stresses to be written in terms of the vertical orientation of the ellipse

$$R = \gamma_b \frac{f_0}{N_0} L \cos(\phi_b) \sin(2\phi_t), \qquad S = \gamma_b \frac{f_0}{N_0} L \sin(\phi_b) \sin(2\phi_t). \tag{7.56}$$

7.4 Results

7.4.1 Eddy Reynolds Stresses

Linear Model

Depth-latitude plots of the zonal mean eddy momentum flux $N = \overline{u'v'}$ are shown in figure 7.2 for both models M-LIN and H-LIN. In both cases, there is a positive flux of momentum located within the strong shear of the mean zonal velocity associated with the SECN at 1°N. There is a negative flux of momentum near the core of the SECN at 2°N. This converging momentum flux pattern corresponds to the banana-shaped eddies illustrated in figure 7.1. In particular, the eddies act to flux eastward momentum into the center of the converging region at 1.5°N where zonal momentum forcing on the mean flow by the eddies is largest corresponding to a local maximum in $-N_y$. The main difference between the spatial distribution of N for M-LIN and H-LIN is that there is a positive flux of momentum at 3°N for M-LIN. This results in a convergent momentum flux indicative of a flux of westward momentum into the core of the SECN. However, this positive contribution to N is both weak and also not present in the higher resolution output.

The eastward momentum flux by the eddies in figure 7.2 is consistent with scatter plots of $u' - v'$ and their corresponding geometrical eddy ellipse parameters shown in figure 7.3. As one moves north from the equator and plots covariance ellipses corresponding to the meridional locations of the black circles in figure 7.2, the ellipses exhibit positive tilts on the southern flank of the SECN and then become negatively tilted further north. Furthermore, plots of the eddy ellipses superposed onto the mean zonal velocity field, presented in figure 7.4, indicate that the eddies are extracting energy from the mean flow. The eddies are tilted into the mean flow on the southern flank of the SECN where there is strong meridional shear between the EUC and SECN. This is consistent with positive values of barotropic conversion ($-\overline{u'v'}U_y$) and hence eddies extracting energy from the mean flow.

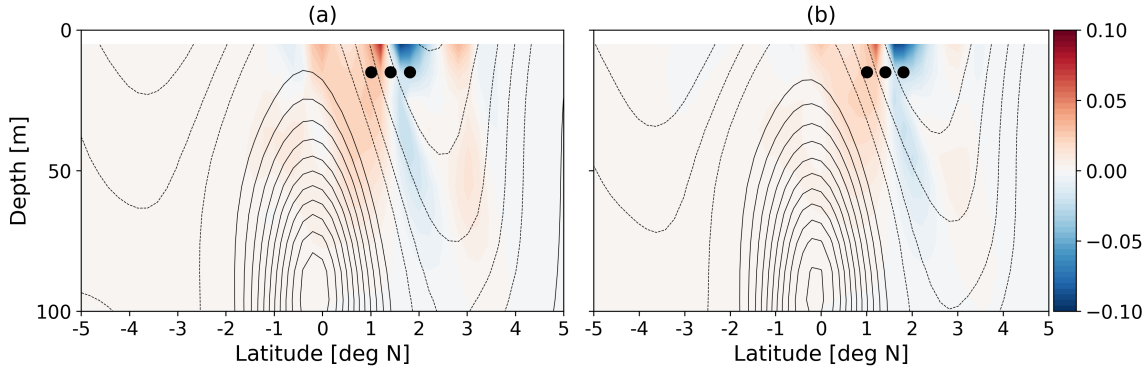


Figure 7.2: Zonally averaged eddy momentum flux $N = \overline{u'v'}$ (colour) calculated from models M-LIN (a) and H-LIN (b). Superposed are contours of the mean zonal velocity field at intervals of 0.1ms^{-1} with positive (negative) values denoted by solid (dashed) contours. In both plots, three black circular markers are used to denote the locations at which we plot $u' - v'$ covariance ellipses in figure 7.3, namely 1°N, 1.4°N and 1.8°N at a depth of 15m.

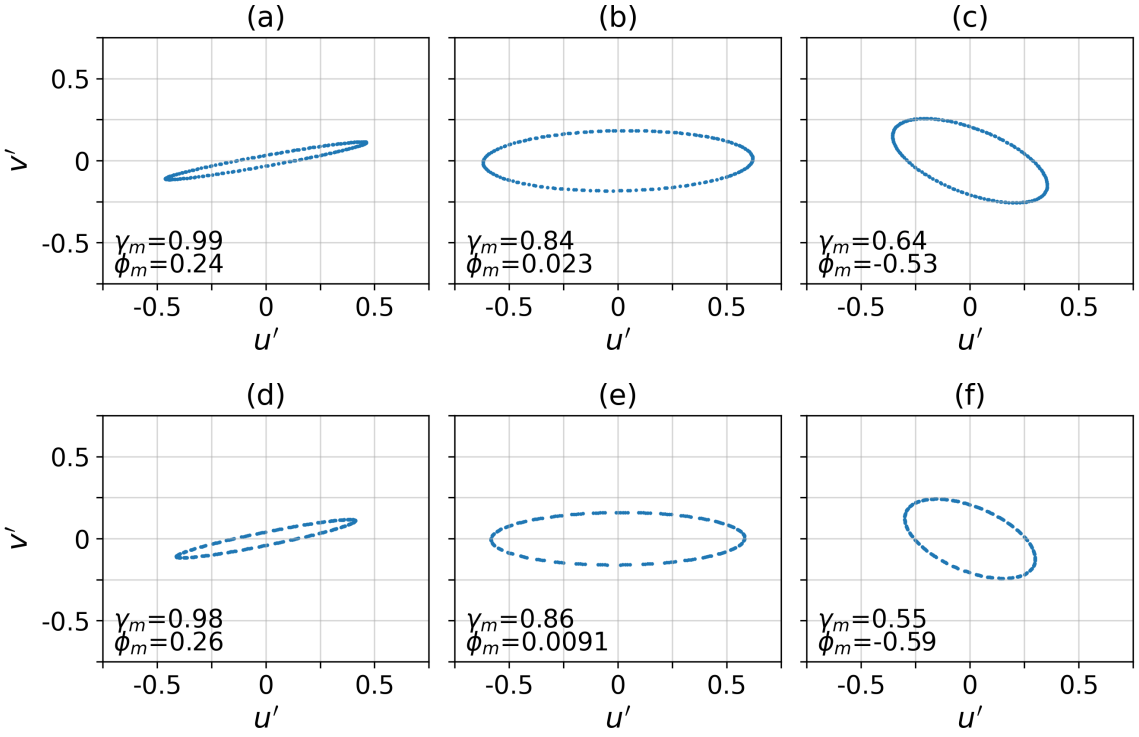


Figure 7.3: Horizontal eddy velocity covariance ellipses from models M-LIN ((a)-(c)) and H-LIN ((d)-(f)). Ellipses are calculated via scatter plots of (u', v') over longitude. Corresponding eddy ellipse eccentricity (γ_m) and tilt (ϕ_m [rads]) values are stated in the lower left of each plot. Eddy ellipses are plotted corresponding to the black circles in figure 7.2, namely 1°N ((a),(d)), 1.4°N ((b),(e)), and 1.8°N ((c),(f)) at a depth of 15m.

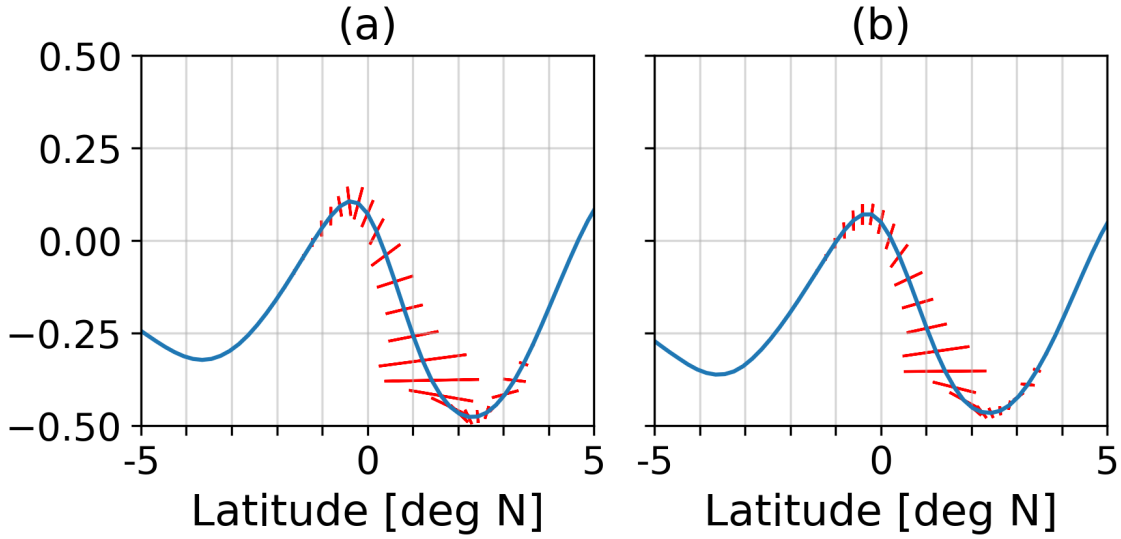


Figure 7.4: Mean zonal velocity at a depth of 15m for models M-LIN (a) and H-LIN (b). At each grid point, eddy ellipses are plotted along the mean zonal velocity field to demonstrate eddies tilting into the shear of the mean flow. The size of the eddy ellipses is proportional to the eddy kinetic energy and, for visual clarity, we have fixed the eddy eccentricity to 1.

Nonlinear Model

Depth-latitude plots of the zonally averaged eddy momentum flux N, which is averaged in time over the linear period of the TIW life-cycle, are presented in figure 7.5. There is a positive flux of momentum at 1°N on the southern flank of the SECN, and there is a negative flux of momentum at 3°N immediately north of the core of the SECN. A converging momentum flux pattern like this indicates that eddies are acting to flux eastward momentum into the core of the SECN. This is consistent with scatterplots of $u' - v'$ and the corresponding geometrical eddy ellipse properties shown in figure 7.6. The distribution of the eddy ellipse tilts exhibits a banana-shaped pattern with positive and negative tilts at 1°N and 3°N, respectively. The eddies are tilted into the mean flow, as shown in figure 7.7. This indicates that eddies are extracting energy from the mean flow with positive values of barotropic conversion ($-\overline{u'v'}U_y$).

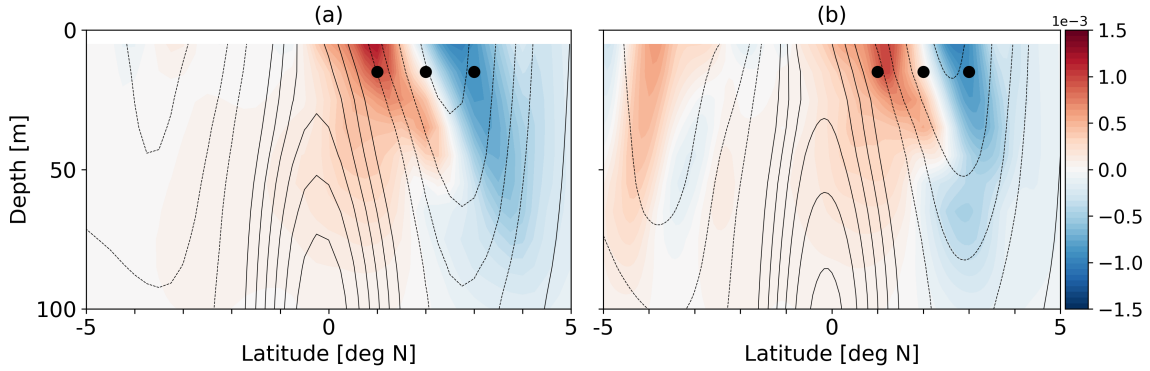


Figure 7.5: Depth-latitude plot of the zonally averaged eddy momentum flux $N = \overline{u'v'}$ (colour) averaged in time over the linear period of the TIW life-cycle for integrations M-NONLIN (a) and H-NONLIN (b). Contours of the mean zonal velocity averaged over the same time period are superposed with contour intervals of 0.1ms^{-1}. Three black circular markers are used to denote the locations at which we plot $u' - v'$ covariance ellipses in figure 7.6, namely at 15m depth and 1°N, 2°N and 3°N, respectively.

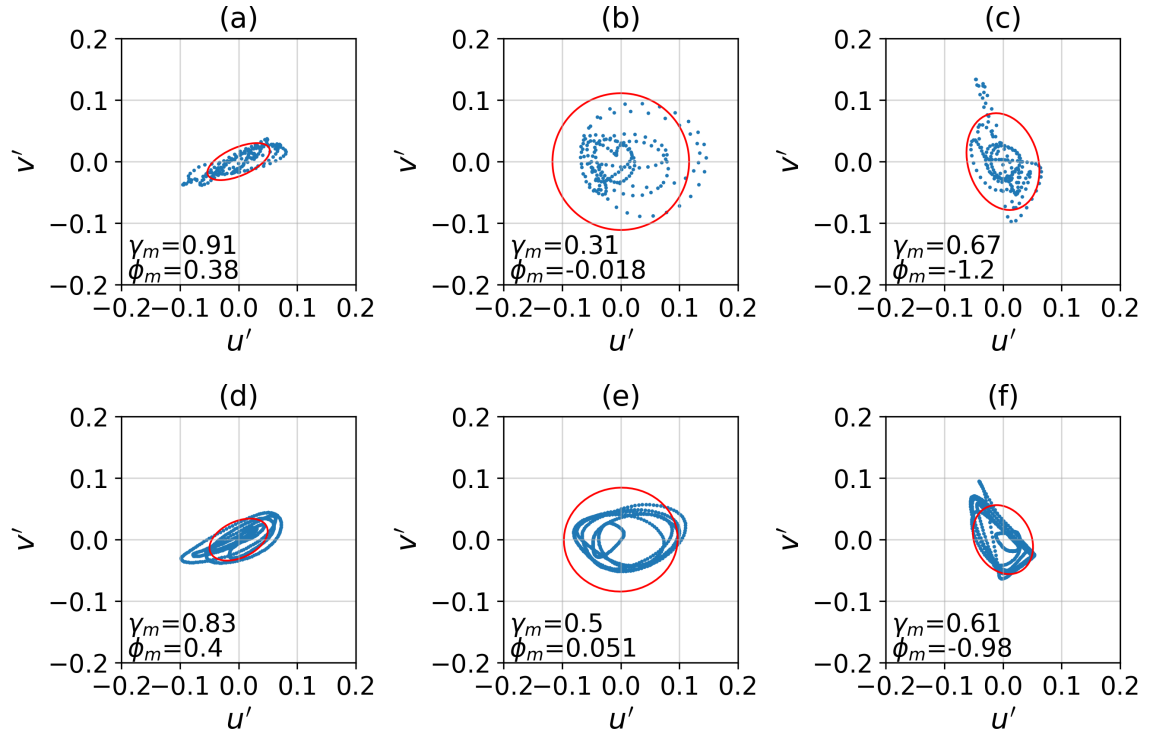


Figure 7.6: Scatter plots of (u', v'), for integrations M-NONLIN ((a)-(c)) and H-NONLIN ((d)-(f)), time averaged over the linear period of the TIW life-cycle, at a depth of 15m, and over different meridional locations, from left to right, at $y = 1°\text{N}$, $y = 2°\text{N}$ and $y = 3°\text{N}$. Superposed are red variance ellipses with eccentricity γ_m, tilt ϕ_m and are scaled with the eddy kinetic energy. Values for the eccentricity and tilts (radians) of each ellipse are stated in the lower left of each plot.

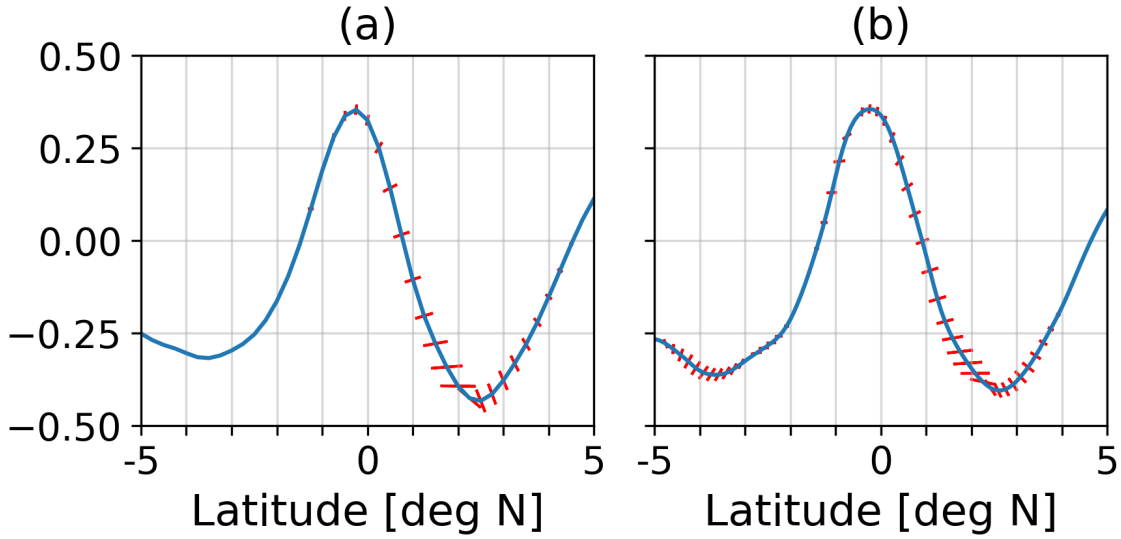


Figure 7.7: Mean zonal velocity (blue) time averaged over the linear period of the TIW life-cycle and at 15m depth for integrations M-NONLIN (a) and H-NONLIN (b). At each grid point, eddy ellipses are plotted along the mean zonal velocity field to demonstrate eddies tilting into the shear of the mean flow. The size of the eddy ellipses is proportional to the eddy kinetic energy and, for visual clarity, we have fixed the eddy eccentricity to 1.

Hovmöller plots of eddy ellipse parameters M, N and ϕ_m are presented in figure 7.8, showing their evolution in time at a depth of 15m. From day 200, there is growth of a positive eddy momentum flux near the equator and negative eddy momentum flux north of the equator corresponding to the northern flank of the SECN. As the flow evolves, both regions of positive and negative eddy momentum fluxes strengthen. Patterns in M indicate that the eddies are zonally elongated at the equator and 4°, with meridional elongation between these regions. From day 250, positive contributions to N persist whilst the negative contributions weaken. At this time, there is a mean deceleration of the SECN due to eddy activity. This is also evident in the eddy tilts between 3°N-4°N which become positive and no longer tilt into the mean flow. By day 300, negative contributions to N north of the equator have vanished and eddy tilts are positive up to 7°N. There is a maximum in M which coincides with the location at which there is a local minimum in the maximum mean zonal velocity field. As the flow evolves beyond day 300, eddy momentum fluxes weaken and patterns are less distinguishable. Positive signals in M at the equator occur due to the alternating patters in the meridional velocity perturbation at the equator. The oscillating behaviour of ϕ_m beyond day 400 is similar to behaviours associated with barotropic ocean jets [Tamarin et al., 2016].

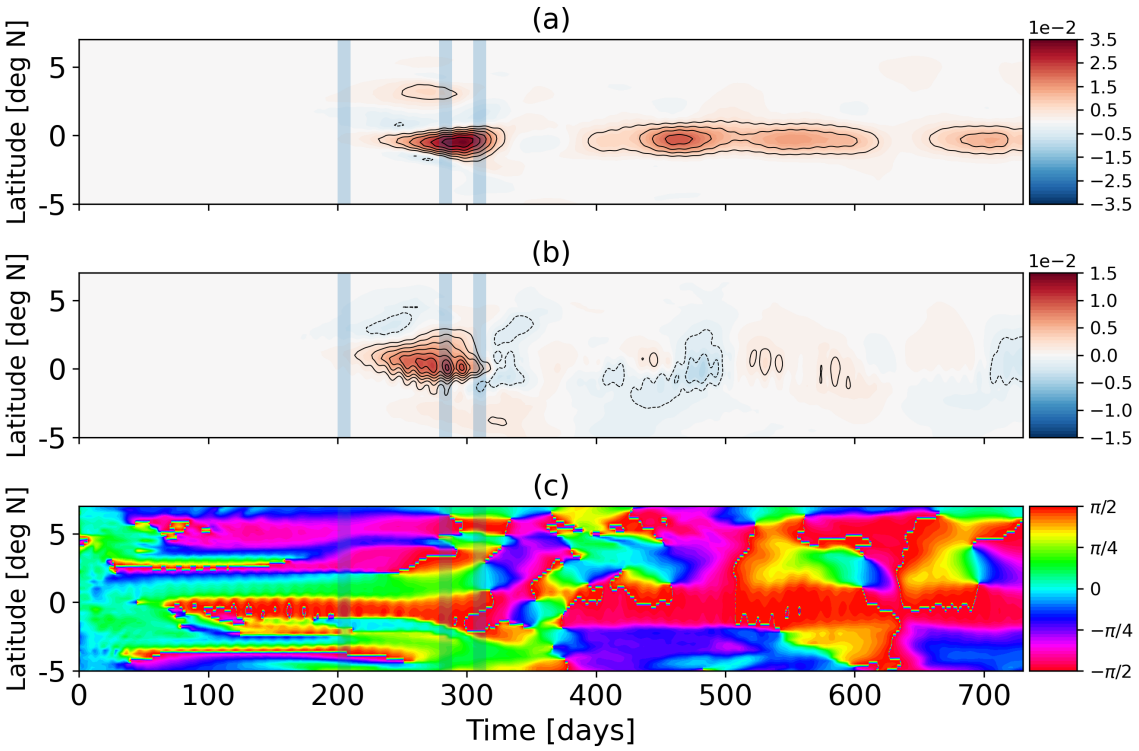


Figure 7.8: Hovmöller plots for the eddy ellipse quantities N $[m^2s^{-2}]$ (a), M $[m^2s^{-2}]$ (b) and ϕ_m (c) over the two year duration of integration M-NONLIN. Blue highlighted regions in time denote the linear, equilibrated and decaying stages of the TIW life-cycle, respectively.

7.4.2 Eddy Buoyancy Fluxes

As with the horizontal eddy Reynolds stresses, one can also look at the tilt of eddy ellipses in the vertical [Poulsen et al., 2019]. However, the definition of this tilt depends on the choice of the eddy stress tensor which is degenerate, as discussed in section 7.3. Instead, we follow a simpler approach here of looking at the pattern of the eddy form stress, S, associated with the vertical flux of zonal momentum, and show that it acts to reduce the mean vertical shear, hence extracting energy from the mean flow.

Linear Model

Depth-latitude plots of the zonal mean eddy form stress S for both models M-LIN and H-LIN is shown in figure 7.9. In both cases, there is an equatorward flux of heat by the eddies which is maximal on the southern flank of the SECN associated the strong mean meridional density gradients and vertical shear. Positive values of S together with a westward flowing mean current indicate that the eddies act to flux eastward momentum upwards to weaken the vertical shear. The eddy forcing on the mean flow, given by S_z, is positive beneath 25m and across the SECN, and is maximal at 2°N and 25m depth. There

are only minor differences in the structure of S between the models M-LIN and H-LIN, namely that S is slightly weaker for H-LIN when compared to M-LIN.

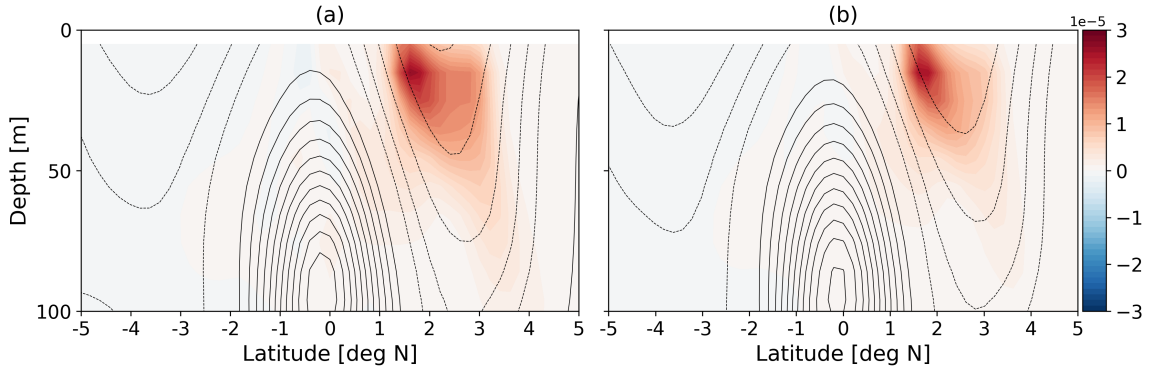


Figure 7.9: Depth-latitude plot of the zonally averaged eddy form stress $S = f_0\overline{v'b'}/N_0^2$ (colour) calculated from models M-LIN (a) and H-LIN (b). Superposed are contours of the mean zonal velocity field at intervals of 0.1ms^{-1} with positive (negative) values denoted by solid (dashed) contours.

Nonlinear Model

Depth-latitude plots of the zonal mean eddy meridional buoyancy flux for both integrations M-NONLIN and H-NONLIN. Similarly to the outputs of the linear models, the eddy meridional buoyancy flux is positive within the SECN which is indicative of an upwards vertical flux of eastward momentum acting to weaken the vertical shear of the SECN. The locations of the maxima in S for both integrations M-NONLIN and H-NONLIN are deeper than the linear model at a depth of 50m. The maximum also lies further eastward at 3°N which is at the core of the SECN and not on the southern flank.

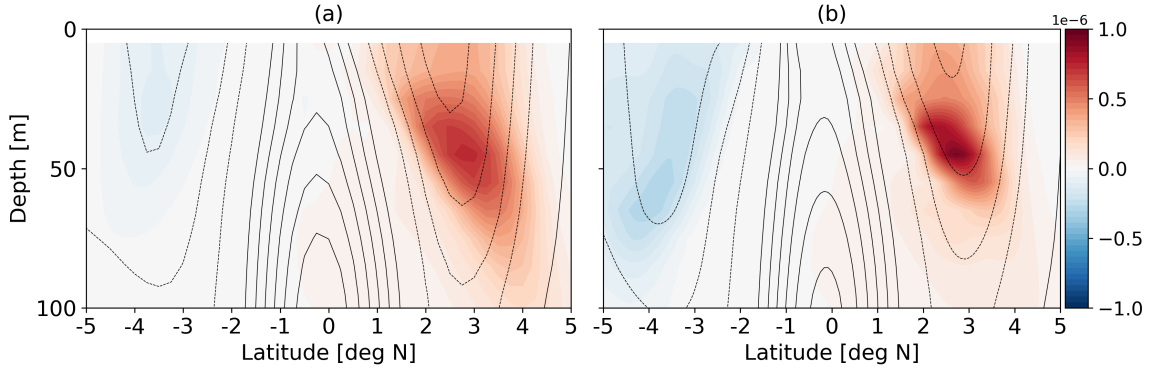


Figure 7.10: Depth-latitude plot of the zonally averaged eddy buoyancy flux $S = f_0\overline{v'b'}/N_0^2$ (colour) averaged in time over the linear period of the TIW life-cycle for integrations M-NONLIN (a) and H-NONLIN (b). Contours of the mean zonal velocity averaged over the same time period are superposed with contour intervals of 0.1ms^{-1}.

A Hovmöller plot of the eddy form stress S and mean zonal velocity is presented in figure 7.11 showing the time evolution of these fields over the two years of integration M-NONLIN. From day 200, there is a growth of positive S within the core of the SECN. The eddy form stress is maximal near day 260 and, up to day 300, one can see that the vertical flux of eastward momentum acts to decelerate the SECN and weaken the vertical shear. As the flow evolves beyond day 300, the eddy form stress weakens and patterns are less distinguishable.

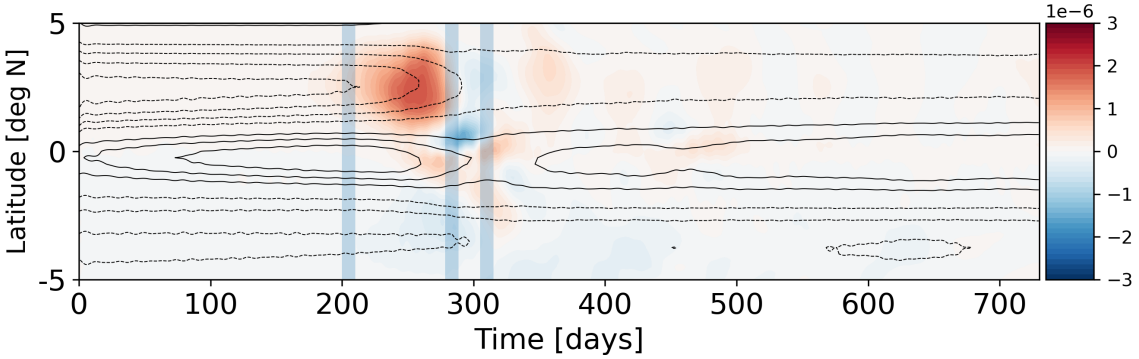


Figure 7.11: Hovmöller plot for the eddy form stress S (colour) and mean zonal velocity U (contours) depth averaged over the upper 50m of the domain for the two year duration of integration M-NONLIN. Blue highlighted regions in time denote the linear, equilibrated and decaying stages of the TIW life-cycle, respectively.

Chapter 8

Conclusions

The aim of this thesis has been to investigate the properties of tropical instability waves (TIWs) in idealised linear and fully nonlinear models of the equatorial Pacific ocean with mean fields computed from the outputs of both medium and high resolution eddy-resolving coupled AOGCM integrations, originally run by the Met Office. In particular, we have explored the three-dimensional structure of TIWs through various stages of the TIW life-cycle, namely the linear, equilibrated and decaying stages. We have also investigated eddy energetics to determine the instability mechanisms responsible for TIW growth. Additionally, we have elucidated the role of eddy feedbacks onto the mean flow by investigating the components of the eddy stress tensor and through visualisations of this tensor in terms of the spatial distribution of eddy ellipses. In this chapter we will summarise the findings of each chapter and outline extensions that could be made to this thesis.

8.1 Thesis Summary

In Chapter 3, we described the model configurations of the medium and high resolution AOGCM integrations. We presented outputs of the zonal velocity and temperature fields time-averaged over periods prior to TIW activity (July-August) and after TIW activity has ceased (March-April). This allowed us to investigate which features may be important for the instability of the equatorial Pacific ocean. In particular, the TIW-active period exhibits strong meridional shears north of the equator between the EUC and SECN, as well as between the SECN and NECC, which suggests that barotropic conversion in these regions could be important. Similarly, there is a strong meridional temperature gradient north of the equator associated with the equatorial cold tongue and the warm waters of the NECC, which suggests that baroclinic conversion in this region could be important.

In Chapter 4, we described the configuration and equations of motion for an idealised zonal channel centered on the equator. We perturbed about meridionally and vertically varying mean zonal velocity and mean density profiles, obtained by zonally averaging the fields described in chapter 3 over the longitude range over which TIWs are predominantly active ($110^\circ - 160^\circ$W), to obtain the linearised equations of motion. We then described the discretisation of the linearised equations of motion by a finite difference method and discuss the numerical procedure by which we solve the resulting large and sparse generalised eigenvalue problem. We assessed the reliability of our numerical solver by solving increasingly complex stability problems from the literature. We started by solving the classic one-dimensional stability problems of Rayleigh-Kuo [Kuo, 1949] and Eady/Stone [Eady, 1949, Stone, 1970] before proceeding to solve a series of idealised two-dimensional equatorial stability problems studied by Proehl [1996, 1998].

In Chapter 5, we solved the linearised equations of motion, described in chapter 4, for both the medium and high resolution mean fields, and calculated growth rates over a range of wavenumbers. The most unstable mode occurs at wavelengths significantly shorter than any TIWs in the literature. This may occur due to turbulent transports and vertical mixing implicit in our imposed mean fields, the representation of which is not included within our idealised linear model. However, there are unstable modes which have a local maximum within the wavelength range expected of TIWs, namely with a wavelength of $\sim$ 1000km and period of $\sim$ 30 days. The three-dimensional structure of the unstable mode exhibits features typical of TIWs, such as alternating patterns of meridional velocity at the equator. Additionally, the linear models exhibit asymmetric vortices about the equator centered at $\sim 2^\circ$N with alternating patterns of perturbation velocities, density and pressure. The spatial distribution of the eddies indicates an equatorward heat flux consistent with warming of the equatorial cold tongue, and eddy fluxes of eastward momentum into the westward flowing SECN. The dominant instability mechanism for TIW growth is baroclinic conversion ($\sim 90\%$ in the domain average) at the near surface between $1^\circ - 4^\circ$N. Eddy pressure work fluxes indicate that eddies act to redistribute energy from the generation site north of the equator to the south.

In Chapter 6, we described the configuration of the idealised fully nonlinear model for a zonally periodic channel centered on the equator. We initialise the model with the zonally invariant zonal velocity and temperature fields shown in chapter 5. We run the model for 2 years at both medium ($1/4^\circ$) and high ($1/12^\circ$) horizontal resolutions. The high resolution integration aborts the run prior to the equilibration of TIWs. We are able to identify

TIWs from signals of westward propagating vortices north of the equator, and alternating patterns of meridional velocity at the equator, with wavelengths of $\sim$ 930km and periods of $\sim$ 38 days. The use of a fully nonlinear model allows us to investigate the properties of TIWs beyond the early (linear) stages of TIW development. The three-dimensional structure of the TIWs during the linear stage of the TIW life-cycle agree with our outputs from the linear model with vortices north of the equator centered at 2°-3°N. The equilibrated TIWs have strong vortices on both sides of the equator. Analysis of the eddy energetics indicates that, during the linear stage of the TIW life-cycle, baroclinic conversion north of the equator, associated with the meridional temperature gradient between the equatorial cold tongue and NECC, is the dominant instability mechanism ($\sim$ 73% in the domain average). However, as the waves grow, barotropic conversion on the southern flank of the SECN is the dominant instability mechanism ($\sim$ 71% in the domain average) and is also the largest sink in eddy energy on the southern flank of the EUC. By investigating the mean fields both prior to, and after, TIW activity we find that the net effect of the eddies acts to warm the near surface equatorial waters, cool the northern subsurface waters by 1°C, and decelerate the SECN by a mean velocity of over 0.3ms^{-1}.

In Chapter 7, we investigated the role of eddy momentum fluxes and eddy buoyancy fluxes associated with TIWs and their feedbacks onto the mean flow. We discussed how one can encapsulate eddy forcing on the mean flow in terms of an eddy stress tensor. We derived the geometric decomposition of the eddy stress tensor which allows us to interpret eddy forcing via the spatial distribution of eddy ellipses. In particular, we show that spatial patterns of eddy momentum fluxes $N = \overline{u'v'}$ and corresponding "banana-shaped" eddies indicate an eastward momentum flux by the eddies into the westward flowing SECN, therefore acting to decelerate the mean flow in this region. Investigations of the eddy form stress also indicates a vertical transport of eastward momentum which acts to weaken the vertical shear associated with the SECN. The findings of this chapter agree for both the linear and nonlinear models, though the spatial structures of the eddy Reynolds stresses and eddy form stresses are broader in the nonlinear model. Eddy ellipse patterns are also consistent with classical stability theory and tilt into the shear of the mean flow to extract eddy energy and grow the perturbation. The GEOMETRIC framework provides a simple visual framework for which one can interpret eddy feedbacks onto the mean flow.

8.2 Future Work

In this section we outline possible avenues for future work that could extend the results of this thesis.

Surface Wind Forcing

Our linear and nonlinear models are idealised representations of the equatorial Pacific ocean. There are aspects of the physics which we have not included which are important for a more realistic simulation of TIWs in the equatorial Pacific ocean. We have not included the effects of external forcing such as surface wind stresses and surface heat fluxes. To extend our model, one could impose an idealised surface wind field which is a representation of the easterly equatorial trade winds. For example, one could impose an idealised zonal wind field which is strongest in the eastern Pacific and decays towards the western Pacific [McCreary Jr and Yu, 1992].

In our nonlinear model, NEMO calculates the surface boundary condition of the vertical turbulent momentum fluxes in terms of the surface horizontal wind stress vector $\boldsymbol{\tau}$. The vertical eddy viscosity and diffusivity coefficients ensure that surface wind stress is distributed in the vertical over the mixed layer depth. Our linear model does not include viscous effects and cannot model vertical mixing via turbulent momentum fluxes. However, to mitigate this issue, one could set a rigid lid to be at the base of the mixed layer (~ 30m) instead of the surface, and impose an Ekman pumping boundary condition on the vertical velocity in terms of the curl of the surface wind stress. This boundary condition can be viewed as the communication of a non-geostrophic external stress into the interior geostrophic motions of the ocean.

Chebyshev Collocation Method

In Chapter 4, we described the numerical method used to discretise the linearised equations of motion and solve the resulting generalised eigenvalue problem. We demonstrated the reliability of our numerical solver by solving well-documented linear stability problems in the existing literature. One could further improve upon the reliability of our numerical solver by the use of an additional numerical method which is independent of our existing finite difference discretisation scheme. One possible choice would be to use a spectral method such as the Chebyshev collocation method. We omit the details of this method, which are given in Trefethen [2000, Chapter 6], and proceed onto discussion of the advantages and disadvantages of using this numerical method. There are two main advantages for using a Chebyshev collocation method:

- Spectral methods have an exponential convergence rate of $O(e^{-cN})$, where c is a positive real number and N is the number of grid points. Conversely, a second-order finite difference method has an algebraic convergence rate of $O(N^{-2})$. Spectral

methods could allow one to obtain an accurate solution at a coarser grid resolution than with a finite difference method.

- The locations of grid points for the Chebyshev collocation method are clustered towards the edges of the domain. This would allow us to obtain a fine vertical grid resolution near the surface of the domain, where TIW signals are strongest, at a smaller number of grid points.

A disadvantage of using a Chebyshev collocation method is that the differentiation matrices, which are the discrete differentiation operators, are dense. One must use a dense eigenvalue solver, such as `scipy.linalg.eig` which employs the QZ algorithm [Moler and Stewart, 1973], which is significantly more computationally expensive than its sparse counterpart for large eigenvalue problems. However, if one only checks the eigenvalue corresponding to a single wavenumber, such as the most unstable mode, then comparison could be drawn to the corresponding eigenvalue and eigenvector pair obtained from the finite difference method.

We were able to solve the one-dimensional Rayleigh-Kuo and Eady problems discussed in chapter 4 using the Chebyshev collocation method (not shown). However, due to time constraints, we did not pursue the application of this method further. The success of the Chebyshev collocation method on a variety of both one and two-dimensional problems in the literature [Trefethen, 2000] indicates that one could successfully apply this method to our linear stability problem.

Investigations of TIWs directly from global coupled AOGCMs

We have performed investigations into TIWs in idealised models of the equatorial Pacific whose mean fields are motivated from realistic global eddy-resolving coupled AOGCM integrations. We have compared outputs between the linear and nonlinear models to gain insight into the effect of nonlinearity on the development of TIWs. One could perform similar analysis of TIWs directly from the outputs of the AOGCMs. This would allow one to investigate the development of TIWs in realistic models of the equatorial Pacific and to draw comparison to the idealised models and elucidate the effect of realistic physics on TIW dynamics.

Parametrisation of TIWs via GEOMETRIC

To improve the simulation of the equatorial Pacific in global climate models, one should improve the representation of TIWs to mitigate the equatorial cold tongue bias [Roberts

et al., 2009, Graham, 2014]. Therefore, there is interest in parametrisation of TIWs in eddy-permitting climate models [Imada and Kimoto, 2012]. The GEOMETRIC framework moves the need for parametrisation of eddy potential vorticity fluxes to parametrisation of the eddy Reynolds stresses and eddy form stresses, which are in turn related to the geometry of eddy ellipses. Given the eddy energy, the eddy anisotropies and eddy tilts could form the basis of a parametrisation for horizontal or vertical eddy momentum fluxes representative of TIW activity where energetic constraints are automatically satisfied through the use of the GEOMETRIC framework. One could also investigate analytical solutions for eddy tilts through the use of ray-tracing theory [Bühler, 2009] which has seen success for barotropic ocean jets [Tamarin et al., 2016].

Appendix A

Appendix

A.1 Eigenvalues of the Eddy Reynolds Stress Tensor

The eigenvalues of the eddy Reynolds stress tensor

$$\boldsymbol{E}_m = \begin{pmatrix} -M+K & N & 0 \\ N & M+K & 0 \\ 0 & 0 & -P \end{pmatrix}, \tag{A.1}$$

are solutions of the characteristic equation

$$\det\left(\boldsymbol{E}_m - \lambda \boldsymbol{I}\right) = 0, \tag{A.2}$$

where $\boldsymbol{I}$ is the 3×3 identity matrix. The characteristic equation is given by

$$\begin{vmatrix} -M+K-\lambda & N & 0 \\ N & M+K-\lambda & 0 \\ 0 & 0 & -P-\lambda \end{vmatrix} = 0, \tag{A.3}$$

$$(-P-\lambda)\left[(-M+K-\lambda)(M+K-\lambda) - N^2\right] = 0. \tag{A.4}$$

Inspection of (A.4) shows that one of the eigenvalues is $\lambda =_0 -P$. The two other eigenvalues are solution of the quadratic equation

$$\lambda^2 - 2K\lambda + K^2 - (M^2+N^2) = 0. \tag{A.5}$$

By the quadratic formula

$$\lambda_\pm = \frac{1}{2}\left[2K \pm \sqrt{4(M^2+N^2)}\right], \tag{A.6}$$

$$= K \pm K\sqrt{\frac{M^2+N^2}{K^2}}, \tag{A.7}$$

$$= K\left(1 \pm \gamma_m\right). \tag{A.8}$$

Therefore, the eigenvalues of the eddy Reynolds stress tensor are

$$\lambda_0 = -P \quad \text{and} \quad \lambda_\pm = K(1 \pm \gamma_m). \tag{A.9}$$

A.2 Eigenvalues of the Eddy Form Stress Tensor

The eigenvalues of the eddy form stress tensor

$$\boldsymbol{E}_b = \begin{pmatrix} K & 0 & -S/2 \\ 0 & K & R/2 \\ -S/2 & R/2 & P^* \end{pmatrix}, \tag{A.10}$$

are solutions of the characteristic equation

$$\det\left(\boldsymbol{E}_b - \xi \boldsymbol{I}\right) = 0, \tag{A.11}$$

where $\boldsymbol{I}$ is the 3×3 identity matrix and we use ξ to denote eigenvalues to avoid a conflict of notation with the eddy partition angle λ^*. The characteristic equation is given by

$$\begin{vmatrix} K-\xi & 0 & -S/2 \\ 0 & K-\xi & R/2 \\ -S/2 & R/2 & P^*-\xi \end{vmatrix} = 0, \tag{A.12}$$

$$(K-\xi)\left[(P^*-\xi)(K-\xi) - (R^2+S^2)/4\right] = 0. \tag{A.13}$$

Inspection of (A.13) shows that one of the eigenvalues is $\xi_0 = K$. The remaining eigenvalues are solutions of the quadratic equation

$$\xi^2 - (K+P^*)\xi + KP^* - (R^2+S^2)/4 = 0. \tag{A.14}$$

By the quadratic formula

$$\xi_\pm = \frac{1}{2}\left[(K+P^*) \pm \sqrt{(K+P^*)^2 - 4KP^* + (R^2+S^2)}\right]. \tag{A.15}$$

Let the total scaled eddy energy $L = K + P^*$ then

$$\xi_\pm = \frac{L}{2}\left[1 \pm \sqrt{1 + \frac{(R^2+S^2) - 4KP^*}{L^2}}\right] \tag{A.16}$$

The scaled eddy energy can be written in terms of the eddy potential energy, eddy kinetic energy, and an eddy energy partitioning angle λ^* as

$$\frac{P^*}{L} = \sin^2(\lambda *), \qquad \frac{K}{L} = \cos^2(\lambda^*). \tag{A.17}$$

One can substitute

$$\frac{1}{L^2} = \frac{\sin^2(\lambda^*)\cos^2(\lambda^*)}{KP^*}, \tag{A.18}$$

into (A.16) to obtain

$$\xi_\pm = \frac{L}{2}\left[1 \pm \sqrt{1 - 4\sin^2(\lambda^*)\cos^2(\lambda^*) + \frac{R^2+S^2}{KP^*}\sin^2(\lambda^*)\cos^2(\lambda^*)}\right]. \tag{A.19}$$

Using the trigonometric identities

$$\cos^2(2\lambda^*) = 1 - 4\sin^2(\lambda^*)\cos^2(\lambda^*), \qquad \frac{1}{4}\sin^2(2\lambda^*) = \sin^2(\lambda^*)\cos^2(\lambda^*), \tag{A.20}$$

we find

$$\xi_\pm = \frac{L}{2}\left[1 \pm \sqrt{\cos^2(2\lambda^*) + \frac{R^2+S^2}{4KP^*}\sin^2(2\lambda^*)}\right], \tag{A.21}$$

$$= \frac{L}{2}\left[1 \pm \sqrt{\cos^2(2\lambda^*) + \sin^2(2\lambda^*)\left(\frac{1}{2}\sqrt{\frac{R^2+S^2}{KP^*}}\right)^2}\right]. \tag{A.22}$$

Using

$$P^* = \frac{f_0^2}{N_0^2}P, \tag{A.23}$$

one can write

$$\xi_\pm = \frac{L}{2}\left[1 \pm \sqrt{\cos^2(2\lambda^*) + \sin^2(2\lambda^*)\left(\frac{N_0}{2|f_0|}\sqrt{\frac{R^2+S^2}{KP}}\right)}\right]. \tag{A.24}$$

Therefore,

$$\xi_\pm = \frac{L}{2}(1 \pm \gamma_t), \tag{A.25}$$

where

$$\gamma_t = \sqrt{\cos^2(2\lambda^*) + \sin^2(2\lambda^*)\gamma_b^2}, \tag{A.26}$$

and

$$\gamma_b = \frac{N_0}{2|f_0|}\sqrt{\frac{R^2+S^2}{KP}}. \tag{A.27}$$

Therefore, the eigenvalues of the eddy form stress tensor are

$$\xi_0 = K \quad \text{and} \quad \xi_\pm = \frac{L}{2}(1 \pm \gamma_t). \tag{A.28}$$

Bibliography

S.-I. An. Interannual variations of the tropical ocean instability wave and enso. *J. Clim.*, 21(15):3680–3686, 2008.

S.-I. An and F.-F. Jin. Nonlinearity and asymmetry of enso. *Journal of Climate*, 17(12): 2399–2412, 2004.

D. Andrews and M. E. Mcintyre. Planetary waves in horizontal and vertical shear: The generalized Eliassen-Palm relation and the mean zonal acceleration. *J. Atmos. Sci.*, 33 (11):2031–2048, 1976.

T. Andrews and M. J. Webb. The dependence of global cloud and lapse rate feedbacks on the spatial structure of tropical Pacific warming. *J. Clim.*, 31(2):641–654, 2018.

A. Arakawa. Computational design for long term integration of the equations of motion: Two-dimensional incompressible flow. part 1. *J. Comput. Phys*, 1(1):19–143, 1966.

M. Balmaseda, D. Dee, A. Vidard, and D. Anderson. A multivariate treatment of bias for sequential data assimilation: Application to the tropical oceans. *Quart. J. Roy. Met. Soc.*, 133(622):167–179, 2007.

N. Baturin and P. Niiler. Effects of instability waves in the mixed layer of the equatorial Pacific. *J. Geophys. Res. Oceans*, 102(C13):27771–27793, 1997.

M. J. Bell, M. Martin, and N. Nichols. Assimilation of data into an ocean model with systematic errors near the equator. *Quart. J. Roy. Met. Soc.*, 130(598):873–893, 2004.

J. Bjerknes. Atmospheric teleconnections from the equatorial pacific. *Monthly Weather Rev.*, 97(3):163–172, 1969.

J. Boucharel and F.-F. Jin. A simple theory for the modulation of tropical instability waves by enso and the annual cycle. *Tellus A: Dyn. Met. Ocean.*, 72(1):1–14, 2020.

H. L. Bryden and E. C. Brady. Eddy momentum and heat fluxes and their effects on the circulation of the equatorial Pacific Ocean. *J. Mar. Res.*, 47(1):55–79, 1989.

O. Bühler. *Waves and mean flows*. Cambridge University Press, 2009.

S. Butterworth et al. On the theory of filter amplifiers. *Wireless Engineer*, 7(6):536–541, 1930.

M. Cane and E. Sarachik. Forced baroclic ocean motions: I. The linear bounded equation case. *J. Mar. Res*, 34:629–665, 1976.

J. G. Charney and M. E. Stern. On the stability of internal baroclinic jets in a rotating atmosphere. *Journal of the Atmospheric Sciences*, 19(2):159–172, 1962.

D. B. Chelton, F. J. Wentz, C. L. Gentemann, R. A. de Szoeke, and M. G. Schlax. Satellite microwave sst observations of transequatorial tropical instability waves. *Geophys. Res. Lett.*, 27(9):1239–1242, 2000.

M. D. Cox. Generation and propagation of 30-day waves in a numerical model of the Pacific. *J. Phys. Oceanogr.*, 10(8):1168–1186, 1980.

H. T. de Decco, A. R. T. Junior, L. P. Pezzi, and L. Landau. Revisiting tropical instability wave variability in the atlantic ocean using soda reanalysis. *Ocean Dyn.*, 68 (3):327–345, 2018.

W. Duing, P. Hisard, E. Katz, J. Meincke, L. Miller, K. Moroshkin, G. Philander, A. Ribnikov, K. Voigt, and R. Weisberg. Meanders and long waves in the equatorial Atlantic. *Nature*, 257(5524):280–284, 1975.

E. T. Eady. Long waves and cyclone waves. *Tellus*, 1(3):33–52, 1949.

A. Eliassen. On the transfer of energy in stationary mountain waves. *Geofys. Publ.*, 22: 1–23, 1961.

H. Ertel. Ein neuer hydrodynamischer wirbelsatz met. *Z*, 59:271–281, 1942.

R. Feely, R. Wanninkhof, C. Cosca, M. McPhaden, R. Byrne, F. J. Millero, F. Chavez, T. Clayton, D. Campbell, and P. Murphy. The effect of tropical instability waves on CO2 species distributions along the equator in the eastern equatorial Pacific during the 1992 ENSO event. *Geophys. Res. Lett.*, 21(4):277–280, 1994.

P. J. Flament, S. C. Kennan, R. A. Knox, P. P. Niiler, and R. L. Bernstein. The three-dimensional structure of an upper ocean vortex in the tropical Pacific Ocean. *Nature*, 383(6601):610–613, 1996.

S. A. Good, M. J. Martin, and N. A. Rayner. En4: Quality controlled ocean temperature and salinity profiles and monthly objective analyses with uncertainty estimates. *Journal of Geophysical Research: Oceans*, 118(12):6704–6716, 2013.

T. Graham. The importance of eddy permitting model resolution for simulation of the heat budget of tropical instability waves. *Ocean. Mod.*, 79:21–32, 2014.

S. M. Griffies, M. Winton, W. G. Anderson, R. Benson, T. L. Delworth, C. O. Dufour, J. P. Dunne, P. Goddard, A. K. Morrison, A. Rosati, et al. Impacts on ocean heat from transient mesoscale eddies in a hierarchy of climate models. *J. Clim.*, 28(3):952–977, 2015.

S. A. Grodsky, J. A. Carton, C. Provost, J. Servain, J. A. Lorenzzetti, and M. J. McPhaden. Tropical instability waves at 0 N, 23 W in the Atlantic: A case study using Pilot Research Moored Array in the Tropical Atlantic (PIRATA) mooring data. *J. Geophys. Res. Oceans*, 110(C8), 2005.

D. V. Hansen and C. A. Paul. Genesis and effects of long waves in the equatorial Pacific. *J. Geophys. Res. Oceans*, 89(C6):10431–10440, 1984.

B. J. Hoskins, I. N. James, and G. H. White. The shape, propagation and mean-flow interaction of large-scale weather systems. *J. Atmos. Sci.*, 40(7):1595–1612, 1983.

B. J. Hoskins, M. E. McIntyre, and A. W. Robertson. On the use and significance of isentropic potential vorticity maps. *Quarterly Journal of the Royal Meteorological Society*, 111(470):877–946, 1985.

Y. Imada and M. Kimoto. Parameterization of tropical instability waves and examination of their impact on ENSO characteristics. *J. Clim.*, 25(13):4568–4581, 2012.

Y. Imada, M. Kimoto, and X. Chen. Impact of the atmospheric mean state on tropical instability wave activity. *J. Clim.*, 25(7):2341–2355, 2012.

S. IOC and IAPSO. The international thermodynamic equation of seawater: Calculation and use of thermodynamic properties. *Intergovernmental Oceangraphic Commision, Manuals and Guides*, 56:196, 2010.

M. Jochum and R. Murtugudde. Temperature advection by tropical instability waves. *J. Phys. Oceanogr.*, 36(4):592–605, 2006.

M. Jochum, P. Malanotte-Rizzoli, and A. Busalacchi. Tropical instability waves in the atlantic ocean. *Ocean Mod.*, 7(1-2):145–163, 2004.

G. C. Johnson and H. L. Bryden. On the size of the antarctic circumpolar current. *Deep Sea Research Part A. Oceanographic Research Papers*, 36(1):39–53, 1989.

S. C. Kennan and P. J. Flament. Observations of a tropical instability vortex. *J. Phys. Oceanogr.*, 30(9):2277–2301, 2000.

G. Kontogiannis and N. A. Bakas. A geometric interpretation of zonostrophic instability. *J. Phys. Oceanogr.*, 2020.

H.-l. Kuo. Dynamic instability of two-dimensional nondivergent flow in a barotropic atmosphere. *J. Meteor.*, 6(2):105–122, 1949.

H.-L. Kuo. Dynamics of quasigeostrophic flows and instability theory. *Advances in Applied Mechanics*, 13:247–330, 1973.

R. Legeckis. Long waves in the eastern equatorial Pacific Ocean: A view from a geostationary satellite. *Science*, 197(4309):1179–1181, 1977.

R. B. Lehoucq, D. C. Sorensen, and C. Yang. *ARPACK users' guide: solution of large-scale eigenvalue problems with implicitly restarted Arnoldi methods*. SIAM, 1998.

G. Li and S.-P. Xie. Origins of tropical-wide sst biases in cmip multi-model ensembles. *Geophys. Res. Lett.*, 39(22), 2012.

G. Li and S.-P. Xie. Tropical biases in cmip5 multimodel ensemble: The excessive equatorial pacific cold tongue and double itcz problems. *J. Clim.*, 27(4):1765–1780, 2014.

R.-C. Lien, E. A. d'Asaro, and C. E. Menkes. Modulation of equatorial turbulence by tropical instability waves. *Geophys. Res. Lett.*, 35(24), 2008.

J.-L. Lin. The double-itcz problem in ipcc ar4 coupled gcms: Ocean–atmosphere feedback analysis. *J. Clim.*, 20(18):4497–4525, 2007.

Z. Lin, J. Yang, and H. Zhu. Barotropic instability of shear flows. *Studies in Applied Mathematics*, 144(3):289–326, 2020.

R. S. Lindzen. Instability of plane parallel shear flow (toward a mechanistic picture of how it works). *Pure and App. Geophys.*, 126(1):103–121, 1988.

R. Locarnini, A. Mishonov, J. Antonov, T. Boyer, H. Garcia, O. Baranova, M. Zweng, C. Paver, J. Reagan, D. Johnson, et al. World ocean atlas 2013, volume 1: Temperature, edited by: Levitus, s. *A. Mishonov Technical Ed., NOAA Atlas NESDIS*, 73:40, 2013.

R. Lukas. Horizontal Reynolds stresses in the central equatorial Pacific. *J. Geophys. Res. Oceans*, 92(C9):9453–9463, 1987.

D. S. Luther and E. S. Johnson. Eddy energetics in the upper equatorial Pacific during the Hawaii-to-Tahiti Shuttle Experiment. *J. Phys. Oceanogr.*, 20(7):913–944, 1990.

J. M. Lyman, D. B. Chelton, R. A. DeSzoeke, and R. M. Samelson. Tropical instability waves as a resonance between equatorial Rossby waves. *J. Phys. Oceanogr.*, 35(2): 232–254, 2005.

J. M. Lyman, G. C. Johnson, and W. S. Kessler. Distinct 17-and 33-day tropical instability waves in subsurface observations. *J. Phys. Oceanogr.*, 37(4):855–872, 2007.

J. R. Maddison and D. P. Marshall. The eliassen–palm flux tensor. *Journal of Fluid Mechanics*, 729:69–102, 2013.

G. Madec. *NEMO ocean engine*, 2016.

J. Mak, D. P. Marshall, J. R. Maddison, and S. D. Bachman. Emergent eddy saturation from an energy constrained eddy parameterisation. *Ocean Modelling*, 112:125–138, 2017.

J. Mak, J. R. Maddison, D. P. Marshall, and D. R. Munday. Implementation of a geometrically informed and energetically constrained mesoscale eddy parameterization in an ocean circulation model. *Journal of Physical Oceanography*, 48(10):2363–2382, 2018.

D. P. Marshall, J. R. Maddison, and P. S. Berloff. A framework for parameterizing eddy potential vorticity fluxes. *J. Phys. Oceanogr.*, 42(4):539–557, 2012.

M. Martin, M. Bell, and N. K. Nichols. Estimation of systematic error in an equatorial ocean model using data assimilation. *Inter. J. Num. Meth. Flu.*, 40(3-4):435–444, 2002.

S. Masina. Tropical instability waves in the Pacific Ocean. 1997.

S. Masina, S. Philander, and A. Bush. An analysis of tropical instability waves in a numerical model of the Pacific Ocean: 2. Generation and energetics of the waves. *J. Geophys. Res. Oceans*, 104(C12):29637–29661, 1999.

T. Matsuno. Quasi-geostrophic motions in the equatorial area. *J. Meteor. Soc. Japan*, 44 (1):25–43, 1966.

J. P. McCreary Jr and Z. Yu. Equatorial dynamics in a 2.5-layer model. *Prog. Oceanogr.*, 29(1):61–132, 1992.

M. McPhaden and P. Ripa. Wave-mean flow interactions in the equatorial ocean. *Annual. Rev. Fluid Mech.*, 22(1):167–206, 1990.

C. R. Mechoso, A. W. Robertson, N. Barth, M. Davey, P. Delecluse, P. Gent, S. Ineson, B. Kirtman, M. Latif, H. L. Treut, et al. The seasonal cycle over the tropical pacific in coupled ocean–atmosphere general circulation models. *Monthly Weather Rev.*, 123(9): 2825–2838, 1995.

C. B. Moler and G. W. Stewart. An algorithm for generalized matrix eigenvalue problems. *SIAM Journal on Numerical Analysis*, 10(2):241–256, 1973.

J. Moum, R.-C. Lien, A. Perlin, J. Nash, M. Gregg, and P. Wiles. Sea surface cooling at the equator by subsurface mixing in tropical instability waves. *Nat. Geosci.*, 2(11): 761–765, 2009.

J. N. Moum, A. Perlin, J. D. Nash, and M. J. McPhaden. Seasonal sea surface cooling in the equatorial pacific cold tongue controlled by ocean mixing. *Nature*, 500(7460):64–67, 2013.

W. H. Munk and E. Palmen. Note on the dynamics of the antarctic circumpolar current 1. *Tellus*, 3(1):53–55, 1951.

S. Musman. Geosat altimeter observations of long waves in the equatorial atlantic. *J. Geophys. Res: Oceans*, 97(C3):3573–3579, 1992.

A. Navarra, S. Gualdi, S. Masina, S. Behera, J.-J. Luo, S. Masson, E. Guilyardi, P. Delécluse, and T. Yamagata. Atmospheric horizontal resolution affects tropical climate variability in coupled models. *J. Clim.*, 21(4):730–750, 2008.

J. Pedlosky. The stability of currents in the atmosphere and the ocean: Part i. *Journal of Atmospheric Sciences*, 21(2):201–219, 1964.

S. Philander. Instabilities of zonal equatorial currents. *J. Geophys. Res.*, 81(21): 3725–3735, 1976.

S. Philander. Instabilities of zonal equatorial currents, 2. *J. Geophys. Res. Oceans*, 83 (C7):3679–3682, 1978.

S. Philander. Equatorial waves in the presence of the equatorial undercurrent. *J. Phys. Oceanogr.*, 9(2):254–262, 1979.

S. Philander, W. Hurlin, and R. Pacanowski. Properties of long equatorial waves in models of the sea-sonal cycle in the tropic Atlantic and Pacific oceans. *J. Geophys. Res.*, 91:14–207, 1986.

S. Philander, W. Hurlin, and A. Seigel. Simulation of the seasonal cycle of the tropical Pacific Ocean. *J. Phys. Oceanogr.*, 17(11):1986–2002, 1987.

R. A. Plumb. Three-dimensional propagation of transient quasi-geostrophic eddies and its relationship with the eddy forcing of the time—mean flow. *J. Atmos. Sci.*, 43(16): 1657–1678, 1986.

M. B. Poulsen, M. Jochum, J. R. Maddison, D. P. Marshall, and R. Nuterman. A geometric interpretation of southern ocean eddy form stress. *Journal of Physical Oceanography*, 49(10):2553–2570, 2019.

R. W. Preisendorfer and C. D. Mobley. Principal component analysis in meteorology and oceanography. *Developments in atmospheric science*, 17, 1988.

J. A. Proehl. Linear stability of equatorial zonal flows. *J. Phys. Oceanogr.*, 26(4):601–621, 1996.

J. A. Proehl. The role of meridional flow asymmetry in the dynamics of tropical instability. *J. Geophys. Res: Oceans*, 103(C11):24597–24618, 1998.

L. Qiao and R. H. Weisberg. Tropical instability wave kinematics: Observations from the tropical instability wave experiment. *J. Geophys. Res. Oceans*, 100(C5):8677–8693, 1995.

L. Qiao and R. H. Weisberg. Tropical instability wave energetics: Observations from the tropical instability wave experiment. *J. Phys. Oceanogr.*, 28(2):345–360, 1998.

S. Ray, A. T. Wittenberg, S. M. Griffies, and F. Zeng. Understanding the equatorial pacific cold tongue time-mean heat budget. part ii: Evaluation of the gfdl-flor coupled gcm. *J. Clim.*, 31(24):9987–10011, 2018.

M. J. Roberts, H. Banks, N. Gedney, J. Gregory, R. Hill, S. Mullerworth, A. Pardaens, G. Rickard, R. Thorpe, and R. Wood. Impact of an eddy-permitting ocean resolution on control and climate change simulations with a global coupled gcm. *J. Clim.*, 17(1): 3–20, 2004.

M. J. Roberts, A. Clayton, M.-E. Demory, J. Donners, P. L. Vidale, W. Norton, L. Shaffrey, D. Stevens, I. Stevens, R. Wood, et al. Impact of resolution on the tropical pacific circulation in a matrix of coupled models. *J. Clim.*, 22(10):2541–2556, 2009.

M. J. Roberts, P. L. Vidale, M. S. Mizielinski, M.-E. Demory, R. Schiemann, J. Strachan, K. Hodges, R. Bell, and J. Camp. Tropical cyclones in the upscale ensemble of high-resolution global climate models. *Journal of Climate*, 28(2):574–596, 2015.

T. T. Sakamoto, Y. Komuro, T. Nishimura, M. Ishii, H. Tatebe, H. Shiogama, A. Hasegawa, T. Toyoda, M. Mori, T. Suzuki, et al. Miroc4h—a new high-resolution atmosphere-ocean coupled general circulation model. *J. Met. Soc. Japan. Ser. II*, 90(3): 325–359, 2012.

K. Stewart, P. Spence, S. Waterman, J. Le Sommer, J.-M. Molines, J. Lilly, and M. H. England. Anisotropy of eddy variability in the global ocean. *Ocean Modelling*, 95:53–65, 2015.

P. H. Stone. On non-geostrophic baroclinic stability. *J. Atmos. Sci.*, 23(4):390–400, 1966.

P. H. Stone. On non-geostrophic baroclinic stability: Part ii. *J. Atmos. Sci.*, 27(5): 721–726, 1970.

P. G. Strutton, J. P. Ryan, and F. P. Chavez. Enhanced chlorophyll associated with tropical instability waves in the equatorial Pacific. *Geophys. Res. Lett.*, 28(10): 2005–2008, 2001.

M. S. Swenson and D. V. Hansen. Tropical Pacific Ocean mixed layer heat budget: The Pacific cold tongue. *J. Phys. Oceanogr.*, 29(1):69–81, 1999.

T. Tamarin, J. R. Maddison, E. Heifetz, and D. P. Marshall. A geometric interpretation of eddy Reynolds stresses in barotropic ocean jets. *J. Phys. Oceanogr.*, 46(8):2285–2307, 2016.

Y. Tanaka and T. Hibiya. Generation mechanism of tropical instability waves in the equatorial Pacific Ocean. *J. Phys. Oceanogr.*, 49(11):2901–2915, 2019.

L. N. Trefethen. *Spectral methods in MATLAB*. SIAM, 2000.

UNESCO. Algorithms for the computation of fundamental properties of seawater. *Technical Papers in Marine Science*, 44:58, 1983.

B. Vanniere, E. Guilyardi, G. Madec, F. J. Doblas-Reyes, and S. Woolnough. Using seasonal hindcasts to understand the origin of the equatorial cold tongue bias in cgcms and its impact on enso. *Clim. dyn.*, 40(3-4):963–981, 2013.

K. Von Schuckmann, P. Brandt, and C. Eden. Generation of tropical instability waves in the atlantic ocean. *J. Geophys. Res. Oceans*, 113(C8), 2008.

R. Wardle and J. Marshall. Representation of eddies in primitive equation models by a PV flux. *J. Phys. Oceanogr.*, 30(10):2481–2503, 2000.

S. Waterman and B. J. Hoskins. Eddy shape, orientation, propagation, and mean flow feedback in western boundary current jets. *J. Phys. Oceanogr.*, 43(8):1666–1690, 2013.

S. Waterman and J. M. Lilly. Geometric decomposition of eddy feedbacks in barotropic systems. *J. Phys. Oceanogr.*, 45(4):1009–1024, 2015.

D. J. Webb. On the role of the north equatorial counter current during a strong el niño. *Ocean Sci.*, 14(4):633–660, 2018.

R. H. Weisberg and T. J. Weingartner. Instability waves in the equatorial Atlantic Ocean. *J. Phys. Oceanogr.*, 18(11):1641–1657, 1988.

C. S. Willett, R. R. Leben, and M. F. Lavín. Eddies and tropical instability waves in the eastern tropical Pacific: A review. *Prog. Oceanogr.*, 69(2-4):218–238, 2006.

K. Williams, C. Harris, A. Bodas-Salcedo, J. Camp, R. Comer, D. Copsey, D. Fereday, T. Graham, R. Hill, T. Hinton, et al. The met office global coupled model 2.0 (gc2) configuration. *Geosci. Model Dev.*, 8(5):1509–1524, 2015.

D. Wilson and A. Leetmaa. Acoustic Doppler current profiling in the equatorial Pacific in 1984. *J. Geophys. Res. Oceans*, 93(C11):13947–13966, 1988.

K. Wyrtki. El Niño - the dynamic response of the equatorial pacific oceanto atmospheric forcing. *J. Phys. Oceanogr.*, 5(4):572–584, 1975.

K. Wyrtki and B. Kilonsky. Mean water and current structure during the Hawaii-to-Tahiti shuttle experiment. *J. Phys. Oceanogr.*, 14(2):242–254, 1984.

X. Yin, J. Boutin, G. Reverdin, T. Lee, S. Arnault, and N. Martin. Smos Sea Surface Salinity signals of tropical instability waves. *J. Geophys. Res. Oceans.*, 119(11): 7811–7826, 2014.

W. R. Young. An exact thickness-weighted average formulation of the boussinesq equations. *Journal of Physical Oceanography*, 42(5):692–707, 2012.

Z. Yu, J. P. McCreary Jr, and J. A. Proehl. Meridional asymmetry and energetics of tropical instability waves. *J. Phys. Oceanogr.*, 25(12):2997–3007, 1995.

C. Zhou and J. Boyd. Nonlinear shallow water tropical instability waves on the equatorial β-plane: Genesis of two distinct types of waves. *Geophys. Res. Lett.*, 36(23), 2009.